(5) 2 9 9 f $\int_{\ell} \ell$

(1)

NOT SUITABLE FOR RELEASE TO OTS

RESEARCH ON MATERIALS, PROCESSES,

AND DEVICES RELATED TO

ENERGY CONVERSION

Semiannual Technical Summary Report

Scientific Report No. 6

MASSACHUSETTS INSTITUTE OF TECHNOLOGY

ENERGY CONVERSION RESEARCH

SCHOOL OF ENGINEERING

December 31, 1962

DDC

JUN 20 1963

TISIA D

AD No. 402856

CBC FILE COPY

407 856

④ Λ/Λ

⑤ — 299 800

⑥ RESEARCH ON MATERIALS, PROCESSES, AND DEVICES
RELATED TO ENERGY CONVERSION

⑦-⑧ Λ/Λ

⑨ Semiannual Technical Summary Report.

⑭ Scientific Report No. 6

⑩ Λ/Λ

⑫ 651.

⑬ Λ/Λ

⑱ Λ/Λ

⑲ Λ/Λ

⑳ Λ

㉑ Λ/Λ

MASSACHUSETTS INSTITUTE OF TECHNOLOGY
ENERGY CONVERSION RESEARCH
SCHOOL OF ENGINEERING

⑮ Contract No. Nonr-1841(78)
⑯ Authorization ARPA Order No. 214-62
⑰ Task No. NR 099-360
Project Code Number 9800
M.I.T. Project DSR 8848-8849

⑪ December 31, 1962

TABLE OF CONTENTS

TABLE OF CONTENTS (Continued)

INTRODUCTION

The primary goal of the Energy Conversion Research program as instigated in June 1961 was the investigation of all fundamental processes of energy conversion. The program was based on the thesis that research must precede device development by a significant period of time if maximum overall results are to be obtained without excessive waste of time, effort and development funds.

A second goal of equal significance to the above was the conducting of this research in a university environment so that the research was used to train future scientists and engineers. The research reported herein has been carried out under such a system.

The total number of students supported by the program during this reporting period has been 69 and during this same period there have been 10 masters degrees, 1 engineer's degree, and 7 doctorates granted to students associated with the program. This is a significant accomplishment for a program that has been in operation less than two years and which in its second year was reduced and organized to phase out at the end of the second year. The output of doctorates would have reached an even larger number by the end of 1964 had the funding continued as originally anticipated.

The student and faculty participation has been centered in five departments of the Engineering School. These include the Mechanical Engineering Department, Electrical Engineering Department, Metallurgy Department, Nuclear Engineering Department, and Chemical Engineering Department. Students have received doctorates during this period from four of these departments and doctorates and master's degrees from all departments involved. The students receiving degrees under the program are:

Metallurgy

K.M. Ralls	S.M.	September 1962
C.S. Tedmon, Jr.	S.M.	September 1962
R.E. Enstrom	S.M.	January 1962
C. Stein	Sc.D.	June 1962
R. Cairns	Sc.D.	June 1962
W. Ferguson	M.E.	June 1962
J. Benjamin	S.M.	September 1962

Mechanical Engineering

J.R. Bledsoe	M.S.	January 1962
P. Klimowski	Sc.D.	September 1962
W.T. Norris	Sc.D.	September 1962
J. Psarouthokis	M.S.	September 1962

Chemical Engineering

A.R. Reti	Sc.D.	June 1962
R. Slott	Sc.D.	January 1962

Electrical Engineering

B.D. Wedlock	Sc.D.	September 1962
G.S. Almasi	S.M.	September 1962
S.I. Butman	S.M.	September 1962
F.A. Leith	S.M.	September 1962
L. Mandel	S.M.	September 1962

The research reported herein is divided into five major divisions:
I. Superconducting Materials and Systems, II. Electrochemical Energy
Conversion Research, III. High Temperature Metallurgy Research on
Thermoelectric and Thermionic Materials, IV. Solid State Energy Converters,
V. The Development of Thermionic Emitter Materials. In addition to specific
status reports under each major heading several specific finished pieces of
research being submitted for publication are also included. In addition to these
data other reports and papers that have been published under the contract since
the last reporting period are:

"Spectral Response and Conversion Efficiency of P-N Junctions", B.D. Wedlock,
Contract Nonr 1841(78) Scientific Report No. 3, August 20, 1962.

"Rate Limiting Steps on Fuel Cells Electro", A.R. Reti, Contract Nonr 1841(78)
Scientific Report No. 4, June 1962.

"Electrochemical Oxidation of Formic Acid", R. Slott, Contract Nonr 1841(78) Scientific Report No. 5, January 1963.

"Thermionic Emission From a Single Crystal of Tantalum Exposed to Cesium Vapor", W.T. Norris, Sc.D. Thesis, Mechanical Engineering Department, M.I.T., September 1962.

"The Design Construction and Testing of a Cesium Thermionic Converter with Monocrystal Molybdenum Emitter", J. Psarouthakis, S.M. Thesis, Mechanical Engineering Department, M.I.T., June 1962.

"Thermodynamics of Surface Films", E.N. Carabateas, Journal of Applied Physics, September 1962.

"A Ductile, High-Field, High-Current Ternary Superconducting Alloy", R.M. Rose and J. Wulff, J. Appl. Phys., 33, 2394 (1962).

"High-Field Capabilities of High-Zirconium Nb-Zr Superconducting Alloys", K.M. Ralls, A. L. Donlevy, R.M. Rose, and J. Wulff, to be published in Proceedings of the Conference on Advanced Electronic Materials (A.I.M.E.), paper presented, August 1962.

"Superconductivity in Single and Polycrystalline Niobium", C.S. Tedmon, Jr. R.M. Rose, and J. Wulff, to be published in Proceedings of the Conference on Advanced Electronic Materials (A.I.M.E.), paper presented, August 1962.

"Current and Field Dependence of Superconductivity in the Nb-Sn System" R.E. Enstrom, T.H. Courtney, G.W. Pearsall, and J. Wulff, to be published in Proceedings of the Conference on Advanced Electronic Materials (A.I.M.E.), paper presented, August 1962.

"Joining Current Contacts to Superconducting Wire", K.M. Ralls, A.L. Donlevy, R.M. Rose, and J. Wulff, to be published in the Welding Journal, and to be presented at the Fall Meeting 1963 of the American Welding Society.

"The Niobium-Thorium Eutectic as a High-Field, High-Current Superconducting Alloy," H.E. Cline, R.M. Rose, and J. Wulff submitted to Journal of Applied Physics.

I SUPERCONDUCTING MATERIALS AND SYSTEMS

1.0   Superconducting Solid Solutions

Personnel:

    J. Wulff, Professor of Metallurgy
    R.M. Rose, Assistant Professor of Metallurgy
    A.L. Donlevy, Research Assistant, Metallurgy
    H.E. Cline, Research Assistant, Metallurgy
    K.M. Ralls, N.S.F. Graduate Fellow in Engineering (Metallurgy)

Research Report:

1.1   Solid Solution Alloys

The study of the influence of processing variables on the critical current level of Nb-Zr alloys is continuing. It has been demonstrated, for instance, that drawing at intermediate diameters, rather than swaging (as is generally the practice) is preferable in combination with certain heat treatments, when processing 25% Zr wire. In this connection, the heat treatments of Kneip,[1] and Wong[2] are being investigated systematically, especially with regard to the phase of processing during which the heat treatment is carried out. Although the situation is not simple, we hope to have resolved a number of questions in the near future.

1.2   Synthetic Microstructures

By metallurgical techniques, a synthetically hard filamentary network of niobium has been fabricated, in a thorium matrix. The resulting material is ductile, and carries in excess of 10^4 amperes per square centimeter, independent of magnetic field, at fields up to the highest we have used to date, 82.5 kilogauss. This critical current level promises, consequently, to persist up to considerably higher fields. The details of the investigation are disclosed in the accompanying preprint, which is a copy of the manuscript we have submitted to the Journal of Applied Physics, entitled, "The Niobium-

---

[1] Superscripts refer to numbers items in the References on pages

Thorium Eutectic Alloy as a High-Field, High-Current Superconductor," by
H.E. Cline, R.M. Rose, and J. Wulff. Work is continuing on this material,
in order to obtain better consistency in critical current level, and to improve
the over-all level of critical current density. Besides the obvious significance
for the device builder, this material offers the opportunity of checking the
paramagnetically limited critical field which has been proposed by
Chandrasekhar[3] and Clogston[4].

1.3 Current Contact Research

A number of the more popular current contacts have been sur-
veyed. Although it is generally conceded that, if contact resistance is much
in excess of 10 microhms, the shape and height of the critical current den-
sity vs. field are altered drastically, the physical reasons for this bevahior
are not clear. The most obvious cause, i.e., Joule heating due to the
passage of current directly through an insulating film, has been used, as the
basis of an approximate calculation, by Aron and Hitchcock[5]. However, the
idea of heat rise due to film resistance can be discredited from two view-
points[6]: the calculations do not yield temperature rises of the order of
magnitude necessary to explain the results, and the possible surface films
would all yield very high contact resistances, if unbroken. A more accurate
picture of the interface between two materials may be found in the very
extensive work of Holm[7]. Holm has found that oxide or other types of films
are indeed present at contacts and interfaces, but that almost all of the
current transferred through the contact flows through holes and defects in
the insulating film. Although there is at best a vanishingly small resistance
associated with a film-free interface, the concentration of the current in
order to flow through the holes gives rise to the voltage which is commonly
associated with "contact resistance." By using the combined flow of heat
and current, several investigators[7,8] have obtained differential equations
for the temperature distribution. In a paper which we have just submitted
to the American Welding Society, for presentation at the 1963 Fall Meeting,
and for publication in The Welding Journal, we have obtained an approximate
solution to this equation. The manuscript, entitled "Joining Current Contacts
To Superconducting Wire," by K.M. Ralls, A.L. Donlevy, R.M. Rose, and

J. Wulff, presents the survey of contact resistances and the calculations
mentioned above. We hope to have preprints available at the time of this
report; if this proves to be impossible, we shall include the preprints with
the final report. On a practical basis, we have demonstrated that current
contacts may be made to 0. 010" diameter Nb-Zr wire which are compact,
have resistances of less than $\frac{1}{2}$ microhm (and sometimes considerably lower),
and have saturation of magneto-resistance at relatively low values, allowing
the use of high fields. Contacts of this type allow full utilization of the
superconducting properties of the alloy wire, right up to the critical field of
the wire itself.

1.4   References

1. Kneip, G. D. Jr., et. al., High Magnetic Fields, M.I.T., Wiley, 1962,
   Kolm, H.H., et. al., editors, p. 603.

2. Wong, J., presented at Special Session on Superconducting Materials
   for Magnets, 1962 Annual Meeting AIME, New York, February 18, 1962.

3. Chandrasekhar, B.S., Applied Physics Letters 1, 7 (1962).

4. Clogston, A.M., Phys. Rev. Letters, September 15, 1962, p. 266.

5. Aron, P.R., and Hitchcock, H.C., J. App. Phys. 33, 2242 (1962).

6. Publication no. 2, this report.

7. Holm, R., Electric Contacts Handbook, Springer-Verlag 1958, p. 2 ff.

8. Diesselhorst, H., Ann. Phys. Lpz. 1 (1900), 312.

1.5   Publications

1. "The Niobium-Thorium Eutectic Alloy as a High-Field, High-Current
   Superconductor," by H. E. Cline, R.M. Rose, and J. Wulff; manuscript
   submitted to the Journal of Applied Physics; a preprint of the manuscript
   accompanies this report.

2. "Joining Current Contacts to Superconducting Wire," by K.M. Ralls, A. L.
   Donlevy, R.M. Rose, and J. Wulff; manuscript submitted to The Welding
   Journal, and for presentation at the 1963 Fall Meeting of the American
   Welding Society.

1.6   Appendix I-A

THE NIOBIUM-THORIUM EUTECTIC ALLOY AS A HIGH-FIELD, HIGH-CURRENT SUPERCONDUCTOR

THE NIOBIUM-THORIUM EUTECTIC ALLOY AS A HIGH-FIELD, HIGH-CURRENT SUPERCONDUCTOR

by

H. E. Cline,* R. M. Rose,** and J. Wulff***

ABSTRACT

Niobium-thorium eutectic alloys having fine acicular microstructures were produced by fast cooling from a vacuum melt. Although the solidified material was normal, continuity between the superconducting niobium-rich phase, which was essentially pure niobium, was attained by plastic deformation at room temperature. The resulting wire was tested for critical current at $4.2°K$, in transverse magnetic fields up to 82.5 kilogauss; at the highest field, critical current densities of slightly more than 10^4 amps per square centimeter were observed. The critical current density was independent of applied field from 20 kilogauss to the highest field used; the level of critical current density depended on diameter in a manner which suggested dependence on cold work. It was concluded that the cold work had reduced the thickness of the needles of niobium below the superconducting penetration depth, and had brought them sufficiently close together to allow the superconducting correlation to interconnect the niobium, in the manner suggested by Cooper; furthermore, the constant critical current region may possibly extend to considerably higher fields.

*   Research Assistant, Department of Metallurgy, Massachusetts Institute of Technology

** Assistant Professor of Metallurgy, Massachusetts Institute of Technology

*** Professor of Metallurgy, Massachusetts Institute of Technology

I. INTRODUCTION

Since the discovery of the high-field, high-current superconducting compounds Nb_3Sn (1) and V_3Ga (2), and the alloys Nb-Zr (3) and Nb-Ti (4), it has become apparent that the magnitudes of the critical currents and fields involved are related to the presence of a so-called "filamentary structure." In 1935, Mendelssohn (5) postulated a sponge-like network of material which was to possess a very high critical field compared to the matrix; this was necessary in order to explain the thermodynamic and magnetic properties of the "hard" superconductors. The general idea of finely divided superconducting domains, which may arise even in homogeneous materials, has been considered more recently by Abrikosov (6) and Goodman (7). The Ginzburg-Landau theory (8) allows for a class of materials in which the surface energy between normal and superconducting phases is negative; both Abrikosov and Goodman, following the letter inferences, have predicted "mixed state" critical fields considerably in excess of the bulk critical field. Whatever the case, it

1. J. E. Kunzler, E. Buehler, F. S. L. Hsu, and J. H. Wernick, Phys. Rev. Letters 6, 89 (1961)

2. J. H. Wernick, F. J. Morin, F. S. L. Hsu, D. Dorsi, J. P. Maita, and J. E. Kunzler, High Magnetic Fields, M.I.T. Press, Cambridge, Mass. and John Wiley & Sons, Inc., New York (1962) p. 609

3. T. G. Berlincourt, R. R. Hake, and D. H. Leslie, Phys. Rev. Letters 6, 671 (1961)

4. T. G. Berlincourt, to be published

5. K. Mendelssohn, Proc. Roy. Soc. A152, 34 (1935)

6. A. A. Abrikosov, J.E.T.P. 32, 1442 (1957)

7. B. B. Goodman, Phys. Rev. Letters 6, 597 (1961)

8. V. L. Ginzburg and L. D. Landau, J.E.T.P. 20, 1064 (1950)

appears, from thermodynamic considerations, that very high critical fields cannot
be a bulk property.(9) Furthermore, Gorter has pointed out that a filamentary
structure such as the Goodman-Abrikosov mixed state in a "homogeneous" material,
is not capable of carrying a net current, unless it is constrained in some way.(10)
As a result, the microstructure of a hard superconductor may be expected to contain
some regular feature capable of localizing or stabilizing the filamentary network.

The theories of London (11), Pippard (12), Ginzburg and Landau (8), and the
approximate synthesis by Ittner (13) of the microscopic BCS theory (14), all
predict the finite penetration of magnetic field into superconductors, and very
large enhancement of critical field when the dimension(s) of the superconductor
becomes small compared to the characteristic penetration depth. Hauser and
Helfand (15) have computed the critical fields corresponding to various geometric
shapes, for the different theories. In addition, if field penetration is complete,
the critical current is expected to be independent of field.(16) The possibility
therefore arises that very hard superconductors may be synthesized by suitable

9. D. Shoenberg, Superconductivity, Cambridge U. Press, London (1960), p. 47

10. C. J. Gorter, VIIIth Int. Conf. on Low Temp. Phys., London (1962)

11. F. London, Superfluids, vol. I, Dover (1961), p. 27

12. A. B. Pippard, Proc. Roy. Soc. A216, 547 (1953)

13. W. B. Ittner, III, Phys. Rev. 119, 1591 (1960)

14. J. Bardeen, L. N. Cooper, and J. R. Schrieffer, Phys. Rev. 108, 1175 (1957)

15. J. J. Hauser and E. Helfand, Phys. Rev. 127, 386 (1962)

16. See Ref. 9, p. 175

manipulation of the microstructure to achieve networks of thin superconducting filaments. Bean and co-workers (17) have succeeded in the above by pressing mercury into porous Vycor glass; the critical field in this case was at least twenty times greater than the critical field of bulk mercury, and the measured critical currents in the filaments were independent of applied field.

Eutectic and eutectoid alloys lend themselves naturally to the synthesis of filamentary structures. Tiller (18) has analyzed extensively the problem of solidification of eutectic alloys; the resultant structures, according to the theory, may be lamellar (plate-like), acicular (rod-like), or spherical particles of one phase, dispersed in the other. Consequently, a eutectic alloy of one strongly superconducting component, and one weak or non-superconducting component, appeared to be a good basis. Other desirable properties were: (a) negligible solubility of the weak superconductor in the strong superconductor to minimize solid-solution effects; (b) room-temperature stability of the microstructure. The above considerations led to the choice of the niobium-thorium eutectic alloy for experimentation; the solubility of thorium in niobium is negligible, (19) and both metals have high melting points.

17. C. P. Bean, M. V. Doyle, and A. G. Pincus, Phys. Rev. Letters 9, 93 (1962)

18. W. A. Tiller, Liquid Metals and Solidification, American Society for Metals, (1958), 276

19. O. N. Carlson, J. M. Dickinson, H. E. Lunt, and H. A. Wilhelm, Trans. AIME 206, 132 (1956)

II. EXPERIMENTAL PROCEDURE

The initial ingot was made up of a 5% Nb-95% Th mixture (by weight), in a niobium tube (see Fig. 1). The ingot was then heated to 1500°C in vacuo, and the thorium-rich core melted; this temperature was held for five minutes, during which a portion of the inner wall of the niobium tube partially dissolved in the liquid. Cooling to room temperature was accomplished by quenching with helium gas; it was hoped that a sufficiently large cooling rate would result in a finer dispersion of the eutectic structure. The "history" of the ingot is shown schematically in Figure 2a; Figure 2b plots time vs. temperature (optical pyrometer) for the quench.

Other ingots were made up by various techniques. A faster cooling rate was achieved by transferring the material to a "cold zone" whose walls were water-cooled; electron-beam zone melting at a relatively rapid rate (4 mm. per minute) was also used. Finally, a slow zone melting rate was used (0.2 mm. per minute) with induction heating.

The ingots were swaged down to 0.035", and then drawn through wire dies to 0.019"; some of this wire was then drawn down further to 0.013". Some wire of 0.019" diameter was etched to remove the niobium jacket from the Nb-Th core. Current leads were made by combining ultrasonic soldering and cold welding (20); voltage loads were attached across a 1/2" section of the wire. Measurements were made in liquid helium, using the Bitter solenoids of the M.I.T. National Magnet Laboratory.

20. K. M. Ralls, A. L. Donlevy, R. M. Rose, and J. Wulff, to be published.

III. EXPERIMENTAL RESULTS

Microstructure

The eutectic structure of the solidified ingot was acicular, with evidence of primary niobium (solid solution) between the eutectic colonies; Figures 3a-c show typical microstructures. Figures 3a and 3b are of the ingot whose material was later used to make wire for the superconducting measurements (Figure 4). Figure 3c is of an ingot which was cooled at a more rapid rate. The slowly cooled ingot, which was made by induction-heated zone melting, had a spheroidized microstructure, i.e., spheres of niobium in a thorium matrix. The electron-beam melted ingot had a structure similar to that of Figures 3a and 3b. Measurement of the diameters of the thinnest rods of niobium at a total magnification of 1500X showed this dimension to range from 5000 to 10,000 Å. The structure of the wire at its final diameter was impossible to resolve optically.

Critical Currents

Measurements on the electron-beam melted ingot indicated that it was normal at 4.2°K; however, the resistance increased markedly with magnetic field, approaching asymptotically a constant value at fields in excess of 10 kilogauss.

The wire from the helium-gas quenched ingot (see Figures 3a, b) was made up into specimens for high-field testing. The critical current density in the Nb-Th core of the best specimen was essentially independent of magnetic field, from five kilogauss to the highest field used, 82.5 kilogauss. The critical current vs. transverse field curve, with 10^{-7} volts used to define the transition, is presented in Figure 4.

The critical current density in the core of the 0.013" total diameter wire (Nb-Th core diameter 0.008") dropped from very large values below 5 kilogauss to a constant value of 2×10^{4} amps/cm^2 for the higher fields; this corresponds to

a current of about 8 amperes. If 10^{-6} volts are used instead as a standard for the transition, the critical current density in the plateau region is 3×10^4 amps/cm^2. Boiling of the liquid helium was observed when the current exceeded 4 amperes at the higher fields.

Measurements were also made in a smaller magnet which was mounted goniometrically; the critical current at 8.8 kilogauss, when plotted on polar coordinates, resulted in an ellipse. The major and minor axes of the ellipse corresponded to the longitudinal and transverse field orientations, respectively; the ratio between these critical currents, transverse to longitudinal, was 0.7.

The larger diameter wires (see Figure 4) yielded similar but quantitatively different results. The plateau, which ran from about 20 to 82.5 kilogauss for the 0.013" diameter cores, was between 10 and 30 amps/cm^2.

In some other cases, difficulty was encountered -- very violent boiling was sometimes observed; sometimes negative (i.e., indicative of negative resistance) voltages occurred. A few specimens did not have current plateaus at high field, but were normal above 8 kilogauss.

IV. DISCUSSION

Microstructure

The presence of primary niobium in the microstructure (see Figures 3a-b) is simply the result of the dissolution of the inner walls of the Nb tube; the hypothetical "history" of the ingot is indicated on the phase diagram (Figure 2a) by the dotted path ABC. The niobium tube, which provides mechanical and chemical protection during processing and handling, has little influence on the high-field critical current (See Figure 4). If uniform deformation of the entire specimen during reduction of the core to 0.008" diameter is assumed, the thinnest needles in the microstructure would be reduced in diameter by a factor of 30, and elongated

by a factor of 900. The filament dimensions, according to this simple viewpoint, would be approximately 200 Å diameter for the thinnest niobium filaments, and 2000 Å for the primary niobium. The thinnest filaments would then be at least 1/2" long.

There is some evidence (18) that the axes of acicular and lamellar eutectic structures grow from the liquid parallel to the thermal gradient. The sharpness of the temperature gradient, and the cooling rate, are the chief factors in determining the size and morphology of the phase distribution. In particular, the thickness of the niobium filaments might be reduced further by faster cooling rates; the latter are easily achieved. Furthermore, considerable control over eutectic alignment is possible, by control of the temperature gradient. Very large, perfectly parallel lamellae of lead-tin eutectic have been grown in our laboratory. (21)

High-field Superconductivity

The highest field used is at least 40 times larger than the bulk critical field of pure niobium, (22) and at least ten times the critical field of cold-worked commercial niobium wire. (23) The shape of the critical current density vs. transverse magnetic field curve is consistent with the microstructural evidence. The critical current "plateau" indicates that the current-carrying filaments are much smaller than the penetration depth at high fields; the steep low-field portion is the contribution of the primary niobium, and, to some extent, the jacket. If the critical current density of the thin filaments is independent of size,

---

21. G. Beske, G. W. Pearsall, and J. Wulff, to be published.

22. See Ref. 9, p. 224.

23. L. C. Skinner, S.B. Thesis, M.I.T. Department of Physics, 1962

the critical current of the entire specimen would be at high fields a very sensitive function of the connectivity of the filamentary structure. The ingot in the as-solidified state is normal, although there is evidence (see results) of superconducting inclusions, i.e., the discontinuous eutectic and primary niobium. The elongation of the filaments and their decreasing separation as the specimen diameter is reduced by plastic deformation increase the connectivity of the niobium network, until a continuous superconducting path is possible. The very large difference in the magnitudes of the high-field current plateaus of Figure 4, illustrates the increase in connectivity of the niobium filaments as the Nb-Th core is worked down from 0.013" to 0.008".

Because the thickness of the niobium phase is probably considerably smaller than the superconducting coherency distance (12), it is possible, as Cooper (24) has pointed out, that the normal material adjacent to the niobium, i.e., the thorium, may itself be superconducting. This is also a plausible mechanism whereby the superconducting path may be established between the filaments, as the ingot is reduced. As the inter-filament distance decreases, some critical diameter is reached, which corresponds to the establishment of coherency or con- tinuity between the filaments. It is also possible that the above effect compli- cates the rather simple model assumed herein for the structure of the superconduct- ing state of this alloy.

V. CONCLUSIONS

(a) Proper treatment of the niobium-thorium eutectic alloy has resulted in critical current densities of 2×10^4 amperes per square centimeter at the highest field used, 82.5 kilogauss. For fields in excess of 20 kilogauss, the critical

---

24. L. N. Cooper, I.B.M. J. Res. Dev. 6, (1962), 75.

current density is substantially independent of field, and therefore high critical current densities at fields considerably higher than 82.5 kilogauss are possible.

(b) The high-field properties of the above alloy may be explained most simply by viewing the microstructure as a composite of very thin filaments of niobium.

(c) The number of superconducting paths in the specimen increases with increasing plastic deformation; the mechanism by which continuity is established may be that of Cooper. (24)

ACKNOWLEDGMENTS

FIGURE CAPTION LIST

Fig. 1 Schematic of experimental ingot.

Fig. 2 (a) The niobium-thorium phase diagram; ingot history is indicated by path ABC.

(b) Cooling curve for ingot, as determined by optical pyrometer.

Fig. 3 (a) Microstructure of the ingot (helium-quenched) after solidification. 150X; etched with dilute HNO_3.

(b) Microstructure of the ingot (helium-quenched) after solidification. 500X; etched with dilute HNO_3.

(c) Microstructure of rapidly cooled ingot after solidification (argon-quenched). 1000X; etched with dilute HNO_3. A particularly good example of the acicular nature of the rapidly cooled Nb-Th eutectic.

Fig. 4 Critical current density vs. transverse magnetic field at 4.2°K; material from helium-quenched ingot, reduced to diameters indicated by swaging and drawing.
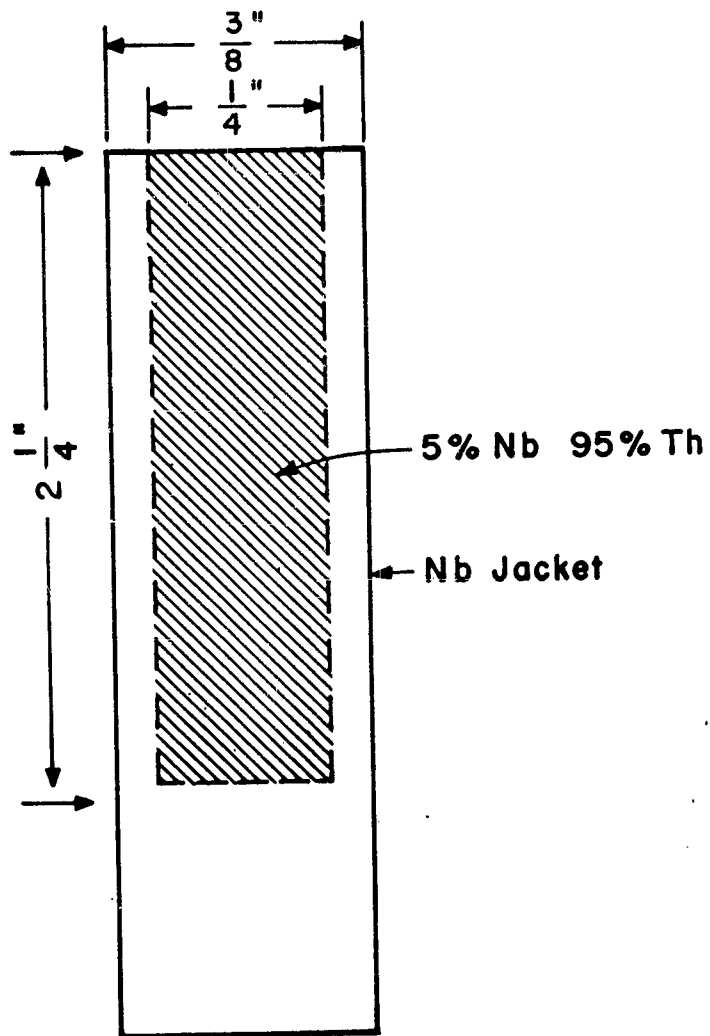
FIGURE 1

FIGURE 2(b)

FIGURE 2(a)

Figure 3a: Microstructure of the ingot
after solidification. 150 X magnifi-
cation. Etchant: dilute HNO_3.
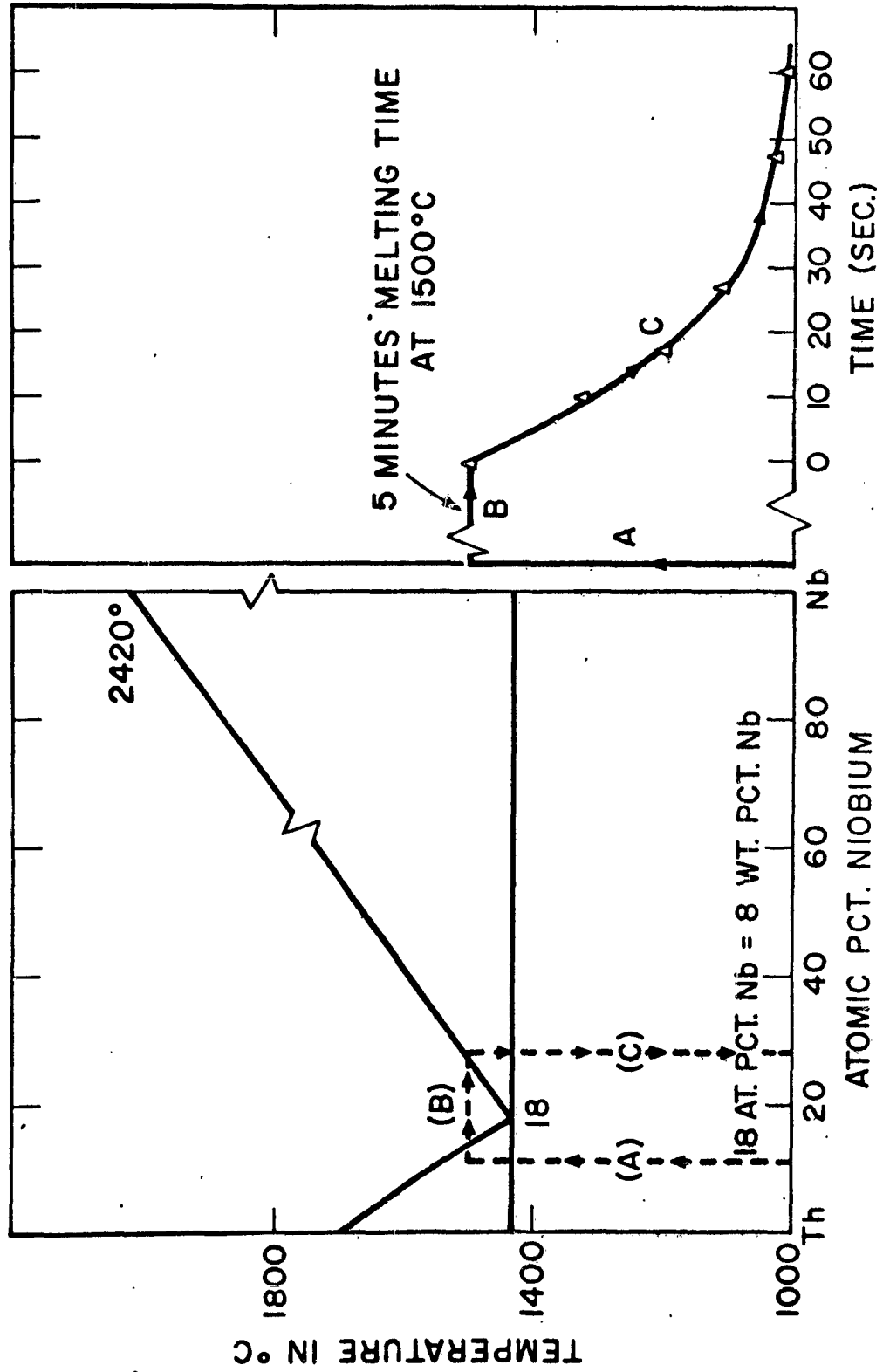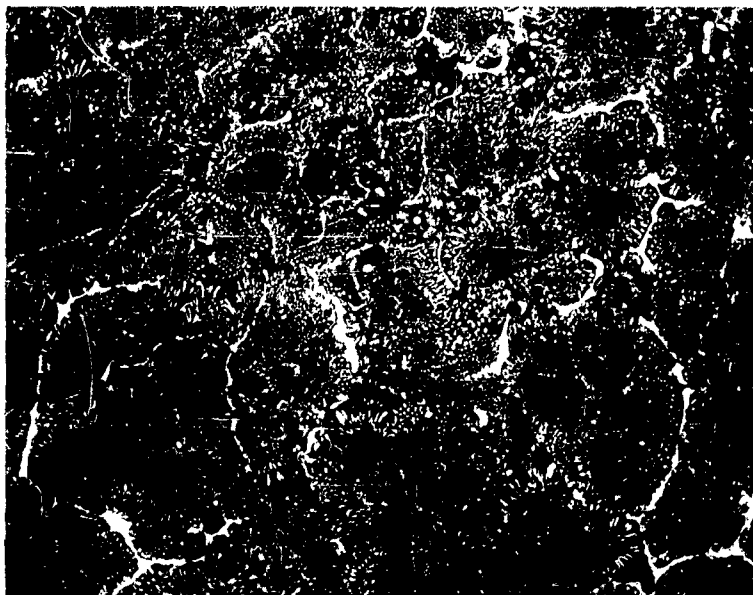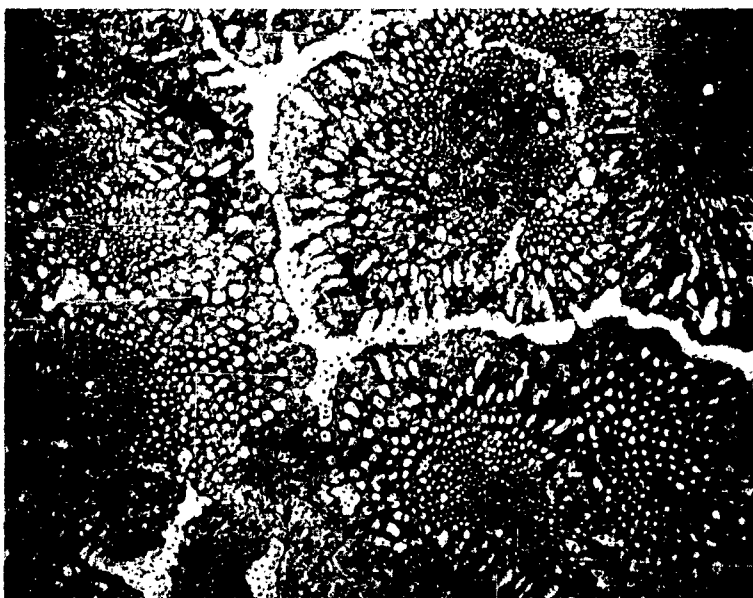

Figure 3b: Microstructure of the ingot
after solidification. 500 X magnification.
Etchant: dilute HNO_3.
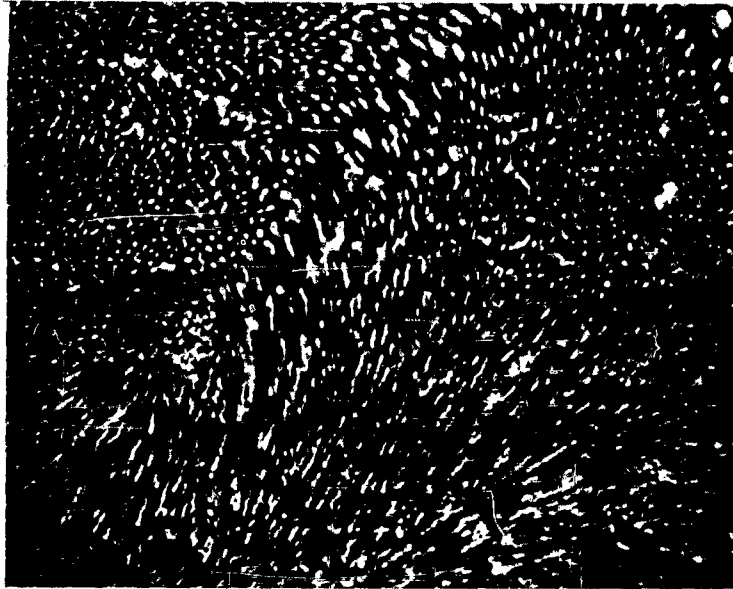
Figure 3c: Microstructure of a rapidly-cooled ingot, after solidification. 1000 X magnification. Etchant: dilute HNO_3. A particularly good example of the acicular nature of the Nb-Th eutectic.

FIGURE 4
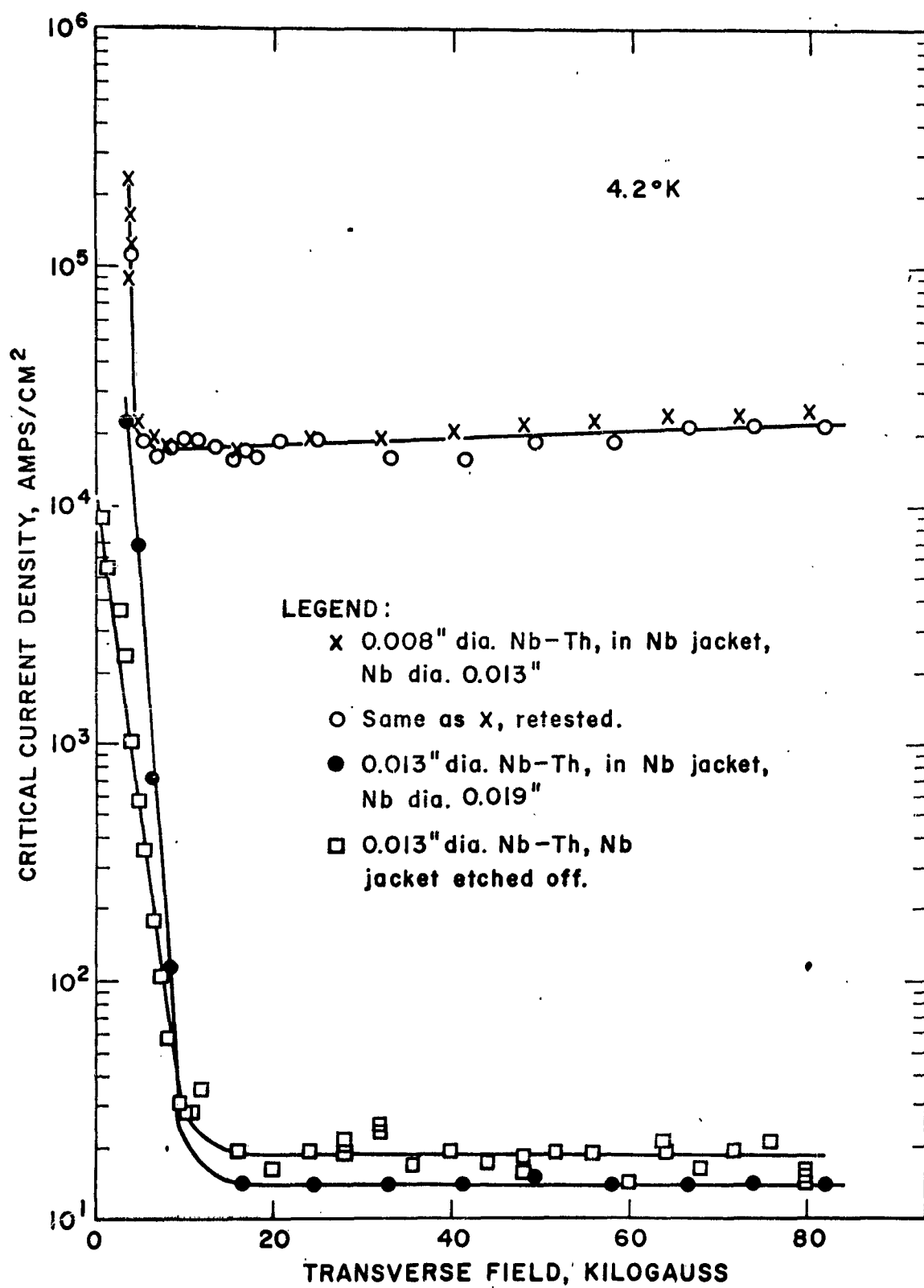
2.0   Large Volume Superconduction Solenoid

<u>Research Report</u>

G. SUPERCONDUCTING SOLENOID

1. Test of a Large Superconducting Coil

While the construction of the vessel and accessories of the large superconducting magnet[1] is progressing satisfactorily, we have proceeded to test a set of three coils in order to evaluate and choose the best design to be used for the remaining coils of the larger magnet. We have also developed an IBM 7090 computer program for the calculation of the magnetic field in any coil or set of coils.

The three coils have been tested in a vertical 14.00-in. liquid-helium dewar.[2] Figures XIV-8, XIV-9, and XIV-10 show close-up views of the coil X1 alone, the set of three coils, and the coil assembly with the dewar.

The specifications of the coils are given in Table XIV-6. Their differences are essentially in the winding, which for the coil X1 was made by using insulated Nb-Zr wire; some copper wire was wound inside and outside for the purpose of protection. For coil X2, the same insulated superconducting wire was used, but it was wound with bifilar copper magnet wire. Finally, coil X3 was made by using insulated copper-plated Nb-Zr, 0.0012 in. thick. No secondary copper winding was used. Figure XIV-11 shows the detail of the winding of coil X1.

Coil X1, which was ready first, underwent the most intensive testing, both alone and with the two other coils.

Intensive investigation of the quenching characteristics has been carried out in order to find the eventual training effect, deterioration of the critical current of the coil and energy balance in the various circuits, as well as the quenching current.

The listings in Table XIV-6 also indicate that the training effect was nonexistent for the three coils and, moreover, that the quenching current is not associated with the rate at which the current is increased (from 20 seconds to 5 minutes for a full increase). For coils X1 and X3 no deterioration of their properties was observed, although the energy involved became quite large (5 kilojoules with the three coils running). The recovery time after quenching is approximately 20 seconds. The deterioration of coil X2 has been found to be due to a kink in the wire which progresses up to a complete break.

The transient phenomena that occur at quenching have been recorded with an oscilloscope for coil X1 only. We have not been able to record the transient in coil X3, probably because of too small a rate of quenching. Figures XIV-12 and XIV-13 illustrate the basic process of quenching. For a single winding, the current decay is approximately 0.030 second. When two windings are separately driven, there is quite a big delay (0.260 sec) between the quenching of the two coils.

By integration of the transient curve of the copper coil, one can calculate the energy that has been dissipated in its external resistance (3 ohms). It appears that in our case only 2 per cent of the magnetic energy has been dissipated into the external resistance.

contain two rows of fins to improve the heat removal. Water is circulated in through a peripheral sleeve, and out axially. The electrodes can slide axially through O-ring seals in the end flanges of the side arms. The power supply consists of two AIRCO welding rectifiers in series, giving 200 amps at 80 volts under load. A spark-gap oscillator is included in the circuit as starter; a filter reduces the ripple to less than 1 per cent.

To probe the hollow-cathode discharge, whose maximum length can be 1.6 meters, Langmuir probes are used. Two of these, rigidly connected, are installed; they can be moved parallel to the mirror axis and rotated in a normal plane. The probe tip describes a circular path, 45° wide, through the mirror axis. The probes are placed 75 cm apart on a supporting arm 1.9 meters long. Each probe tip can span 80 cm of the arc; overlap of the two probe positions allows for reciprocal calibration. The movement is imposed from the outside through a sliding O-ring seal in the end flange. The stainless-steel holder arm contains and seals the probe leads; it is longitudinally supported in the tank by a coaxial cylindrical rail, 2.0 meters long. The rail also serves as screen against the sputtering from the arm.

F. Alvarez de Toledo

References

1. W. D. Getty, A low-pressure gas-arc discharge, Quarterly Progress Report No. 57, Research Laboratory of Electronics, M.I.T., April 15, 1960, pp. 27-29.

F. ENERGY EXTRACTION BLANKET FOR A FUSION REACTOR

Work on nonfissile systems has been completed and final reports are being prepared as theses[1,2] for submission to the Department of Nuclear Engineering, M.I.T.

Heating calculations have revealed that each 14.2 Mev D-T neutron will produce approximately 17.5 Mev of recoverable heat in the blanket. The maximum energy flux of 14.2 Mev neutrons that can be tolerated on a 2-cm molybdenum first wall is 4-5 Mw/m^2. Thermal stress and heat transfer to a fused Li$_2$BeF$_4$ coolant are both limiting at this power. The total blanket thickness necessary to shield superconducting coils is 110-120 cm.

W. G. Homeyer, A. J. Impink, Jr., D. J. Rose, I. Kaplan

References

1. W. G. Homeyer, Thermal and Chemical Aspects of the Thermonuclear Blanket Problem, Sc.D. Thesis, Department of Nuclear Engineering, M.I.T., December 1962.

2. A. J. Impink, Jr., Neutron Economy in Fusion Reactor Blanket Assemblies, Ph.D. Thesis, Department of Nuclear Engineering, M.I.T., January 1963.

Table XIV-6.   Coil data and results of the tests.

	X1 inner	X1 outer	X1 total	X2 inner (bifilar)	X2 outer	X2 total	X3 total (copper-plated)	Notes
I.D. (in.)	11.562	12.584	11.562	11.390	12.696	11.390	11.390	( ) average value
Turn spacing	0.0124	0.0127	0.0126	0.0257	0.0116	(0.0190)	0.0144	
Layer spacing	0.020	0.020	0.020	0.0172	0.022	(0.0202)	0.0242	Length of each winding: 1.750 in.
Space factor (%)	31.7	30.9	31.2	17.8	30.5	(20.4)	22.5	
Turns	1841	2740	4581	2580	1661	4241	4449	
Length of wire (ft)	5745	9363	15109	8419	5738	13757	14930	
Quenching current								
Minimum	20.0	16.0	15.1	15.1	16.0	11.5	20.0	
Maximum	22.7	19.0	16.7	18.5	18.5	15.5	22.0	
Average	22.0	18.0	16.0	(17.0)	(17.0)	(15.0)	21.5	
B av quench (kg) (central field)	0.818	1.880	2.880	1.080	1.780	2.500	3.750	
Number of quenches	46	10	57	8	10	10	10	
Training	No	No	No			Yes	No	
Deterioration	No	No	No			Yes	No	

Maximum field recorded with the three coils running together. 5,600 kgauss on the axis, that is, 11,000 gauss on the edge of the coil.

Fig. XIV-9. Three-coil arrangement with the terminal switches inside the coils.

Fig. XIV-8. Coil X1 with its connections.
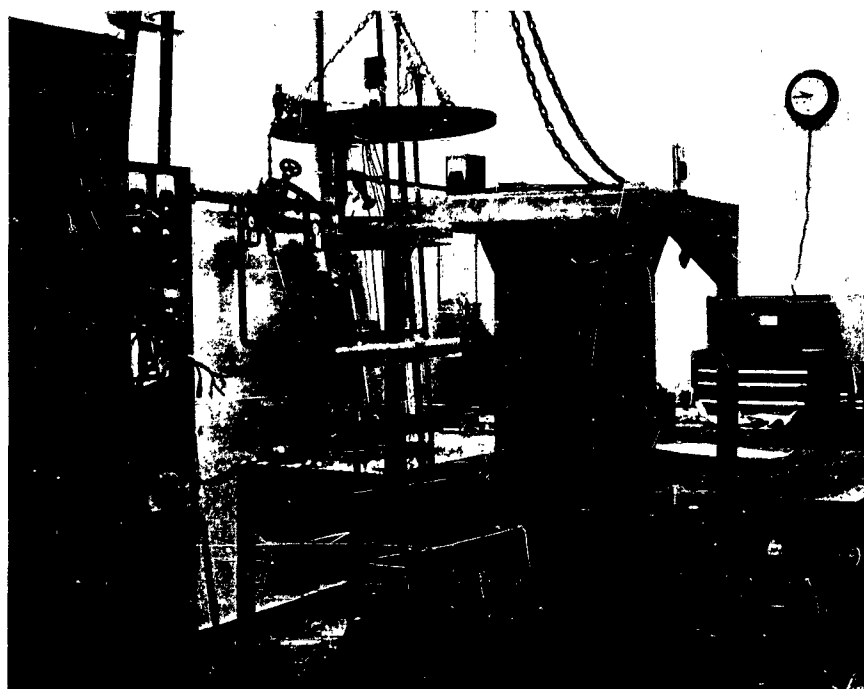
Fig. XIV-10. Coil X1 with its support, the 14-in. dewar.
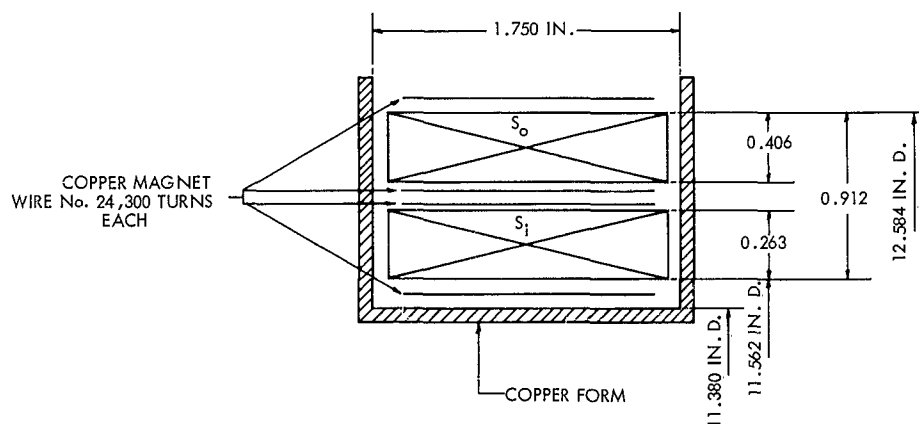
S_i INSIDE SUPERCONDUCTING WINDING - 1841 TURNS IN 13.13 LAYERS SEPARATED WITH 0.075 IN. MYLAR FOIL SPACE FACTOR 31.7%- 5745 FT.,1.681 LBS. OF Nb-Zr WIRE

S_o OUTSIDE SUPERCONDUCTING WINDING - 2740 TURNS IN 20.27 LAYERS SEPARATED WITY 0.075 MYLAR FOIL SPACE FACTOR 30.9%- 9363 FT.,2.816 LBS OF Nb-Zr WIRE

ALL THE WINDING IS ENCAPSULATED INTO AIR-DRY VARNISH (No.=301 OF PEDIGREE COMPANY)

Fig. XIV-11. Schematic cutaway of the winding
of the X1 coil.
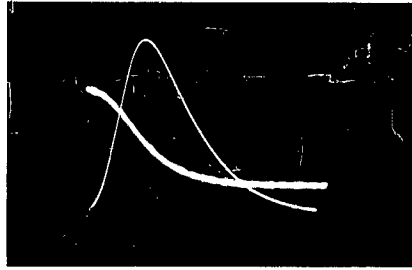
Fig. XIV-12. Quenching transient for inner coil. The bell-shaped curve is the voltage (across a 3-ohm resistor) of the current in the copper coil. Scale, 5 volts/cm. The other curve is the decay of the superconducting current, 5 amp/cm. Time scale, 5 msec/cm. Quenching time, 30 msec.
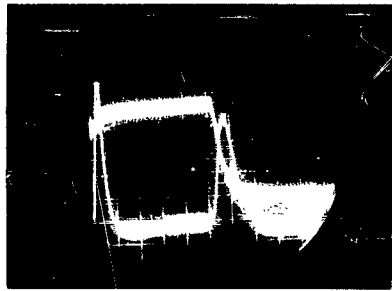
Fig. XIV-13. Quenching transient for the two windings in parallel. The curve with two peaks is for the copper coil (5 volts/cm across 3 ohms). Other curve is for the current in the inner coil (5 amps/cm). Time scale, 50 msec/cm. Quenching occurs in 2 steps: first, the outer coil quenches and current rises in the inner coil; second, after 0.260 sec the inner coil quenches. Each quenching takes approximately 30 msec.

This is due certainly to the large energy dissipation in the copper coil form, which was detected by a quick rise of its temperature.

The behavior of the copper-plated coil, X3, was found to be much more satisfactory than that of the two other coils in all respects. Its operation seems more stable, and it is possible to reach and maintain the current within a few per cent of the maximum value of the current. Moreover, its performances are approximately 30 per cent better than those of the other coils. Consequently, all of the remaining coils will be made of copper-plated wire similar to that used for coil X3.

The coils have been operated in the permanent current states, and differential
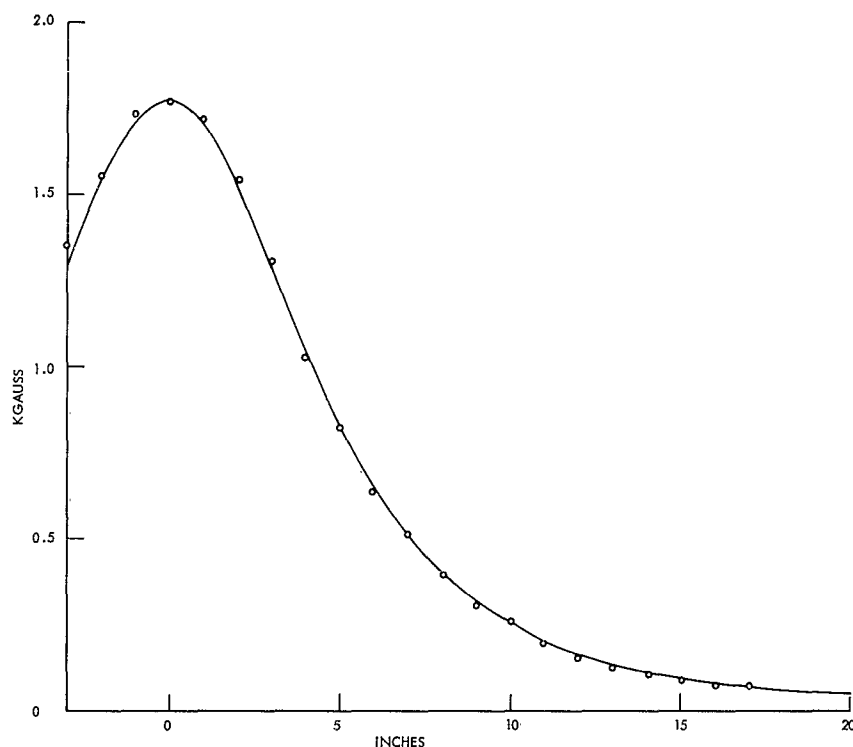
Fig. XIV-14.   Field plot of coil X3 in permanent state. Current, 10 amps. The curve represents calculated values; measured values are plotted as ○.

measurement of the magnetic field leads to the conclusion that there is no decay of the field (say, less than 10^{-4} per hour measured). The field plot measured in the permanent current state is shown in Fig. XIV-4 with the calculated value. The thermal switches operate very satisfactorily. Their power consumption is 0.150 watt for warming up the gate wire to the critical temperature, and their switching takes approximately 1 second.

We have been able to pump the field from the X3 coil to the X1 and X2 coils by using the proper switching sequence in and out of the permanent mode. The highest field produced has been achieved in this way.

The clamped contacts have shown a contact resistance of the order of 10^{-7} ohms, which is also quite satisfactory.

2. Magnetic Field Calculation

An IBM 7090 computer program has been developed[3] for the calculation of both components of the magnetic field at any location of a solenoid, including the winding interior.

Fig. XIV-15. Coordinates used in calculation of the magnetic vector potential and magnetic field for a cylindrical geometry.

The program was then extended to calculate for a multicoil solenoid, for the reciprocal case of the determination of the current that will produce a given magnetic-field shape, and for the field of a uniformly distributed dipole in a solenoidal winding. All three cases are important for the evaluation of the performance of superconducting solenoids.

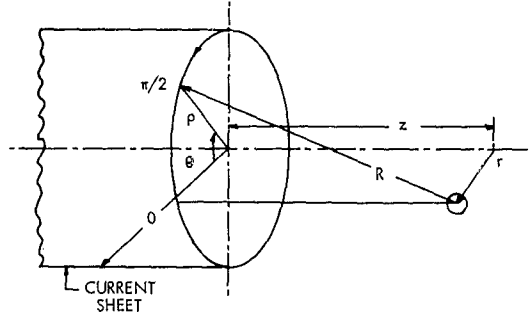The principle of these field calculations is based on the splitting of the winding in several current sheets. We assume a uniform distribution on the current throughout the winding. It can be noted, then, that the program can be easily modified to fit any current distribution by weighting each current sheet accordingly.

The field is derived from the expression of the vector potential of a current loop[4-7]

$$A(r,z) = \frac{1}{2\pi} \int_0^\pi \frac{\cos\theta}{R}\, d\theta, \tag{1}$$

where R is the distance between the field point and the source point as shown in Fig. XIV-15:

$$R = [r^2 - 2r\cos\theta + 1 + z^2]^{1/2}. \tag{2}$$

The distances are normalized to the radius of the current sheet, and the vector potential (and subsequently the field) to the value of an infinitely long solenoid, that is, $\left(\mu\frac{NI}{L}\text{ in mks units or }\frac{4\pi}{10}\frac{NI}{L}\text{ in cgs units}\right)$.

For a current sheet extending from $z = S_1$ to $z = S_2$, the magnetic potential is

$$S(r,z) = \frac{1}{2\pi} \int_{S_1}^{S_2} \int_0^\pi \frac{\cos\theta}{R}\, d\theta\, ds. \tag{3}$$

If the order of integration is inverted, the integration with respect to S carried out, the angular integration modified by using the identity

$$\int_0^\pi F(\cos\theta)\, d\theta = \int_0^{\pi/2} F(\cos\theta)\, d\theta + F(-\cos\theta)\, d\theta, \tag{4}$$

and the origin S_1 extended to infinity, one obtains the vector potential of a semi-infinite current sheet:

$$A(r,z) = \frac{1}{2\pi} \int_0^{\pi/2} d\theta \cos\theta \ln \frac{z + \sqrt{z^2 + r^2 + 1 + 2r\cos\theta}}{z + \sqrt{z^2 + r^2 + 1 - 2r\cos\theta}} \tag{5}$$

The radial and axial magnetic fields are derived from the vector potential and are given by

$$H_r(r, z) = -\frac{\partial A(r, z)}{\partial z} \tag{6}$$

$$H_z(r, z) = \frac{1}{r}\frac{\partial}{\partial r}(rA(r, z)), \tag{7}$$

which, applied to Eq. 5, give

$$H_r(r, z) = \frac{2}{\pi} r \int_0^{\pi/2} \frac{\cos^2\theta\, d\theta}{Q_+ Q_- (Q_+ + Q_-)} \tag{8}$$

and

$$H_z(r, z) = \frac{1}{2\pi}\int_0^{\pi/2} d\theta\, \cos\theta\left[\frac{1}{r}\ln\frac{z+Q_+}{z+Q_-} + \frac{2\cos\theta}{(z+Q_+)(z+Q_-)(Q_++Q_-)}\right.$$

$$\left. \times \left(\left(\frac{z^2+1-r^2}{Q_+ Q_-}\right)(z+Q_++Q_-)+z\right)\right]. \tag{9}$$

Here,

$$Q_+ = \sqrt{z^2 + r^2 + 1 + 2r\cos\theta} \tag{10}$$

$$Q_- = \sqrt{z^2 + r^2 + 1 - 2r\cos\theta}. \tag{11}$$

The field of a finite current sheet is obtained by superposition of negative and positive semi-infinite sheets:

$$H_{sol}(r, z) = H_{(r, z)} - H_{(r, z+s)},$$

where s is the normalized length of the solenoid.

From the basic current sheet calculations, the field is obtained by summation of current sheets.

$$H(r, z) = \sum_{n=1}^{N} H(r_s(n), z)/N, \tag{12}$$

where $r_s(n)$ is the relative radial distance of the field point with respect to the particular current sheet.

$$r_s(n) = r/\rho(n). \tag{13}$$

Several problems arise in the evaluation of the integrals. For z negative and $\theta = 0$, $Q_- = |z|$, so that $(z+Q_-) = 0$ and the integrand of H_z becomes infinite. This inconvenience is solved by using the following identity proper to a semi-infinite current sheet

$$
\left.
\begin{array}{lll}
r < 1.0 & H_z(r, -z) = -H_z(r, z) + 1.0 \\
r = 1.0 & H_z(r, -z) = -H_z(r, z) + 0.5 \\
r > 1.0 & H_z(r, -z) = -H_z(r, z)
\end{array}
\right\} \tag{14}
$$

For z = 0

$$r < 1.0 \qquad H_z(r, 0) = 0.5$$
$$r = 1.0 \qquad H_z(r, 0) = 0.25 \qquad\qquad (15)$$
$$r > 1.0 \qquad H_z(r, 0) = 0.0$$

Also, $H_r(r, z) = H_r(r, -z)$.

When $|r-1|$ and z both approach zero, the integrands of both H_r and H_z become very large when θ is small; indeed $Q_- \to 0.0$ for $|r-1|$, z, and $\theta \to 0.0$. Therefore, in order to conserve accuracy in the numerical integration, it has been found necessary to split the integration with emphasis in the range of $\theta \approx 0.0$. Various test runs, comparing the calculated values with those of Alexander and Downing,[6] have shown that the best accuracy was obtained with a three-part splitting, that is,

$$\int_0^{\pi/2} = \int_0^{0.0625} + \int_{0.0625}^{0.250} + \int_{0.250}^{\pi/2}$$

and by calculating Q_- as

$$Q_- = \sqrt{z^2 + (r-1)^2 + 4r \sin^2 (\theta/2.0)} \qquad\qquad (16)$$

In such a way, an accuracy of the order of 10^{-6}, or better, can be maintained for $|r-1.0|$ and $|z| \geqslant 0.0005$, that is, well below any dimension of the wire used. The change from the single integration to a triple integration must occur in the vicinity of $|r-1.0|$ and $|z| \approx 0.4$.

Nevertheless, for $r = 1.0$ and $z = 0.0$, $H_r(1.0, 0.0) = \infty$. However, this is a purely mathematical conclusion, since, by definition, the thickness of the current sheet is zero, and the corresponding current density is infinite, a situation that never arises physically. To avoid such improper physical results, we stop the current sheet a distance ϵ from the corner, ϵ being less than the physical dimension of the actual current carrier. The use of a Gaussian integration procedure achieves the same purpose, since the lowest value of θ employed is not zero.

Finally, for $r = 0.0$, and for any z, the integrand of $H_z(r, z)$ again behaves badly for computation. However, in that case the field is calculated directly by integration of the Biot-Savard law for a thick solenoid of uniform current density.

$$H_z(0, z) = \frac{1}{2.0(\alpha-1)} \left[(\beta-\gamma) \ln \frac{\alpha + \sqrt{\alpha^2 + (\beta-\gamma)^2}}{1 + \sqrt{1 + (\beta-\gamma)^2}} + (\beta+\gamma) \ln \frac{\alpha + \sqrt{\alpha^2 + (\beta+\gamma)^2}}{1 + \sqrt{1 + (\beta+\gamma)^2}} \right] \qquad (17)$$

See **Fig. XIV-16** for definitions of α, β, and γ.

$$\alpha = \frac{D_o}{D_i} \qquad \beta = \frac{L}{D_i} \qquad \gamma = \frac{2.0 z_i}{D_i}$$
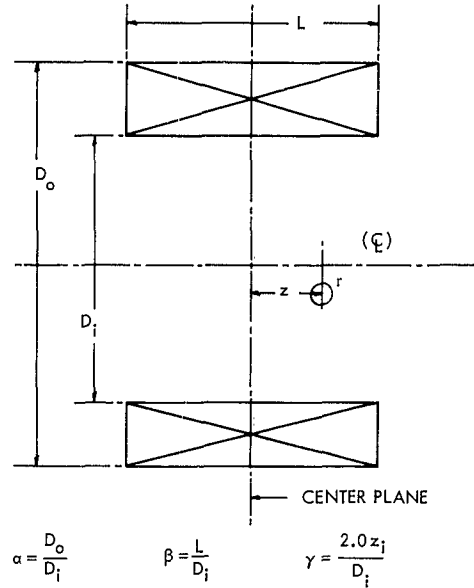
Fig. XIV-16. Configuration of a thick solenoid.

For a thin solenoid, $\alpha = 1.0$, and Eq. 17 becomes indeterminate. We replace it by the equation for the on-axis field of a current sheet

$$H_z(0, z) = \frac{1}{2.0} \left[\frac{\beta + \gamma}{\sqrt{1 + (\beta+\gamma)^2}} + \frac{\beta - \gamma}{\sqrt{1 + (\beta-\gamma)^2}} \right]. \tag{18}$$

Again, the field is normalized to the field of an infinitely long solenoid.

The program automatically provides selection between the various computation schemes so that the best accuracy and speed is obtained.

The numerical integration of Eqs. 2, 3, and 16 is carried out by a 10-point Gaussian quadrature. Test runs indicate that the accuracy is better than a 16-point Gaussian quadrature, probably because of less rounding-off error during the computation.

For a thick solenoid the accuracy may depend upon the number of current sheets in which the actual winding is split. When the field location is far away from the winding, fewer current sheets are required than when it is very close or inside the winding. There is no definite rule for selecting the optimum number of currents, and accuracy test runs must be made for each particular case. However, let us say that our results indicate that for a thin solenoid, that is, with thickness approximately 10 per cent of the radius, an accuracy of 10^{-5}, or better, is obtained with 5 current sheets for $r < 0.5$, and 10 current sheets for $r < 0.95$. Inside the winding, higher-order splitting is necessary, to approximately the same number as the physical number of layers,

that is, from 20 to 30.

The results also have been compared with those obtained by spherical harmonic expansion.[8,9] We have found that using three terms of the expansion gives only 10^{-3} accuracy within 15 per cent of the radius for the z component, and very much less for the r component. The discrepancy between the two methods increases quickly when $r > 0.5$, and no comparison can be made for $r \geq 1.0$ because of nonconvergence of the harmonic expansion.

The basic computation is carried out in a subprogram that calculates H_z and H_r when called by a main program or subprogram. The input data of the subprogram are the inside diameter of the solenoid, the winding thickness, the solenoid length, the number of current sheets in which the winding is split, and the radial and axial field position with respect to the center of the solenoid.

The basic time to calculate the contribution of one current sheet to the H_r and H_z fields takes approximately 0.05 second on the IBM 7090 computer.

Consequently, for a field position that is far enough away from the winding so that
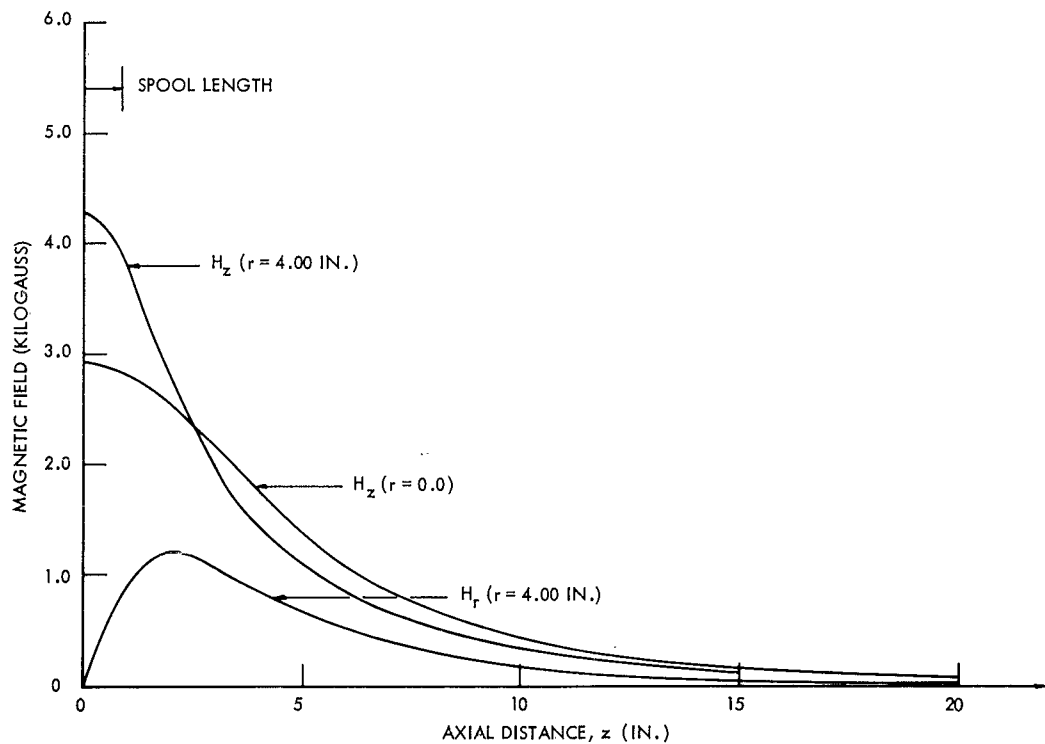
Fig. XIV-17.   Field variation along the axis for coil X1.
$a = 1.158$; $\beta = 0.151$.
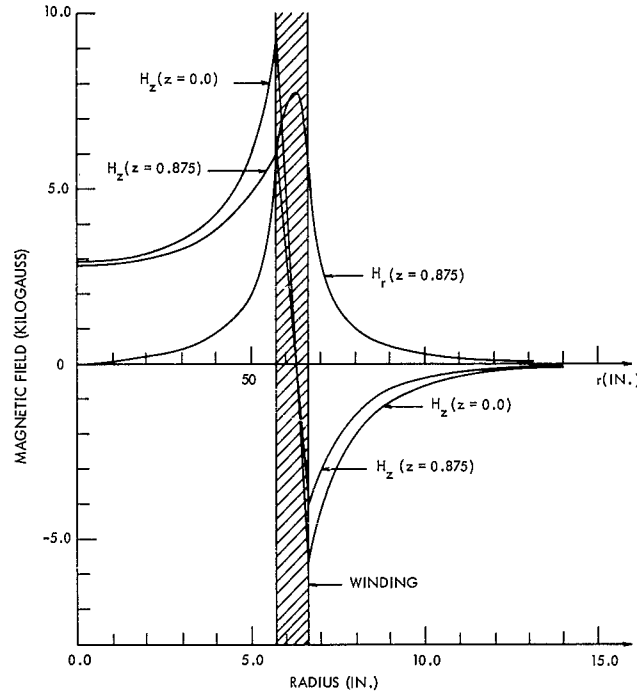
Fig. XIV-18.   Field variation along the radius for coil X1.
$a = 1.158$; $\beta = 0.151$. $Z = 0.875$ is at the
edge of the winding.

the integration is not split, that is, $|r-1|$ or $|z| > 0.4$, with the use of 5 current sheets, assumed the result is 0.25 second per point. If the field position is close to the edge of the winding, then the computation time is approximately three times longer. For any on-axis point, the use of Eq. 17 or Eq. 18 saves much more time and reduces the computation time to approximately 0.005 second.

We have applied the basic subprogram for the calculation of the field of a single solenoid and also for more complex problems.

For a multicoil solenoid, we simply used a summation of the two components of the field. Each coil is characterized independently.

$$H_{set}(r, z) = \sum_{i=1}^{P} H_{coil}(r, z_{(i)}) \times \frac{N_{(i)} J_{(i)}}{L_{(i)}} , \tag{19}$$

where $N_{(i)}$ is the number of turns, $J_{(i)}$ the current or current ratio, and $L_{(i)}$ the length of the ith coil.

The inverse problem consists in the determination of $J_{(i)}$ so that the field satisfies
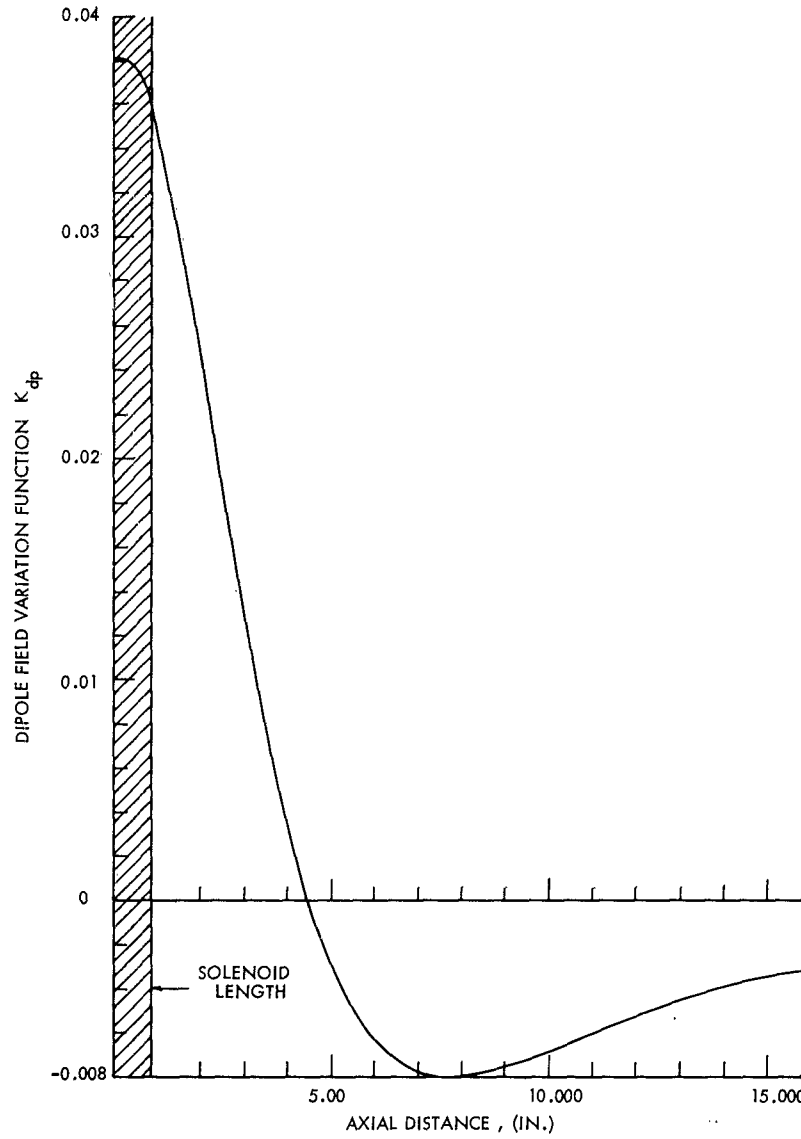
Fig. XIV-19. Axial dipole field of uniformly distributed dipoles in solenoid X1. $H_{gauss} = K_{dp} \times 19.3257 \times I_{amp}$. I_M = equivalent magnetization current.

a given value at P given positions. We have to solve the matrix equation

$$H_{(P)} = K_{(P, N)} J_{(N)};$$

(20)

thus

$$J_{(N)} = K^{-1}_{(P,N)} H_{(P)}.$$ (21)

This operation is easily carried out by the computer. Our program has been set to permit solving this problem when any series grouping of coils is devised.

Dipoles induced into a superconducting solenoid may be of prime importance for the limitation of the current into superconducting solenoids.[10] If we assume uniform distribution of dipoles throughout the winding, the magnetic field results from the superposition of two current sheets of equal strength of opposite direction, one along the inner diameter and the other along the outer diameter.

$$H_{dp} = H_{inner}(r,z) - H_{outer}(r,z)$$ (22)

The normalization factor of the field in that case is

$$K_{dp} = \mu \frac{I_M}{St} = \mu \frac{N_L}{L} I_M,$$ (23)

where St is turn spacing, N_L the number of turns per layer, L the length of the solenoid, and I_M the equivalent magnetization current.

For purposes of illustration we show in Figs. XIV-17, XIV-18, and XIV-19 the fields profiles and denote the field for the X1 coil which is described in the first part of this report.

L. J. Donadieu

References

1. L. J. Donadieu and D. J. Rose, Paper K4, International Conference on High Magnetic Fields, Massachusetts Institute of Technology, November 1-4, 1961.

2. We wish to thank Dr. Z. J. J. Stekly of the AVCO Everett Research Laboratories for the use of the dewar.

3. This work was partly done at the Computation Center, M. I. T.

4. W. R. Smythe, Static and Dynamic Electricity (McGraw-Hill Book Company, Inc., New York, 1950), p. 270.

5. C. Snow, Magnetic Fields of Cylindrical Coils and Annular Coils, National Bureau of Standards, Applied Math. Series, Paper No. 38, 1953.

6. N. B. Alexander and C. P. Downing, Tables for a Semi-Infinite Circular Current Sheet, ORNL-2828, October 13, 1959.

7. E. Durand, Electrostatique et Magnetostatique (Masson Companie, Paris, 1953).

8. D. B. Montgomery and J. Terrell, Some Useful Information for the Design of Air-Core Solenoids, AFOSR-1525, November 1961.

9. M. W. Garrett, J. Appl. Phys. 22 (1951).

10. D. B. Montgomery, Current Carrying Capacity of Superconducting Nb-Zr Solenoids, AFOSR-3015, National Magnet Laboratory, M. I. T., July 1962.

II. ELECTROCHEMICAL ENERGY CONVERSION RESEARCH

1.0 Fuel Cells

Personnel:

Professor Herman P. Meissner, Professor, Chemical Engineering
Gail D. Ulrich, Research Assistant, Chemical Engineering
Stephen G. Paradis, Research Assistant, Chemical Engineering
James P. Bell, Research Assistant, Chemical Engineering
Shing K. Chian, Research Assistant, Chemical Engineering
Herschel Clopper, Research Assistant, Chemical Engineering
Dennis F. Ripple, Research Assistant, Chemical Engineering

Research Report:

1.1 Summary

a) Formic acid is an intermediate formed in the oxidation of methanol and oxidizes with relative difficulty, hence its oxidation behavior influences the oxidation of methanol. Work done in this field is, summarized in the Doctoral thesis by Robert Slott entitled, "Electrochemical Oxidation of Formic Acid". A copy of this thesis (published as Scientific Report No. 5) accompanies this Semiannual Technical Report.

b) The work of the past two years on the flow electrode was reported in the Doctoral thesis of Adrian R. Reti entitled "Rate Limiting Steps on Fuel Cell Electrodes", dated June, 1962. Copies of this thesis were distributed last summer. Since then, theoretical and experimental studies in this area have continued. Considerable "paper" study has been devoted to the exploration of possible porous gas diffusion type electrode geometries whose design would permit the development of high current densities. The type of thinking involved is reviewed in Appendix I, which represents an early simplified version of a paper in preparation by H. P. Meissner and A. R. Reti. A preprint of a second paper in this field by these two authors, now submitted for publication, in also included.

Experimental studies of flow electrodes involve 1. A continuation of rate studies, 2. A preliminary investigation of the preparation of a

-13-

hydrazine electrode having a fair life, 3. Construction and test of a complete cell using "flow electrodes".

c) Heat effects at fuel cell electrodes, and the possibility of constructing a "thermocell" showing a high coefficient of performance, are under experimental and theoretical study.

1.2 Complete Cell

A small complete cell using "flow electrodes" has been assembled along the lines disclosed in the patent application submitted some months ago. This cell was designed to operate on hydrazine and peroxide, since it was judged that these two reagents would be the ones best suited to an early assembly of a complete cell. Unfortunately and unexpectedly the construction of a hydrazine electrode showing reasonable life has proven difficult. The problem of assembling a hydrazine electrode having reasonable ageing characteristics appears on the way to solution.

Detailed study of a complete cell was postponed until after having a proper hydrazine electrode available. These cell studies are now being resumed.

1.3 Hydrazine Electrode Studies

The electrodes used in these studies were platinum screens (80 mesh, with a wire diameter of 0.002 inches and a ratio of wire geometrical surface area to screen face area of unity) electroplated with either platinum, iridium, rhodium, or combinations thereof. For each type of plating, a wide range of plating current densities and plating times were explored.

The most successful metal coating was found to be rhodium. The platinum screen to be plated was always cut in a square shape, 1 cm. on a side. Before coating, the platinum screen was cleaned by washing first with benzene, then with acetone, distilled water, dilute H_2SO_4 and distilled water, after which it was cleaned electrolytically by being operated as an anode in 20% KOH for 5 minutes at 50 ma/cm^2 . The electrode was removed from this cleaning bath while under electrical load, and then again washed with distilled water. This was then immersed in a plating solution, and

surrounded by a cylindrical anode, again made of platinum screen. The dimension of this anode did not appear to be critical, but the anode cylinder used most often was about 1 inch in diameter by 3 inches high. The plating solution was 0.025 molar in rhodium, and was prepared by dissolving rhodium trichloride in aqua regia and diluting. Plating was always at 35°C, under conditions of constant stirring. The most successful rhodium plate was deposited using a current density of 100 ma/ cm^2 for 4 to 8 minutes (24 to 48 coulombs per square cm).

Electrodes were tested by obtaining a so-called "performance curve", namely a curve of voltage (measured against a standard hydrogen electrode connected to the test electrode through the usual Luggin capillary) versus current density. The electrolyte used in this work was 20% KOH , 1 molar in hydrazine. The dummy electrode used in these tests as anode was a sheet of platinum screen.

Ageing was determined by the deterioration of an electrode's performance curve with time. Ageing involved exposing the electrode to the conditions listed below:

a) The electrode was placed in an aqueous solution of 20% KOH , 1 molar in hydrazine, for one week at 25°C. No electric load was imposed during this time.

b) A more critical test involved operating the electrode at 50 ma/ cm^2 as a cathode, using the solution just mentioned as electrolyte, for a prolonged period. The performance curve was determined at suitable intervals.

Results were as follows:

1. For freshly prepared electrodes, the performance curves improved as follows: Platinum coatings were the poorest, iridium were better and rhodium was best.

2. Platinum coatings, which initially always show poor performance, undergo a relatively slow deterioration in the ageing tests just described.

3. Electrodes plated with a mixture of platinum, iridium and rhodium behaved as platinum plated electrodes.

4. Iridium coatings show relatively rapid deterioration with time.

5. The optimum rhodium plated electrodes (procedure described above) show little deterioration after one week of open circuit ageing (test "a" above). Initial results indicate fair performance in ageing tests of type "b".

6. It was found that all "aged" electrodes could be completely regenerated by immersion for five minutes in 98% sulfuric acid at 25°C. That is, the performance curve, after such regeneration, is identical with that of the newly plated electrode. Such regeneration can apparently be repeated a great number of times.

These electrodes are now being used as hydrazine electrodes in the assembled cell using flow electrodes.

1.4 The Thermocell

The thermocell is an electrochemical analogue to the solid - state thermoelectric generator; one difference being that conduction in one leg of the thermocell is by ionic rather than electronic migration. For example, a long column of molten silver chloride (m.p. 455°C), being a good conductor of electricity, can act as one leg of a thermocouple. If both ends of the column are capped with silver and the circuit completed by a wire (silver for example), a current is produced when the electrodes are at different temperatures. In the absence of convection within the melt, the thermodynamic analysis is similar to that of the solid - state devices. In practice, there is one important difference: since conduction in the melt is by silver ions, there is an accumulation of silver at one electrode. This must be recycled externally.

Fused - salt thermocells in general have a higher Seebeck coefficient than semi-conductors, however, the electrical conductivity is less, with the thermal conductivity probably of the same order of magnitude. The most significant difference between the two systems is the temperature of operation

with most salts melting in the range of 400 to 800 °C and having a liquidus range of 600 to 1000 °C. Thus, the fused - salt thermocell is interesting for conversion of heat to electrical energy in the high temperature range above that attainable by existing semi-conductor couples. Of course, in operation, it would be necessary to couple the thermocell in heat series with another type of device in order to extract energy from the heat expelled by the cell at the low temperature electrode.

Experimental work is being started to investigate the chlorine - chloride ion reversible electrode reaction in molten alkali chloride salts. Indications are that figures of merit of the magnitude of 10^{-3} are obtainable in these systems under certain conditions. The first phase of this study will be to investigate the effects of temperature and cation size on the Seebeck coefficient. In the second phase, such a cell will be operated under load to determine the effect of current density on the cell voltage with all other variables constant. Cell operating characteristics and the extent and causes of electrode polarization, will be explored. The apparatus is almost ready for trial operation.

1.5 Appendix II-A

Notes on Porous Gas Diffusion Type Electrodes

II TECHNICAL DISCUSSION

A. Electrode Performance

For electrochemical reactions to occur* at any electrode, the reactants must be allowed to come together at that part of the electrode surface which is submerged in electrolyte (see Appendix 1, 2). Electrons and ions respectively reach this surface by travel through the electrode and by migration through the electrolyte under action of the electromotive force developed in the cell. The uncharged reaction partners move to and from this surface by mass transfer through the electrolyte film at the electrode surface, with the usual concentration gradients acting as driving forces. Convection normally plays a part in bringing uncharged components from the body of the electrolyte to the film's outer boundaries.

The current densities attained at an electrode at any given voltage may be limited by the rates of adsorption or desorption of a reaction partner, by the kinetics of a surface reaction, or by mass transfer of an uncharged reaction partner. Mass transfer resistance is generally very important when dealing with reagents of low solubility, such as oxygen in aqueous electrolyte systems.

1. Experimental Procedure

Reaction rates attainable at silver and platinum wire screens functioning as oxygen and hydrogen electrodes have been explored under such conditions that oxygen mass transfer resistance was eliminated, (Appendix 2). The studies described here are for an 80 mesh platinum screen made of wire 0.002 inches in diameter, used as an oxygen electrode. General procedure involved causing a stream of electrolyte (20% aqueous KOH) containing dissolved molecular oxygen to flow through the test electrode, which was held at right angles to the electrolyte flow direction. Knowing the flow velocity, the concentration of dissolved oxygen and the oxygen reaction rate (calculated from the current density), then the concentration of oxygen at the electrode interface could be calculated from published mass transfer studies of shapes like those of the electrode under investigation. Operating conditions were such that depletion of the dissolved oxygen in the electrolyte flowing through the electrode was negligible, hence oxygen concentration at the electrode surfaces was reasonably uniform.

---

* Many of the ideas presented here are being incorporated into a paper now being prepared by H. P. Meissner and A. R. Reti.

2. Results

Results when operating with an aqueous solution of 20% KOH saturated with oxygen at two different partial pressures and flowing at two different velocities are presented in the curves of Figure 1. Four features of these results are worth noting. First, this electrode showed the typical polarization of oxygen electrodes under all conditions of operation, in that even when approaching open circuit operation, the observed voltage was at least 0.15 volts below theoretical. Second, at lower current densities, for the flow velocities and oxygen partial pressures studied, the experimental points all fall on a single Tafel line. Third, at higher current densities, the curves fall sharply away below this (extrapolated) Tafel line, depending on the flow velocities and oxygen concentrations employed. The significance of this region is discussed in Appendix 2. Fourth, the current densities attained on the smooth platinum wires used, expressed as milliamps per square cm of wire area (not face area), as shown in Figure 1, were not great. These current densities can be increased by increasing the catalytic effectiveness of the wire surface, as by coating with platinum black.

It is interesting to consider the significance of the common Tafel line region. It can be shown (Appendix 2) that under conditions of operation, the oxygen required to maintain these current densities is easily supplied by mass transfer. That is, the quantity of oxygen transferred, expressed as n gram mols per unit area per unit time, must be in accordance with the following familiar equation for steady state mass transfer:

$$n = k(c_0 - c_i)$$

Here c_0 and c_i are respectively the oxygen concentrations in the bulk electrolyte and at the wire - electrolyte interface, while k is the transfer coefficient. In the Tafel line region, k is large compared to n , hence the quantity $(c_0 - c_i)$ is very small. Since $(c_0 - c_i)$ is small, the concentration of oxygen at the surface of the electrode is substantially the same as in the bulk of the solution. In other words, mass transfer is not the rate - limiting step in this operation.

After the oxygen finds its way to the electrode surface, it is adsorbed. Adsorption rates are generally some function of the concentration of the material

II TECHNICAL DISCUSSION

A. Electrode Performance

For electrochemical reactions to occur* at any electrode, the reactants must be allowed to come together at that part of the electrode surface which is submerged in electrolyte (see Appendix 1, 2). Electrons and ions respectively reach this surface by travel through the electrode and by migration through the electrolyte under action of the electromotive force developed in the cell. The uncharged reaction partners move to and from this surface by mass transfer through the electrolyte film at the electrode surface, with the usual concentration gradients acting as driving forces. Convection normally plays a part in bringing uncharged components from the body of the electrolyte to the film's outer boundaries.

The current densities attained at an electrode at any given voltage may be limited by the rates of adsorption or desorption of a reaction partner, by the kinetics of a surface reaction, or by mass transfer of an uncharged reaction partner. Mass transfer resistance is generally very important when dealing with reagents of low solubility, such as oxygen in aqueous electrolyte systems.

1. Experimental Procedure

Reaction rates attainable at silver and platinum wire screens functioning as oxygen and hydrogen electrodes have been explored under such conditions that oxygen mass transfer resistance was eliminated, (Appendix 2). The studies described here are for an 80 mesh platinum screen made of wire 0.002 inches in diameter, used as an oxygen electrode. General procedure involved causing a stream of electrolyte (20% aqueous KOH) containing dissolved molecular oxygen to flow through the test electrode, which was held at right angles to the electrolyte flow direction. Knowing the flow velocity, the concentration of dissolved oxygen and the oxygen reaction rate (calculated from the current density), then the concentration of oxygen at the electrode interface could be calculated from published mass transfer studies of shapes like those of the electrode under investigation. Operating conditions were such that depletion of the dissolved oxygen in the electrolyte flowing through the electrode was negligible, hence oxygen concentration at the electrode surfaces was reasonably uniform.

---

* Many of the ideas presented here are being incorporated into a paper now being prepared by H. P. Meissner and A. R. Reti.

being adsorbed, and of the number of "vacant sites" available for occupancy by
the reagent being adsorbed. The fact that the location of the Tafel line was
unaffected by changes in oxygen concentration in the bulk solution, and hence
at the electrode surface, indicates that this surface was saturated with oxygen.
In other words, adsorption rates were not controlling.

It appears that a similar argument can be presented for the desorption and
mass transfer of products of the reaction. The hydroxyl ions move away from
the theater of reaction not by diffusion but by migration under the action of
the electromotive force acting in the cell. Initial tests indicate that change
in the concentration of OH⁻ ions in solution makes substantially no change in
the overall cell voltage, which suggests that neither desorption or mass transfer
of products away from the electrode surface determines the current density.

The foregoing indicates that a chemical reaction rate on the surface of the
catalyst must be rate controlling. This of course would account for the fact
that the current density developed is independent of the parameters that would
normally be important if mass transfer or adsorption rates controlled, namely
oxygen concentration, OH⁻ ion concentration, and electrolyte flow rates.

3. Porous Gas Diffusion Type Electrodes

Porous gas diffusion type electrodes contain a complex network of
inter-connecting pores of irregular cross-section and tortous path. As a first
approximation, these pores can be taken as cylindrical holes of constant
diameter S lying perpendicular to the electrode surface, as shown in Figure 2.
Oxygen travels into the mouth of the pore to the meniscus of the electrolyte
which fills most of the pore. The oxygen dissolves at this meniscus, and then
finds its way down through the pore by diffusion through the electrolyte.
Because of the electrochemical reaction occurring at the pore wall, it is
obvious that c , the oxygen concentration in the electrolyte, must decrease
as x , the distance into the pore from the meniscus, increases.

A system like this can be dealt with by a minor modification of the approach
used by Thiele (3) to calculate catalyst particles effectiveness. These
assumptions will be made:

1. The electrical potential along the entire pore wall is a constant.
This assumption appears reasonable in view of the relatively high conductivity

of the electrode material, and the small distances involved.

2. A critical distance x_o exists, measured from the meniscus through the electrolyte into the pore over which electrochemical reaction occurs, beyond which substantially no action occurs. Oxygen concentration falls from c_o (the concentration at the meniscus, which is assumed at saturation) to zero over this critical distance.

3. As a first approximation, the current density on the capillary walls over the critical distance x_o is assumed a constant, independent of oxygen concentration. That is, the pore wall is assumed to be coated with platinum having the same electrical characteristics as the screen electrode of Figure 1. Inspection of this figure shows that at a polarization of 0.3 volts, a roughly constant current density of about 0.1 ma/cm^2 can be maintained down to an oxygen concentration corresponding to 0.21 atm. It will be assumed that this same current density can be maintained on the pore walls at a polarization of 0.3 volts, down to an oxygen concentration of zero.

4. The radial gradient of oxygen concentration in the capillary pore is assumed small enough to be negligible. In other words, an oxygen concentration gradient exists only in the "x" direction in Figure 1. This assumption is clearly more justifiable as the pores become smaller.

4. Mathematical Model

The primary mass transfer resistance to oxygen movement in a pore, especially one in which the liquid meniscus lies reasonably close to the pore mouth, is in diffusion of dissolved oxygen through the liquid phase. Thus consider an idealized cylindrical pore such as is presented in Figure 2, filled with electrolyte. An imaginary plane a - a is passed through this capillary at a distance x from the meniscus, as shown. By the familiar diffusion equation, the oxygen crossing plane a - a from left to right is as follows:

$$n = - \frac{\pi \delta^2}{4} D \frac{dc}{dx} \tag{1}$$

where n is gram mols O_2 /(cm)^2(sec), D is the diffusivity of the dissolved oxygen in cm^2/sec., c is the concentration of oxygen in gram mols/cc., and δ is the pore diameter in cms.

After crossing plane a - a , the dissolved oxygen diffuses to the
capillary walls between x_o and -x , reacting all along these walls at a
constant rate equivalent to a current density i amps/cm^2. The mols
oxygen passing through plane a - a are obviously related to i as follows:

$$n = \pi \delta \, (x_o - x) \, \frac{i}{4 \, F} \qquad (2)$$

Equating the two foregoing equations, integrating and simplifying,

$$x_o/\delta = \sqrt{\frac{2 \, FDc_o}{\delta \, i}} \qquad (3)$$

It is interesting to consider the implications of equation (3) for oxygen
diffusing through an aqueous 20% KOH electrolyte located in a pore whose
walls have the same electrical characterisitcs as the platinum screen of
Figure 1. As discussed above, the current density on the pore walls, as a
first approximation, is assumed to be constant at 0.1 ma/cm^2. With this
current density, equation (3) can now be solved for various pore sizes and
oxygen partial pressures, with results presented in Table 1. Note that in
this calculation, D for O_2 is 1.8×10^{-5} cm^2/sec (4), the bulk concen-
tration c_o for an oxygen pressure of 1 atm. is 2.9×10^{-7} g mols/cc,
and the Faraday number F is of course 96,500 coulombs.

Several conclusions can be drawn from Table 1 at this point. The first
is that the reactive zone of a pore is extremely short for a gaseous reagent
of low solubility like oxygen, being of the order of a micron or so in length.
Second, an increase in reactivity (that is, in the current density which can
be attained at a pore wall) actually shortens the "active length" of a pore.

5. Electrode Current Densities

A simple idealized electrode can be viewed as comprising cylindrical
pores lying at right angles to the electrode face, and spaced a distance 2δ
apart on centers, as in Figure 3. The current generated per pore, namely I_p,
is readily calculated. That is,

$$I_p = \pi \delta \, x_o \, i \qquad (4)$$

Substituting equation (3) into equation (4):

$$I_p = \pi \delta \sqrt{2 \; FDc_o \; i \; \delta} \tag{5}$$

The total number of pores per unit face area is obviously $1/(4 \delta^2)$, and from equation (5), the value of I_{CD}, the current density on the electrode face area is:

$$I_{CD} = \frac{\pi}{4} \sqrt{\frac{2 \; FDc_o \; i}{\delta}} \tag{6}$$

The value of I_{CD} can now be calculated for an electrode with pores with electrical characteristics of Figure 2. For pore diameters of 10^{-6} cm, the value of I_{CD} is around 10 ma/sq cm. Such a current density, of course, is low, and could be increased in several ways:

a) Increase the number of pores by decreasing the diameter δ. However, this is not a very hopeful avenue of approach because 10^{-6} cm (or 100 Å) is not far from the size of the hydrated ions themselves.

b) Increase the value of i, namely the current density on the capillary walls, by improving catalytic effectiveness of the pore walls. Inspection of equation (6) shows that a large increase in i is necessary to gain much in I_{CD}, because of the square-root relation involved. That is, a 100 fold increase in i results in only a 10 fold increase in I_{CD}.

c) Develop new electrode geometry, whereby it is possible to install more micropores per unit face area of the electrode. Clearly it will not be possible to crowd more cylindrical pores onto the front face, as in Figure 3, since the spacing of 2δ on centers is already very close. An alternative is to consider new electrode geometry.

TABLE 1

Active Length of Catalyst Pores

p_{O_2}	O_2 solubility g mols/cc	δ cms	x_o/δ	x_o, cms (Eq. 3)
1 atm.	2.9×10^{-7}	10^{-6}	100	10^{-4}
1 atm.	2.9×10^{-7}	10^{-5}	32	3×10^{-4}
1 atm.	2.9×10^{-7}	10^{-4}	10	10^{-3}
0.21 atm.	0.6×10^{-7}	10^{-4}	4	4×10^{-4}

6. New Electrode Designs

To increase current densities, it is necessary merely to increase the total pore area lying within x_o of the meniscus. This can be done in several ways, of which two are mentioned here:

a) Substitute macropores (diameter γ) for the micropore of Figure 3, each macropore having micropores radiating from its walls, as in Figure 4. The macropores in this case could lie $2(x_o + \gamma)$ cms apart. The macropores would of course not contain electrolyte, whereas the micropores would be filled with electrolyte as in Figure 3. These micropores would necessarily be cross-connected, and communicate with the bulk electrolyte phase.

b) Have a "corrugated" electrode face, as in Figure 5, again perforated with cylindrical micropores lying at right angles to the face. The thickness of the electrode sheet is now not much more than x_o, whose magnitude in turn depends on δ, the diameter of the micropores. Because of the corrugations, far many more micropores exist per unit face area than in the simple electrode of Figure 3.

Obviously many problems remain to be solved in constructing any of these electrodes, ranging from the assembly task through to interface control problems. It is significant, however, that by the proper geometry, a very large multiplying factor can in theory by obtained over a simple electrode system like Figure 3.

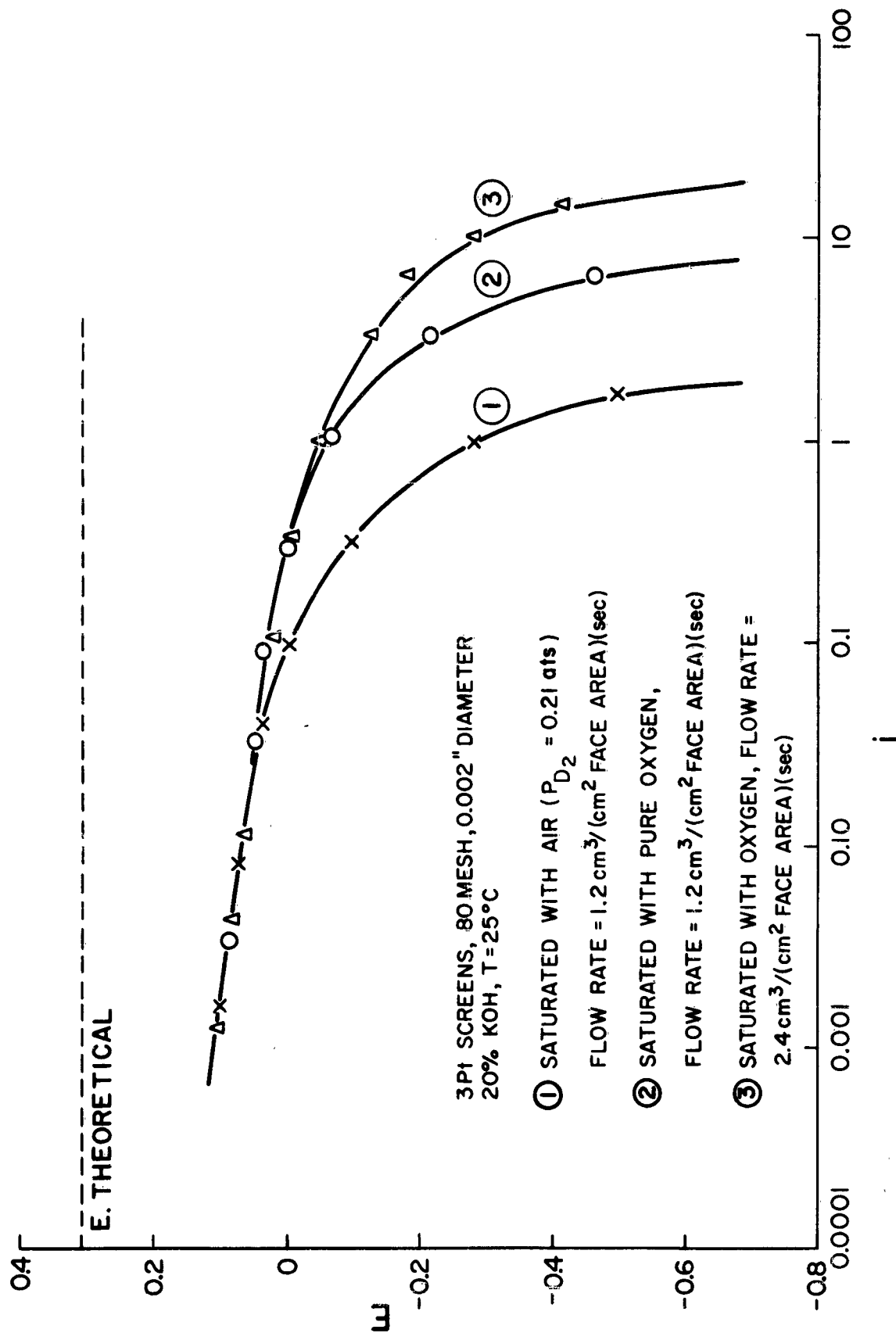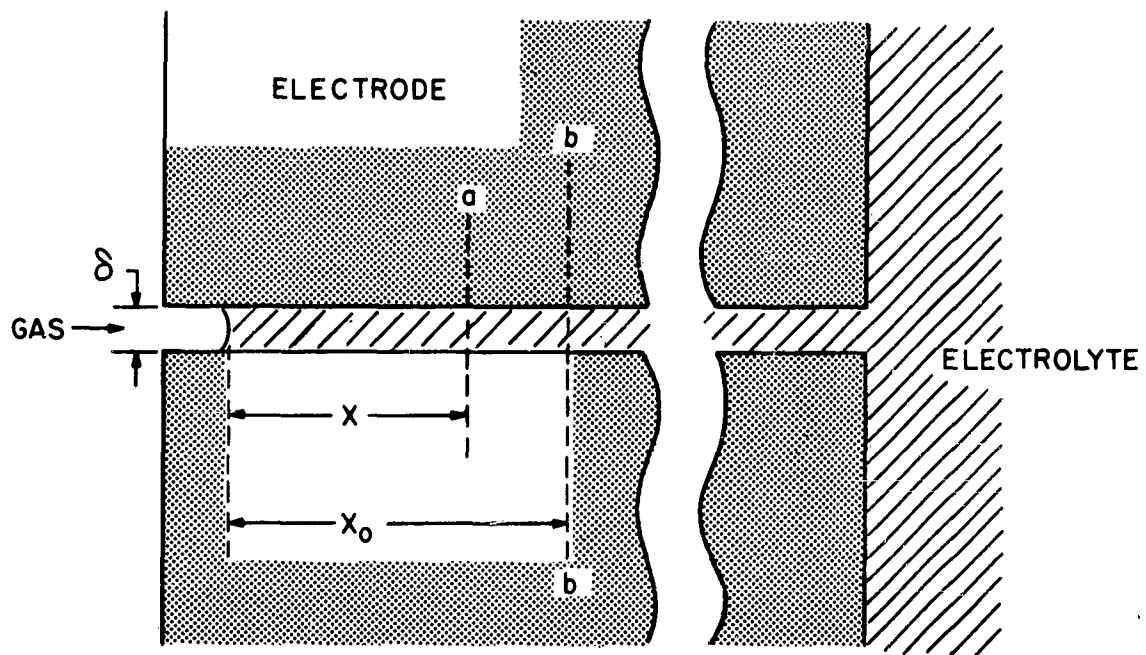Figure 1   Performance Curves of a Platinum Screen Flow Electrode

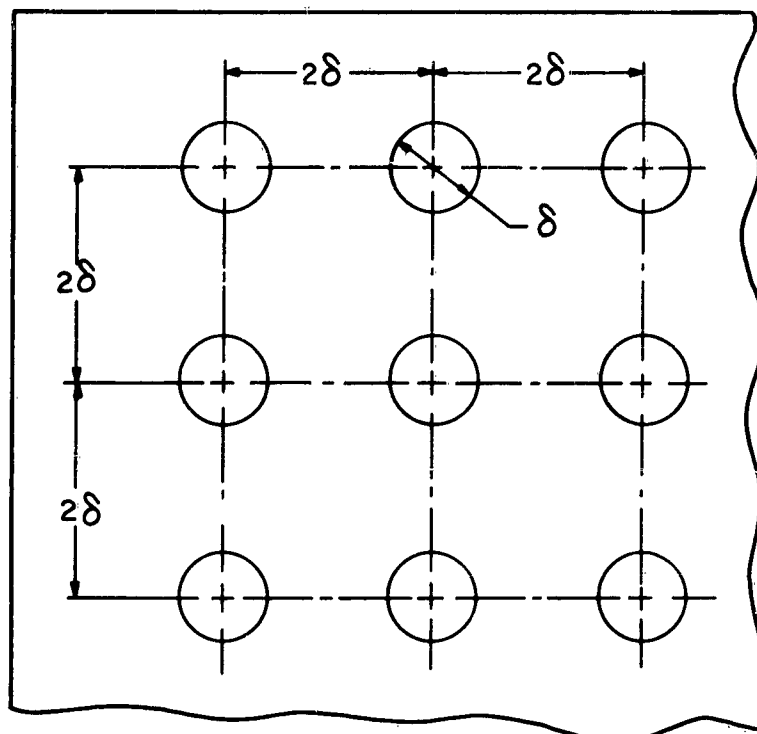Figure 2   Idealized Cylindrical Pore of Diameter

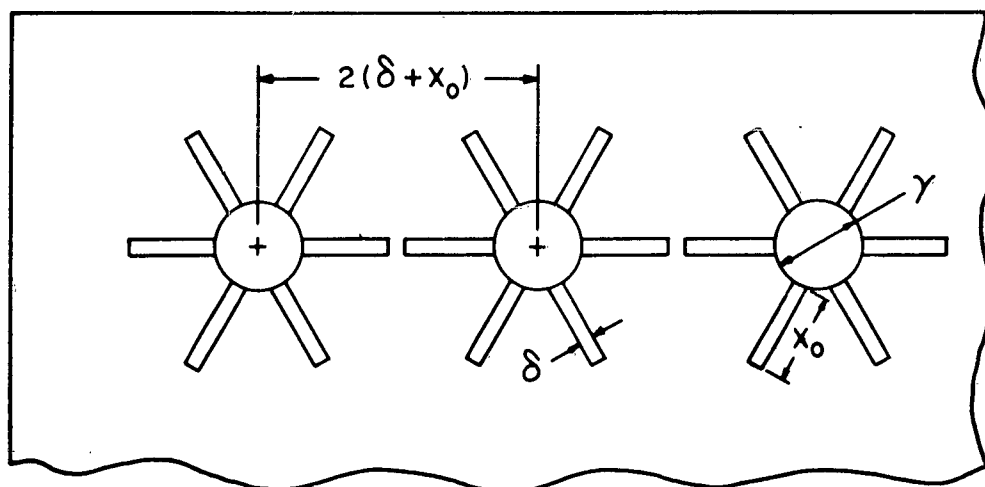Figure 3   Pore Location on Electrode Face

Figure 4   A Micro-Micro Pore System. The Micropores are Assumed
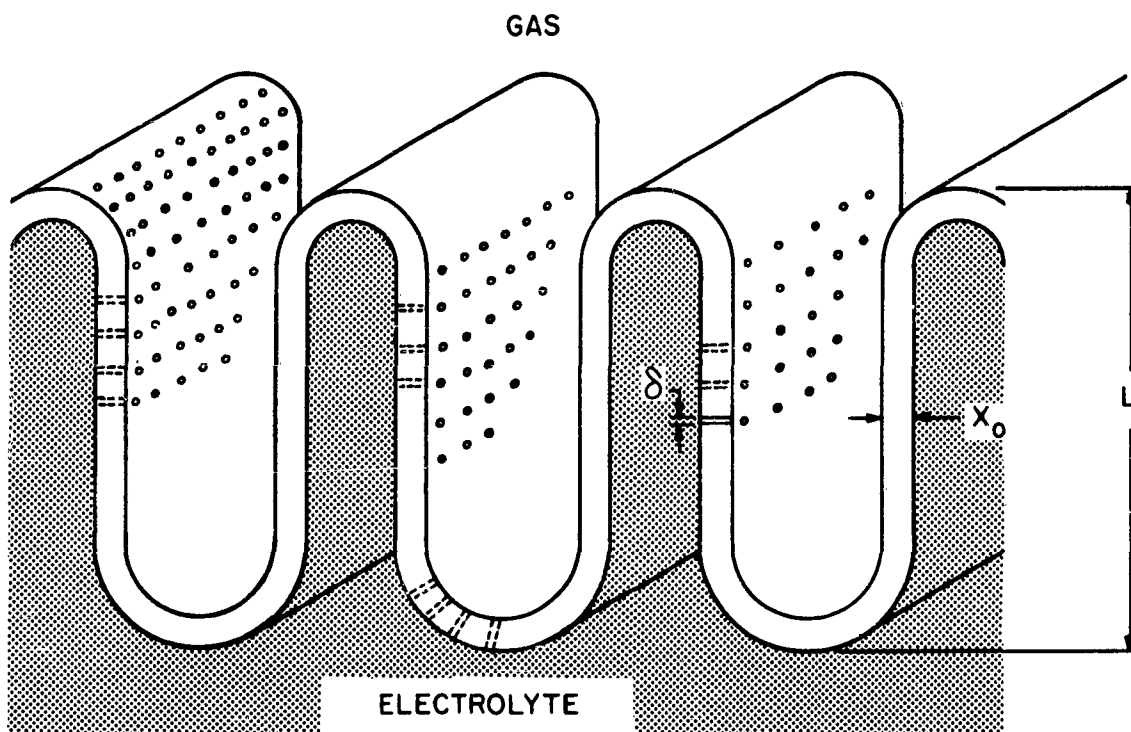to be Interconnected

GAS

Figure 5   A Corrugated Electrode Sheet Perforated with Micropores

1.6 Appendix II-B

Preprint: "Electroreduction of Oxygen and Silver
on Platinum Electrodes."

THE ELECTROREDUCTION OF OXYGEN ON SILVER AND PLATINUM ELECTRODES [*]

by

H. P. Meissner

A. R. Reti

Department of Chemical Engineering and Research Laboratory of Electronics
Massachusetts Institute of Technology
Cambridge, Massachusetts

Oxygen electroreduction was investigated under known and controlled conditions of oxygen mass transfer on electrodes made of smooth platinum and silver wires woven into screens. The object was to obtain insight into electrode performance at higher current densities when operating so that mass transfer effects were eliminated.

Apparatus

The apparatus, shown in Figure 1, consists of a system for saturating the electrolyte with oxygen under a chosen pressure, a cell containing both a dummy electrode and a wire screen electrode through which the saturated electrolyte is caused to flow, and associated equipment. The saturator, the cell and all tubing are made of polyvinyl chloride and Teflon. Each test electrode studied consists of three metal screen discs, 2 cms in diameter, placed one against the other, and held at right angles to the direction of electrolyte flow by suitable gaskets. The test electrode T is connected to a reference calomel electrode C through a Luggin capillary and a salt bridge, and the potential difference between these two electrodes is measured at P, which is either a Sargent Model MR D.C. Recorder or a Tektronic Model 502 Dual Beam Oscilloscope.

In a run, electrolyte is first introduced into the saturator S through line E. Oxygen or air from G flows through the fritted glass

plug at the bottom of the vessel, and is bubbled up through the liquid
until the electrolyte is saturated. This electrolyte, which is
driven out of the chamber by gas introduced above the liquid surface,
passes through the control valve V, the flow meter F, the test electrode
T, and the cell overflow O. This system makes possible the flow of
electrolyte saturated with oxygen at a desired partial pressure through
the electrode at a controlled and known velocity. During operations,
current is passed through the test electrode by means of the DC power
supply B, decade resistance R (1 to 10^6 ohms) and the dummy electrode
D. The magnitude of this current is measured by ammeter A.

Both platinum and silver screens were studied as electrodes. The
platinum screens were 80 mesh, woven of smooth wire 0.002 inches in
diameter, and having a ratio of wire geometrical surface area to face
area of 1 per screen. The silver screens used were 180 mesh made of
wire 0.0023 inches in diameter, and having a ratio of geometrical to
face area of 2.6 per screen. Since the geometrical screen area is known,
the reaction rate per unit area is readily calculated. Moreover, the
screen geometry is simple enough to make possible reasonably accurate
.calculations of the coefficients of mass transfer of oxygen from the
bulk electrolyte flowing through the screens to the electrode surface.
Such pure metal screens are also excellent conductors, and keep the whole
electrode surface at a constant potential, simplifying interpretation of
results.

The variables studied were oxygen concentration, electrolyte composition
and pH, and electrolyte flow rates. Oxygen concentrations were those
obtained by saturating the electrolyte used with either oxygen or air
at one atmosphere and 25°C. Various electrolytes were used, with pH
ranging from 0.55 to 14.85. Flow rates varied from 1.2 to 3.6 cc of
electrolyte per second per square centimeter of electrode face area.
These flow rates and oxygen concentrations were such that generally not
more than 10% of the dissolved oxygen was consumed, thus giving a relatively
constant oxygen concentration driving force through the electrolyte. All

runs were at 25°C.

Results

Curves of E, the electrode voltage on the standard hydrogen scale, versus i, the current density, for operations in 20% KOH solutions using either platinum or silver test electrodes, are presented in Figures 2 and 3 respectively. The curves differ in flow rates and oxygen concentration. Inspection shows that results are quite similar for the two different metal electrode systems. Each curve is characterized by a straight line section at lower current densities, followed by a second section at higher current densities where the curve falls away more and more sharply below an extrapolation of the straight line section. For purposes of this discussion, these two sections will be referred to as regions I and II. The straight line of region I agrees with the familiar Tafel equation:

$$E_S - E_{Actual} = \eta = a + b \log i \qquad (1)$$

Here E_S is the reversible electrode potential calculated for the oxygen concentration in the electrolyte existing at the electrode surface, E_{Act} is the actual voltage observed, i is the current density in amperes per square centimeter and a and b are constants.

Inspection of Figures 2 and 3 shows further that for a given electrode, all experimental points in region I fall on the same straight line, independent of oxygen concentration and flow velocity. The point dividing regions I and II on the curve for any run cannot be located exactly, but appears to move to higher current densities as the oxygen concentration or electrolyte flow velocity is increased. Unlike region I, region II is strongly influenced by oxygen concentration and flow velocity. Region II for each curve extends over a considerable range of current density, and terminates by becoming nearly vertical at some limiting current density, whose magnitude increases with increasing oxygen

concentration or flow velocity.

The effect of pH on the electroreduction of oxygen was explored in
both acid and basic media with platinum, with results as in Figure 4.
Electrode voltages are again reported on the standard hydrogen scale.
Runs on silver, which is attacked by acid, were confined to alkaline
electrolytes, with results similar to those for platinum in this pH
range. Inspection of Figure 4 shows that the curves have the same
general shape as in Figure 2, and that the slope of the Tafel line region
does not appear to change much with pH. For the electrolyte systems
studied, the electrode overpotential at any given current density
increases when the pH is lowered, as is clear from Figure 5, on which
the data of Figure 4 are replotted. Inspection shows that the performance
of this platinum electrode deteriorates rapidly at values of pH above 9.

It should be noted that the current densities in Figures 2, 3 and 4
are per unit of geometrical area. Since three screens were always used,
the current density per unit face area are obtained by multiplying the
abscissa by 3 in the case of the platinum screens, and 7.8 for the silver
screens. These current densities can of course be further increased
by using more screens.

Tafel Region

In the derivation of the Tafel equation 1, it is assumed that the
rate controlling step is an electrochemical reaction ($\underline{8}$). Therefore, the
fact that the experimental data reported in Figures 2 and 3 form a
straight line in region I indicates that an electrochemical reaction rate,
rather than mass transfer, controls. The finding that the experimental
points fall on the same straight line, independent of the oxygen partial
pressure, will be discussed later.

Limiting Current Densities

The current density i is related to N, the mols oxygen reaching a
square centimeter of electrode surface per second, as follows:

$$N = \frac{i}{4 \times 96,500} \tag{2}$$

This oxygen reaches the electrode surface by diffusion through the stagnant layer covering the electrode surface. The magnitude of N is related to the oxygen concentration in the bulk of the electrolyte flowing and in the electrolyte at the electrode surface, namely C_B and C_S, by the familiar mass transfer equation ($\underline{10}$):

$$N = K(C_B - C_S) \tag{3}$$

where K, the mass transfer coefficient, is a function of the liquid velocity. Equation (2) indicates that an increase in i brings about an increase in N. When operating at constant electrolyte velocity, this in turn causes a decrease in C_S by equation (3). Obviously the maximum or limiting current density i_L attainable at any given values of electrolyte flow velocity and oxygen concentration C_B is reached when C_S becomes zero, and can be calculated by combining equations (2) and (3) as follows:

$$i_L = 4 \times 96,500 \; K C_B \tag{4}$$

No study has as yet been published of the magnitude and behavior of mass transfer coefficients between liquids and screens such as were used as test electrodes in the work described here. However, performance data and correlations are available for flow normal to cylinders of small diameters, and these results should be applicable to screens, at least as a first approximation. Thus it is shown by McAdams ($\underline{7}$) , figure 10.12, that at low Reynolds numbers, the coefficient of heat transfer for flow normal to cylinders varies with the velocity raised to approximately the 0.4 power. By the Reynolds analogy ($\underline{10}$), the mass transfer coefficient K of equation (3) must behave similarly, hence equation (4) can be rewritten:

$$i_L = \alpha \, v^{0.4} \, C_B \tag{5}$$

Thus the finding that the limiting current for curve 2 of Figure 2 is about 5 times that of curve 1 reflects the fact that C_B is about 5 times as great for curve 2, since pure oxygen instead of air was used here to saturate the electrolyte. The limiting current for curve 3 is somewhat less than twice that of curve 2, more or less in agreement with the effect of doubling the velocity predicted by equation 5. The relations between the limiting currents of the curves of Figure 3 can be explained similarly.

It is further of interest that the limiting current density can be calculated from equation (4), with results showing fair agreement with the observed values of i_L, as illustrated below for curve 2 of Figure 3. The silver screen used in this run (180 mesh, with D, the wire diameter of 0.0023" or 0.0058 cm) has a free flow area of (1 - 2 x 180 x 0.0023) = 0.174 square inches per square inch of face area. The superficial electrolyte flow velocity is 1.2 cm/sec, or an average velocity, V, of (1.2 + 1.2 x 0.174)/2 = 4.05 cms/sec. For 20% KOH at 25°C, the viscosity μ is 10 lbs/(hr)(ft), C_p is 0.85 Btu/lb°F, the thermal conductivity k is 0.35 Btu/hr ft^2 °F/ft, the density ρ is 70 lbs/cu ft, and the diffusivity D_L of oxygen in this system is 1.79 x 10^{-5} cm^2/sec, or 7 x 10^{-5} ft^2/hr. Using consistent units, the Reynolds number $DV\rho/\mu$ is then 0.64; the Prandl number $C_p\mu/k$ is 2.4 and the Schmidt number $\mu/\rho D_L$ is 2050.

From McAdams (7), Figure 10.12, $(hD/k)(C_p\mu/k)^{-0.3} = 0.7$

Therefore, the Nusselt number $(hD/k) = 1.82$

By the Heat – Mass Transfer analogy (10), the Sherwood number is:

$$\frac{KD}{D_L} = \frac{hD}{k} \left[\frac{\mu/\rho D_L}{C_p\mu/k} \right]^{1/3} = 10.3$$

and so K is 0.031 cm/sec.

The solubility of pure O_2 at 1 atm pressure at 25°C in 20% KOH

is 2.9×10^{-7} g mols/cc, hence the limiting current can be calculated from equation (4) as follows:

$$i_L = 0.0031 \ (2.9 \times 10^{-7}) \times 4 \times 96{,}500 = 3.5 \times 10^{-3} \ \text{amps/cm}^{-2}$$

Inspection shows this value to be in reasonable agreement with the extrapolated value of the limiting current for curve 2 of Figure 3. Values of i_L cannot always be calculated this successfully, as is evident from the table below:

Fig. No.	Curve	Calculated i_L	Observed i_L
2	1	4.2×10^{-4}	1.5×10^{-3}
	2	2.0×10^{-4}	6×10^{-3}
3	1	7.4×10^{-4}	6×10^{-4}
	2	3.5×10^{-3}	4×10^{-3}

Agreement is nevertheless not bad, recognizing that both the diffusivity and solubility of oxygen in 20% KOH are not known very accurately, and recognizing the approximations made in the mass transfer calculations (assuming a screen system is equivalent to flow normal to cylinders of screen wire diameter). The results just presented therefore support the explanation that the final drop - off in the curves of Figures 2 and 3 is due to oxygen concentration polarization.

Concentration Polarization

At very low current densities, it is evident from equation (3) that C_B and C_S are substantially equal. At higher current densities as N increases, C_S must become noticeably smaller than C_B. Under all these conditions, the theoretical electrode voltages E_B and E_S as calculated for oxygen concentrations in the bulk of the electrolyte and at the electrode surface respectively, differ as follows:

$$E_B - E_S = - 0.059 \log \frac{C_B}{C_S} \tag{6}$$

By adding equation (6) to equation (1), the Tafel equation is revised to include the effects of concentration polarization:

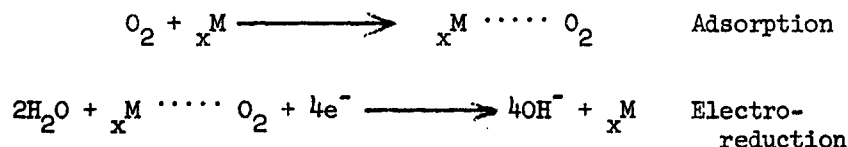$$E_B - E_{Actual} = a + b \ln i - 0.059 \log \frac{C_B}{C_S} \qquad (7)$$

But by combining equations (2), (3) and (4), C_B/C_S is found to equal $i_L/(i_L - i)$, hence equation (7) becomes:

$$E_B - E_{Actual} = a + b \ln i - 0.059 \log \frac{i_L}{i_L - i} \qquad (8)$$

The values of a and b for region I of the curves of Figure 2 are respectively - 0.01 and - 0.4. The value of i_L for curve 2 of Figure 3 is about 4 ma/sq cm. Using these values for a, b and i_L, equation (8) has been plotted in Figure 6, and the experimental points of curve 2 of Figure 3 have been presented on the same plot. Inspection shows that in region II, the curve so calculated from equation (8) does not coincide with the experimental points. Similar lack of agreement exists between equation (8) and the experimental points of the other runs shown on Figures 2 and 3. These discrepancies can be reconciled in terms of the adsorption hypothesis presented below.

Adsorption Hypothesis

The oxygen electroreduction studies of Lingane (6) and Sawyer and Interrante (9) suggested that prior to the electroreduction step, oxygen reacts with the metal electrode to form either a surface oxide or hydroxide, like PtO, PtO_2, or $Pt(OH)_2$. This same evidence could be interpreted as indicating that oxygen is chemisorbed on the metal electrode surface. Such a chemisorption step would then be followed by electroreduction, as follows:

$$O_2 + {}_xM \longrightarrow {}_xM \cdots O_2 \qquad \text{Adsorption}$$

$$2H_2O + {}_xM \cdots O_2 + 4e^- \longrightarrow 4OH^- + {}_xM \qquad \text{Electro-reduction}$$

It is now assumed that the rate of oxygen chemisorption on the electrode surface can be described by the Becker - Zeldovich equation (1), (11), which has been found to apply to the chemisorptions of oxygen on silver (9) and the adsorption of oxygen on Tungsten (5):

$$\text{Adsorption Rate} = B \frac{d\Theta}{dt} = AC_S (1 - \Theta)e^{-b\Theta}$$

where Θ is fractional coverage of the surface active sites by the chemisorbed oxygen, t is time, A and b are constants, and B is the maximum mols which can be adsorbed on a unit area. Thus the adsorption rate $B \frac{d\Theta}{dt}$ is expressed in gram mols per unit area per second. At steady state, the rate of oxygen chemisorption is equal to the rate of adsorbed oxygen electroreduction (assuming that the chemisorption is essentially irreversible, that is, that the desorption rate is negligible). It follows that:

$$\frac{i}{4 \times 96,500} = A \, C_S(1 - \Theta) \, e^{-b\Theta} \tag{9}$$

By this equation, adsorption rates are rapid enough at low current densities so that Θ lies very close to unity, but as current densities increase, a point is soon reached at which Θ is noticeably smaller than unity. Further increases in i then cause further decreases in Θ. Under all conditions, a given current density i and a given oxygen concentration at the surface C_S obviously characterize a surface coverage Θ.

Since the electrochemical reaction can presumably take place only at the areas covered by chemisorbed oxygen, it appears more appropriate to use an "effective" current density based on "effective" or covered area instead of the current density based on total electrode area, whenever considering the electrochemical kinetics. The "effective" current density can be simply described by the relation

$$i_{eff} = \frac{i_s}{\Theta} \tag{10}$$

At a given bulk electrolyte oxygen concentration, as the current density increases, the oxygen chemisorption rate is not fast enough to keep the electrode surface completely covered, and so the coverage Θ becomes smaller than unity. The "effective" current density thus becomes larger than the current density based on total surface area, with the consequent increase in the electrode overvoltage. A plot of voltage versus i_s, rather than versus i_{eff}, will therefore cause the kind of curvature observed in region II of the curves of Figures 2, 3, and 4.

The low chemisorbed oxygen coverage at current densities close to the limiting current density has an additional effect on the electrode overvoltage, since the activation energy of adsorption is not independent of the coverage Θ. Higuchi, Eyring and Ree (5) showed that the activation heats of adsorption and desorption generally decrease with increasing Θ, and explained this as being due to the effect of the field of the adsorbed layer on the adsorbing (desorbing) atom or molecule. Other investigators explain this phenomenon by postulating that some sites on the surface have higher activity than others. Whatever is the real explanation in this case, it would be expected that as the coverage decreases, only the more strongly bonded chemisorbed oxygen will be left, requiring a higher than normal activation energy (overvoltage) for the electroreduction step.

Based on the adsorption hypothesis proposed here, therefore, the pronounced curvature observed in region II of the curves of Figures 2, 3, and 4 can be attributed to the simultaneous influence of two factors. The first is that the effective current density is greater than the current density based on the entire surface area, with consequent apparent increase in the electrode overvoltage. The second is that as the fractional surface coverage is decreased, the activation energy and hence the voltage needed to remove a further increment of adsorbed oxygen increases.

The finding that the dividing points between regions I and II of the curves of Figures 2 and 3 moves to the right with increasing flow velocities and oxygen concentrations is of course consistent with this hypothesis. That is, higher flow velocities and higher values of C_B cause C_S to increase, resulting in values for Θ close to unity at higher current densities than before. As long as Θ is approximately unity, deviations from the Tafel line will not occur.

Double Layer Capacitance

The proposed explanations of the electrode behavior appear consistent with the experimental evidence. It seemed desirable, however, to find some further experimental support for the proposed explanation. Unfortunately, it is not easy to ascertain the presence and amount of chemisorbed species on an electrode surface in the presence of electrolyte. Studies of the electrode surface by infrared spectroscopy are as yet, not feasible, since the large amounts of electrolyte in the beam path would drown out the signal resulting from a chemisorbed monolayer. However, some information on the state of the electrode surface can be obtained by measurement of the electrode double layer capacitance, which should be influenced by the presence of a layer of chemisorbed oxygen. That is, the fractional coverage Θ of the surface by chemisorbed oxygen remains substantially constant and equal to unity in region I, but grows smaller as region II is penetrated further. It would therefore be expected that the electrical double layer capacitance would remain constant in region I, but change in region II. Electrical double layer capacitance measurements were therefore performed by the methods used by Hackerman (3), (4). The results are presented in Figure 7, where the observed electrical double layer capacitance is plotted as a function of current density at a constant electrolyte velocity, for electrolyte saturated with oxygen at one atmosphere in one case and with air ($pO_2 = 0.21$ Atm.), in the other. These results show that the electrical double layer capacitance does in fact begin to change noticeably at the dividing point between

regions I and II for these voltage - current density curves.
Moreover, the electrode double layer capacitance (coverage) is not
a function of current density alone, but of both current density and
oxygen concentration at the electrode surface, as it would be expected
from equations (1), (4) and (5). These measurements therefore tend
to confirm the proposed explanation.

The fact that the electrode potential in Figures 2 and 3 at low
current densities appears to be independent of oxygen concentration
(partial pressure) can now also be explained. It is to be expected
that the oxygen electrode potential for electrolytes saturated with
oxygen and with air at one atmosphere total pressure to differ by
$0.059 \log 1/0.21 = 0.042$ volts. Differences of such magnitude are
not observed in Figures 2 and 3, in spite of the fact that the recorder
sensitivity is of the order of 0.002 volts. This is presumably
because the electrode surface is saturated ($\theta = 1.0$) at both oxygen
partial pressures at low current densities, and the activation energy
required to reduce the chemisorbed oxygen from the electrode is the
same for both cases, making the electrode overpotential the same as
well.

Effect of pH

Inspection shows that the curves of Figure 5, for various values
of pH, again show straight Tafel line behavior in region I, followed
by increasing deviations from a straight line in region II. The curves
of Figure 5 do not drop almost vertically at higher current densities,
however, and so do not show a limiting current density such as was
encountered in 20% KOH.

The existence of a Tafel line region signifies that electro-
chemical kinetics control here. Region II can be explained in terms
of the adsorption hypothesis just presented. Moreover, it is a well
known fact (2) that sulfate ions tend to adsorb strongly on platinum
electrodes in acid solution. These adsorbed sulfate ions presumably

block off sites which would otherwise serve to catalyze the oxygen electroreduction reaction. Overvoltages over the entire pH range are higher in consequence.

The nonexistence of a limiting current density at these lower pH values, resulting from oxygen concentration polarization at the surface, is attributable to the fact that hydrogen ion reduction has presumably developed due to the high overpotentials existing. Therefore, at higher current densities, the electrochemical action is not solely the reduction of oxygen, but also of hydrogen ion.

Conclusions

The experimental method employed in these studies (flowing a reactant - saturated electrolyte through an electrode of known geometry) is particularly suited to the study of electrode potential as a function of current density and reactant concentration. Reproduceable data are obtained which can be related directly to current density per unit of superficial area, and mass transfer limitations can to a degree be reduced when they occur by increasing flow velocities and reactant concentrations. Thus the Tafel line region in oxygen electroreduction can be extended to higher current densities by increased electrolyte flow rates and oxygen concentrations. However, large overpotentials are encountered at both silver and platinum electrodes as the limiting current density is approached, in considerable excess of those to be expected from an extrapolation of the Tafel line, well before any such behavior attributable to mass transfer limitations is to be expected. These high overpotentials appear attributable to a rate - limiting chemisorption step.

Literature Citations

1. Becker, J., Trans. Am. Electrochem. Soc. *55*, 153, (1929)

2. Bockris, J. O'M. and Huq, S., Proc. Roy. Soc. (London) A237, 277 (1956)

3. Hackerman, N. and Brodd, R., J. Electrochem. Soc., *104*, 704 (1957)

4. Hackerman, N., McMullen, J., J. Electrochem. Soc., *106*, 341 (1959)

5. Higuchi, I., et al., J. Am. Chem. Soc., *77*, 4969 (1955)

6. Lingane, R., J. Electroanal. Chem., *2*, 296 - 309 (1961)

7. McAdams, W. H., "Heat Transmission", McGraw-Hill Book Co., 3rd Ed. (1954)

8. Potter, E. C., Electrochemistry., MacMillan Co., N.Y., (1956)

9. Sawyer, D., Interrante, L., J. Electroanal. Chem., *2*, 310 - 327 (1961)

10. Sherwood, T. K. and Pigford, R. L., "Adsorption and Extraction", McGraw-Hill Book Co., (1952)

11. Zeldovich, Ya, Acta Physicochim, U.S.S.R., *1*, 449 (1934)

Figure 1   Schematic Diagram of Appratus

Figure 2   Performance of Triple Screen Platinum Electrode in 20% KOH

Curve 1 represents electrolyte saturated with air at 25°C, flowing at 1.2 cc per sq. cm. of face area per second; Curve 2 represents electrolyte saturated with oxygen at 1 atm., flowing at 1.2 cc per sq. cm. of face area per second; and curve 3 is for electrolyte saturated with oxygen flowing at 2.4 cc per sq cm of face area per second. E is in volts on the standard hydrogen scale, i is in milliamperes per sq. cm. of geometrical screen area.

Figure 3   Performance of Triple Screen Silver Electrode in 20% KOH

Curve 1 is for electrolyte saturated with air, the other curves are for electrolyte saturated with O_2. Electrolyte flow rates for curves 1 and 2 are 1.2 cc per sq. cm. of face area per second, and for curves 3 and 4 are 2.4 and 3.6 cc per sq. cm. per second. E is in volts (standard hydrogen scale), i is in ma per sq. cm. of geometrical screen area.

Figure 4   Performance of Triple Screen Platinum Electrodes at Various pH Values

Curve 1 is for 1.7 m $KHCO_3$, 10.0 pH; Curve 2 is for 1 m K_2SO_4, 8.25 pH; Curve 3 is for 1 m K_2SO_4 plus 0.1 m H_2SO_4; 0.55 pH. Flow velocity was 1.2 cc per sq. cm. of face area, and the electrolyte in each case was saturated with oxygen at 1 atm. and 25°C. The theoretical voltages for curves 1, 2, 3, and 4 are respectively 0.635; 0.741; 1.120; and 1.196 on the standard hydrogen scale, i is in ma per sq. cm. of screen area.

Figure 5   Overvoltages at Triple Screen Platinum Electrodes versus pH.

The data of Figure 4 and of curve 2 of Figure 2 are replotted here for various current densities. Curves 1, 2, 3 and 4 are respectively for current densities of 0.0033, 0.010, 0.10 and 1.0 ma per sq. cm.

Figure 6   Effect of Current Density on Actual and on Calculated
                           Potential (Equation 8) for Platinum Screen Electrodes

                               Curve 2 is the same as curve 2 of Figure 3, while
curve a is calculated from equation 8 for these same
conditions.

Figure 7   Electrode Potential E and Double Layer Capacitance C
                           vs Current Densities of Triple Platinum Screen Electrodes

                               E is volts on the standard hydrogen scale, C
is in microfarads per sq. cm. of screen surface area,
and i is in ma/sq. cm. of geometrical screen area.
The electrolyte was 20% KOH, saturated at 25°C and 1
atm. with air for curves (1), and with oxygen for
curves (2).

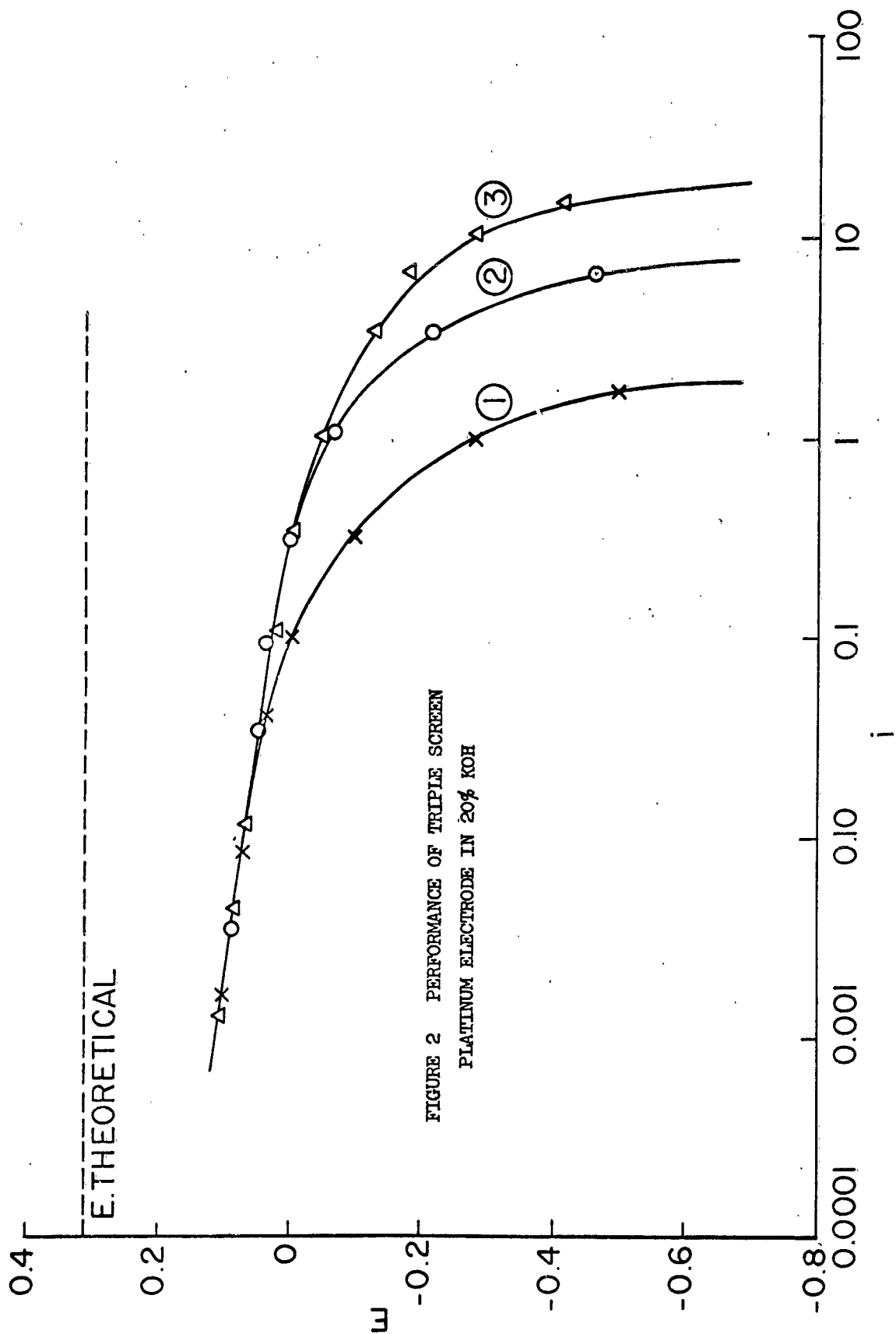FIGURE 1   SCHEMATIC DIAGRAM OF APPARATUS

E. THEORETICAL
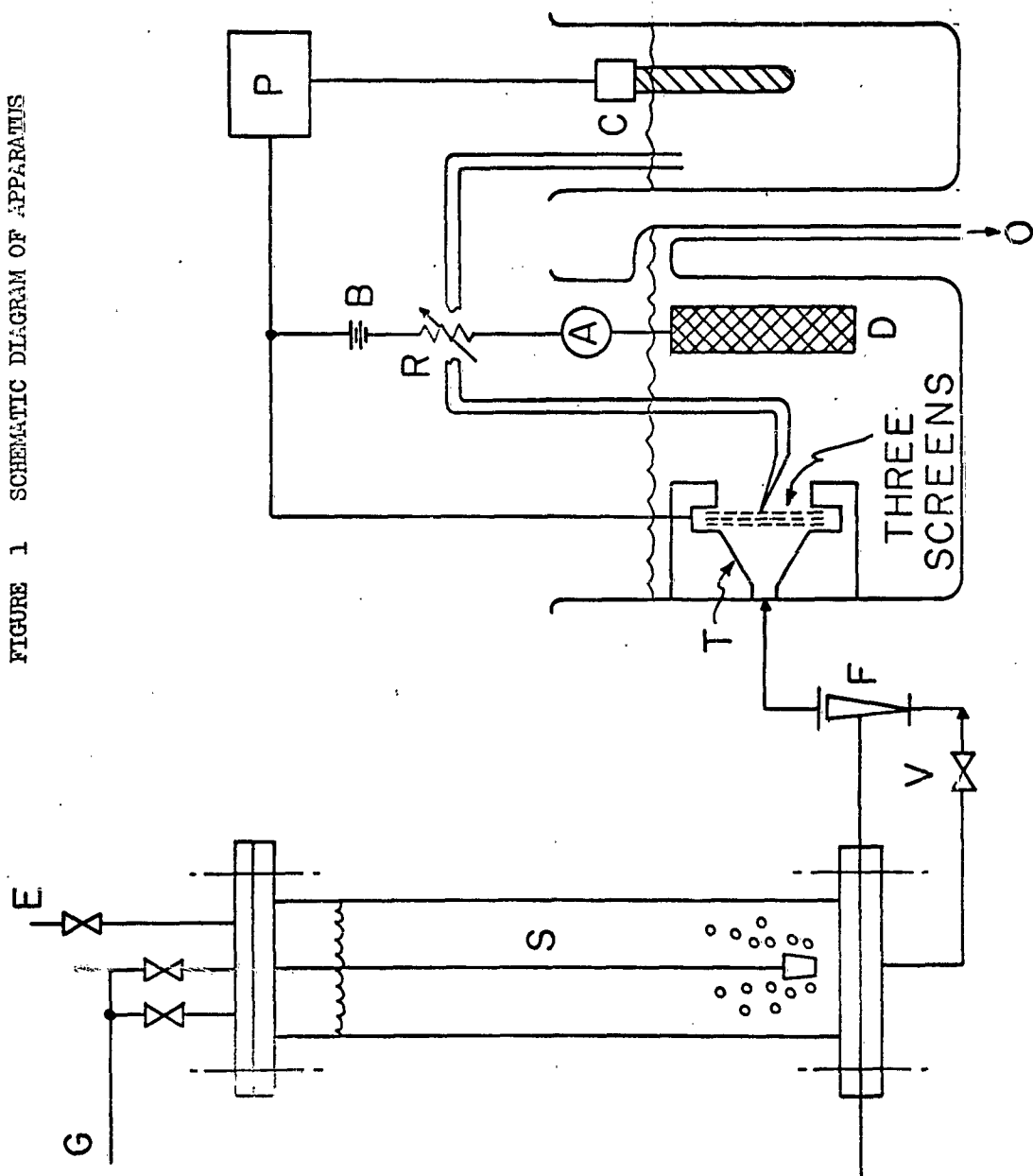
FIGURE 2   PERFORMANCE OF TRIPLE SCREEN
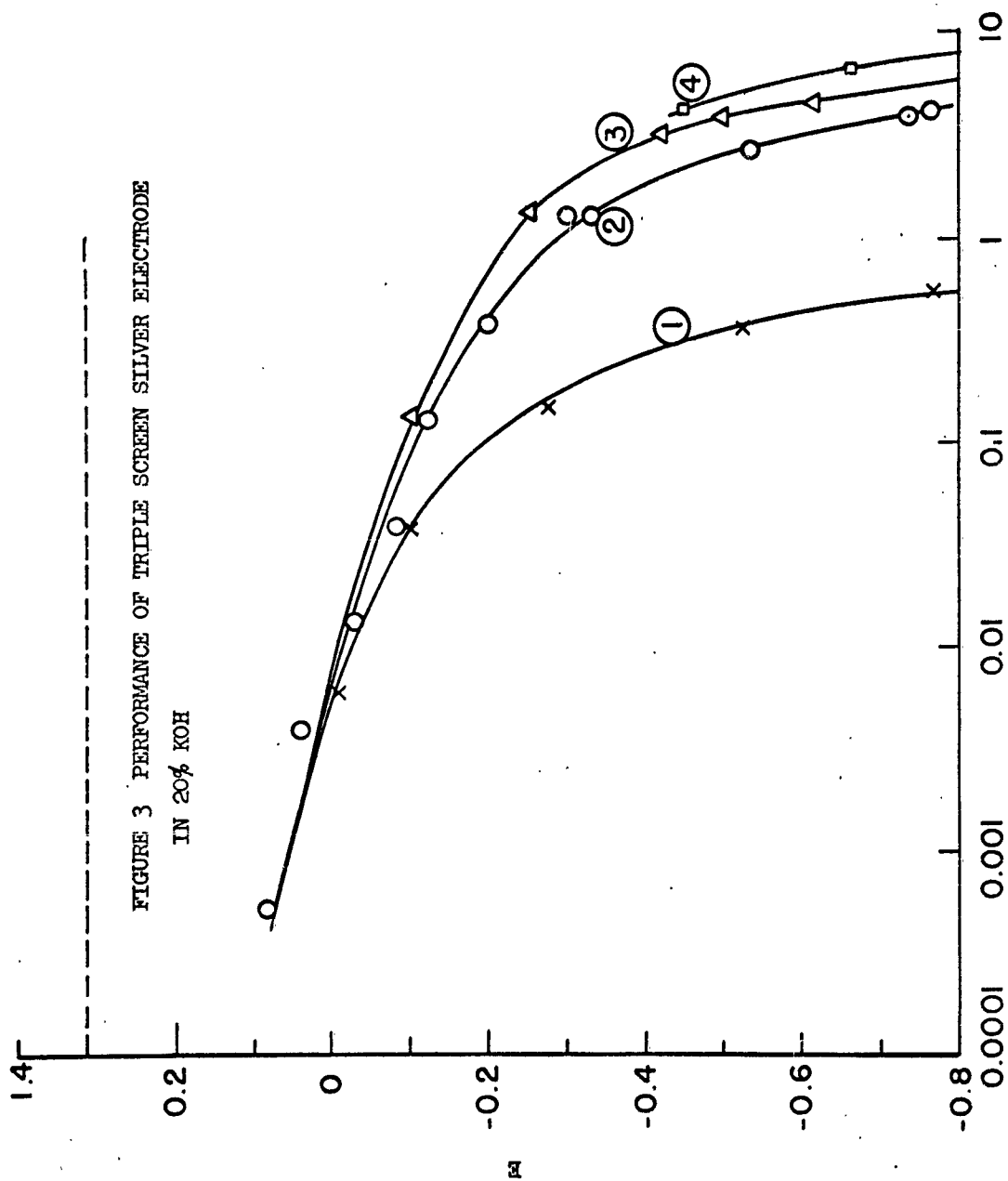PLATINUM ELECTRODE IN 20% KOH

FIGURE 3 PERFORMANCE OF TRIPLE SCREEN SILVER ELECTRODE
IN 20% KOH

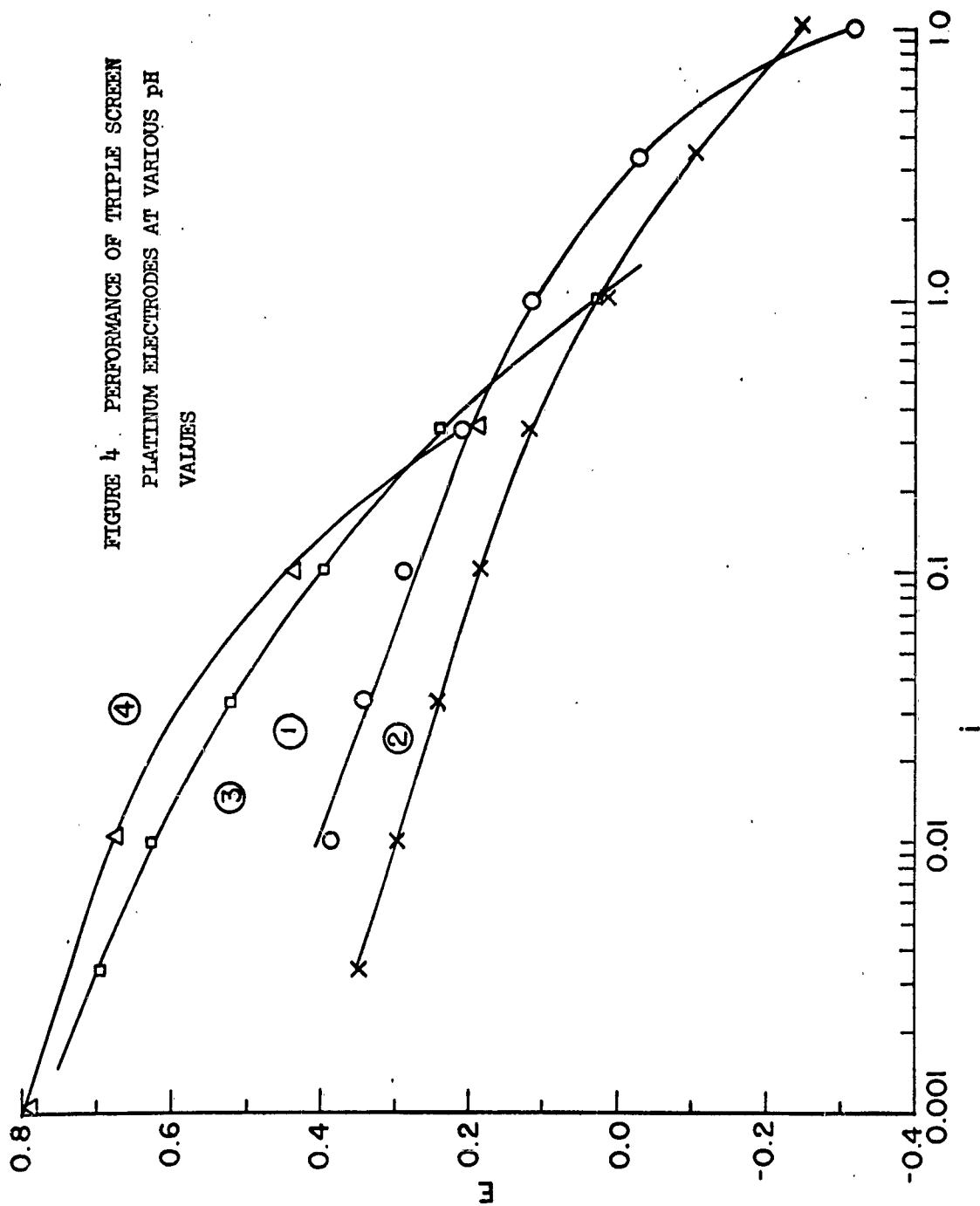FIGURE 4. PERFORMANCE OF TRIPLE SCREEN PLATINUM ELECTRODES AT VARIOUS pH VALUES

FIGURE 5 OVERVOLTAGES AT TRIPLE SCREEN
PLATINUM ELECTRODES VERSUS pH
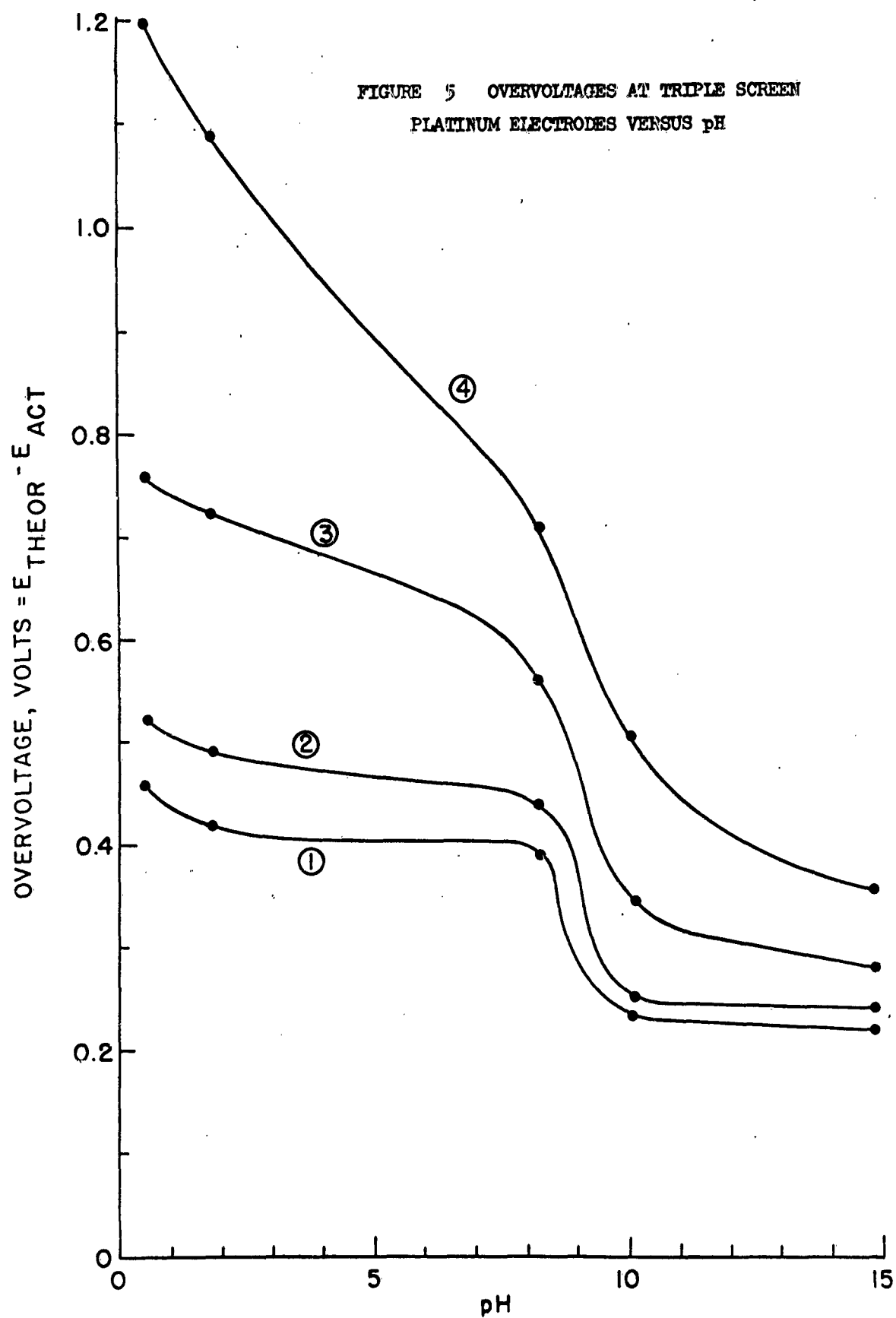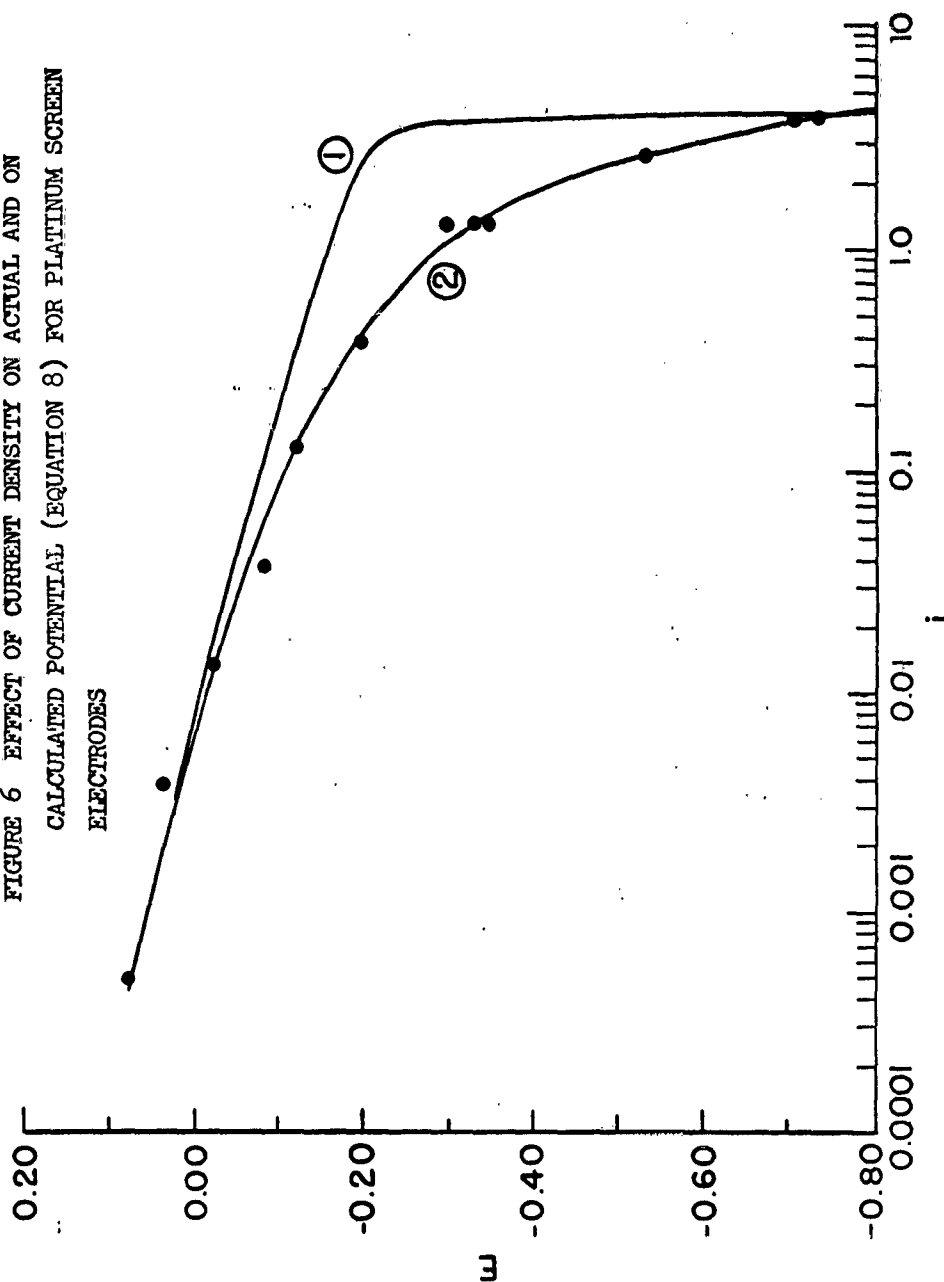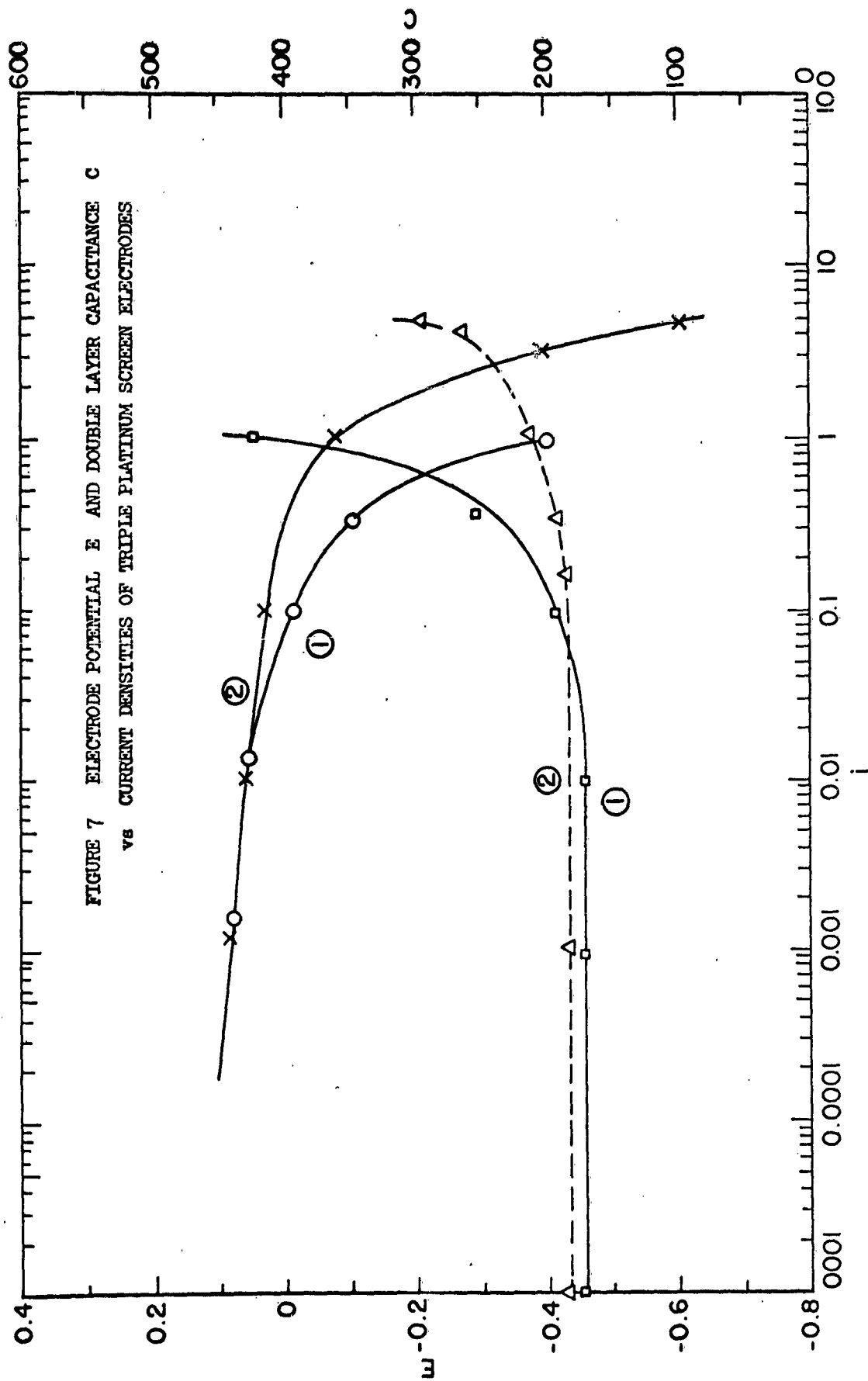
FIGURE 6 EFFECT OF CURRENT DENSITY ON ACTUAL AND ON CALCULATED POTENTIAL (EQUATION 8) FOR PLATINUM SCREEN ELECTRODES

FIGURE 7   ELECTRODE POTENTIAL E AND DOUBLE LAYER CAPACITANCE c
vs CURRENT DENSITIES OF TRIPLE PLATINUM SCREEN ELECTRODES

III HIGH TEMPERATURE METALLURGY RESEARCH ON
THERMOELECTRIC AND THERMIONIC MATERIALS

Personnel:

Nicholas J. Grant, Professor, Metallurgy
Arthur W. Mullendore, Assistant Professor, Metallurgy
Dr. Bill C. Giessen, DSR Research Staff,
Robert Mroczkowski, Research Assistant
Thomas Gibbs, Research Assistant
Joseph Blucher, Research Assistant
Donald Ritter, Research Assistant

INTRODUCTION

Work in this period has continued along the lines set in the ,emiannual Technical Summary Report No. 2, of March 30, 1962. The main emphasis was laid on the programs described in Sections 2.0 and 3.0 of this report, while the phase diagram work in Section 1.0 was continued with a view toward termination of this effort.

1.0 Phase Diagram Investigations

1.1 Thermoelectric Materials

The preliminary phase diagram of the gadolinium-selenium system presented in Fig. 1 of the previous report formed the basis of the work in this period.

The main experimental difficulty consists in obtaining homogeneous alloys with the methods chosen (vapor phase reaction, subsequent arc melting). Therefore, annealing runs at high temperatures were necessary to reach equilibrium. These runs at temperatures up to $1900^\circ C$ are to be carried out in an induction heating unit that was installed in this period. Carbon susceptors serve to heat the alloys which are suspended from thin molybdenum wires. Provisions are made for quenching into a cooled copper block. Termination of work on this system is anticipated for this period.

1.2 Thermionic Materials

The phase diagrams containing rare earths metals or yttrium plus refractory transition metals that were investigated in the past period have been brought to a partial completion. The diagrams Y-Rh and Y-B, which had been given tentatively in the last report, were further worked out and are being readied for publication.

In order to evaluate these alloys, a work function testing diode will
be constructed, modifying the design presently used by the Thermionic Energy
Conversion Laboratory (Tech. Rep. No. 2, p. 96), also to be used on dispersion
thermionic materials.

2.0 Deformation and Fracture of Thermoelectric Materials

After the reduction of scope of the over-all program, it was decided
to limit the deformation and fracture program to one series of alloys which
had been shown to hold interest as a thermoelectric material, namely, the Si-
Ge system. However, the installations constructed will be available for any
extension of the scope of the materials. The necessary steps for this project
were:

   1) Materials Preparation

      a) Melting in quartz tube under purified argon atmosphere in
         induction furnace

      b) Homogenization by isothermal solidification

   2) Measurement of Strength and Conductivity Under Load (Bend Test)

This period was devoted to setting up installations capable of producing
germanium-silicon alloys in research quantities. The purities of the alloys
are to be maintained close to those for the intrinsic semiconductor grade
starting elements used.

The alloys are premelted in sealed quartz capsules under purified
argon in an induction furnace using a carbon susceptor. This equipment, including
sealing off unit and purification train, has been set up.

Since the diffusion rates in diamond structure type alloys are very low
up to melting temperatures, diffusion in the solid state as a means of homogenization
is ruled out. Instead, the alloys will be homogenized by isothermal solidification.
In this technique, which is similar to zone levelling, the boat is charged with two
different compositions corresponding to a solid in equilibrium with a liquid at
constant temperature. The ingot to be homogenized is traversed by a liquid
zone of the liquidus concentration. Since diffusion occurs in the liquid, a solid
homogenized ingot of the solidus concentration freezes out.

The zone melting equipment necessary for this process has been set up and tested. Prior to this, attempts were made to arc-melt alloys in cooled copper crucibles before homogenization, but segregation is severe and the method was not found to be advantageous. In the near future, homogeneous ingots, starting with 0-20 percent Si, balance Ge, will be produced, and examined microscopically and by X-rays to ascertain homogeneity. At the same time, the testing equipment will be set up for bend and resistivity measurements. It is hoped that at a later stage single crystals can be grown and investigated; another interesting approach concerns fabrication methods, e.g., fabrication by extrusions.

3.0 Preparation and Evaluation of Mo-ThO$_2$ Thermionic Emitter Materials

Work in this field, carried out in close cooperation with the Thermionic Energy Conversion Laboratory, M.E. Department, progressed along the following lines:

1. Fabrication of refractory metals and oxide dispersion materials for the measurement of saturation current and work function.

2. Development of equipment to produce high density alloys by gas pressure bonding.

3. Evaluation of Mo-ThO$_2$ alloys, microscopic and electron microscopic observation of structural features, particle size and agglomeration, as well as studies of diffusion and activation mechanisms.

Item 1) Ten different emitter materials were prepared by the technique extensively described in the previous report (mixing, compacting, presintering at 1300°C, sintering at ~1900°C). The alloys prepared had the following concentrations: pure Mo; Mo + 2.5%, 5%, 10%, 15% 25%, 50%, and 75% ThO$_2$; mo + 2.5% and 10% Yb$_2$O$_3$.

The testing of the thermionic properties of some of these alloys is described in detail in the section of this report written by the Thermionic Energy Conversion Laboratory. These compacts show a density of 85 - 90 percent and can be produced with uniform structure and quality. The two alloys in the Mo-Yb$_2$O$_3$ system were included firstly to test the reliability of the fabricating procedure in other systems and secondly because metallic Yb has a significantly

lower work function, than Th (ϕ_{Yb} = 2.59 eV) and a change in the work function of an emitter containing Yb rather than Th might give indications about the role of the low work function element in a dispenser type cathode. An expansion of this approach to cover various related metals and possibly also introducing borides or carbides rather than oxides is planned at a later stage.

Item 2) In order to obtain higher density alloys, a gas pressure bonding apparatus has been constructed. Its basic design is described in the last report and some typical applications are presented in reference (1). Up to the present time, it has been possible to reach a pressure of 10,000 psi at $1600^{\circ}F$ or 5000 psi at $2000^{\circ}F$ with this equipment. $Cu-ThO_2$ slugs have been compacted to 98 percent density at 5000 psi, and $1800^{\circ}F$, for 2 hours. $Ni-ThO_2$ was compacted in quartz capsules to 99 percent density at 5000 psi and $2000^{\circ}F$ for 5 hours. Using 10,000 psi at $1600^{\circ}F$, the density of $Mo-ThO_2$ compacts could not be raised above 85 percent. Therefore, higher temperatures to cause increased flow in the Mo are necessary. Although the gas pressure bonding apparatus is designed for use at 10,000 psi and $2000^{\circ}F$, it was not immediately possible to reach these conditions, because the increased heat conductivity and density of the inert gas used to transmit the pressure caused a breakdown of the power leads. The capacity of the furnace has now been increased to 10,000 psi at $2000^{\circ}F$ by building an improved furnace. This furnace is now operational and has been tested.

Some of the $Mo-ThO_2$ alloys have been duplicated for production in this furnace; they will be available for comparison in the near future.

Item 3) $Mo-ThO_2$ alloys have been studied with optical and electron microscopy after use as emitter electrodes. Platinum shadowed carbon replicas of the electron bombarded and of the emitting surfaces of Mo, $Mo-10\% ThO_2$ and $Mo-25\% ThO_2$ emitter discs (compare Fig. 6, page 96, of the previous report for details) were investigated.

Two typical structures of $Mo-10\% ThO_2$ samples at a magnification of 5000X are presented in Figs. 1 and 2. This emitter had operated at up to about $2200^{\circ}K$. Figure 1 shows the structure of the emission side and Fig. 2 that of the opposite side which had been bombarded by an electron beam for heating.

In Fig. 1, large particles of thoria are visible on the grain boundaries of the Mo matrix, and small particles of thoria, probably precipitated, from solid solution, can be seen inside the Mo grains. This would suggest increased solubility of thoria in Mo at high temperatures. It is noteworthy that the total amount of precipitated and grain boundary thoria is less than the initial content of 10 percent; this can be attributed to depletion by evaporation. Grain growth of the Mo is observed, as would be expected, as well as agglomeration of the thoria particles visible on the grain boundaries.

Figure 2 shows essentially the same precipitate in the matrix as in Fig. 1, but no large thoria particles on grain boundaries. Instead, the grain boundaries are marked by a different level of the Mo matrix. The reason for this preferential attack is not yet known. Wavy lines attributed to thermal etching are easily recognized throughout the structure.

These preliminary results promise an interesting study of the structural changes of the surface in correlation with the observed electronic properties after various heat treatments, which will be initiated. They also suggest that a closer examination of the Mo-ThO$_2$ system with a special view at the high temperature solubilities in Mo may be desirable.

References

1. E.S. Hodge, C.B. Boyer, F.D. Orcutt: Gas Pressure Bonding, I. and E.C., V. 54, No. 1.

Figure 1. Mo + 10% ThO$_2$ emitter surface, 5000X. Emission side.

Figure 2. Mo + 10% ThO$_2$ emitter surface, 5000X. Electron beam side.

IV SOLID STATE ENERGY CONVERTERS

Personnel:

    Professor D.C. White, Ford Professor of Engineering
    Professor J. Blair, Assistant Professor, Electrical Engineering
    Professor B.D. Wedlock, Assistant Professor, Electrical Engineering
    G.S. Almasi, Research Assistant, Electrical Engineering
    P.J. Shaver, Research Assistant, Electrical Engineering
    A. Martinelli, Fellowship Student, Electrical Engineering
    F. Leith, Fellowship Student, Electrical Engineering
    B.A. Smith, Secretary, Electrical Engineering (part time)

Research Report:

1.0 Graded Energy Gap Semiconductor Device

The three most commonly used semiconductor photosensitive devices are the photoconductive cell, the P-N junction converter, and the photo-electro-magnetic (PEM) cell. These devices all depend on the incident photons to create hole-electron pairs. An important disadvantage of such homogeneous-bandgap photocells is the fact that they operate with maximum efficiency at only one input frequency; for if the energy of the incident photons is smaller than the bandgap, no pairs are created, whereas if the energy of the photons is larger than the gap, the excess energy goes into heating the lattice. On the other hand, if it were possible to make a device in which a continuous range of bandgaps exists and in which each photon is absorbed at the point where its energy is equal to the bandgap, it should be possible to convert a continuous spectrum of radiation with maximum efficiency. Another interesting feature of such a device would be the presence of built-in fields due to inhomogeneity. Thus it is possible that the excess-carrier currents in such a device would flow primarily by drift. This may lead to outputs larger than those available from a normal P-N junction cell or a normal PEM cell, in which the excess-carrier currents flow mainly by diffusion.

It has been suggested that the HgTe-CdTe solid solution system might be especially suitable for such a device. This system has the interesting property, that the energy gap is a function of composition, varying from 1.5 eV in pure CdTe to a band overlap in pure HgTe. It is now fairly well established that the transition region between two similar interdiffused semiconductors may be treated as a region of continuously varying energy gap, effective mass, mobility, and excess carrier lifetime. Thus it should be possible to make a device with a varying band-gap by interdiffusing HgTe and CdTe. This program is concerned with the analysis of such a device operating with a magnetic field (i.e., in the PEM mode) and with experimental work which has been done towards the fabrication of such a device by diffusing Hg into CdTe.

The theoretical procedure used was as follows: The Boltzmann transport equation is used first to derive the equations of motion in such a non-homogeneous semiconductor in the presence of a magnetic field. The main feature of these equations is the presence of built-in quasi-electric fields due to the inhomogeneity of the material. Two cases were considered, that of a region which is intrinsic throughout and that of a region which is uniformly doped throughout. It was found that both these cases can be treated under the assumption of quasi-neutrality. The behavior of this region in the presence of optically injected excess carriers was considered.

It was shown that the operation of the device is dominated by the drift of the optically generated excess carriers in the quasi electric field, and diffusion contributions were neglected. The efficiency of a graded energy gap device was shown to be about 50 times that of a homogeneous gap PEM converter.

The experimental part of the program concentrated on the realization of a thin graded energy gap region by diffusing mercury telluride into cadmium telluride. Such regions were obtained successfully in a diffusion process which was designed to control the atmosphere of the environment during diffusion. The composition of the graded region was evaluated using electron microprobe analysis.

Further work is planned on studying the diffusion process, and on the evaluation of device performance under various conditions of diffusion and excitation. The results of the investigation are expected to give additional insight into the physical processes inside a heterogeneous semiconductor transition region.

2.0   Radiation Damage of Semiconductors and Semiconductor Devices

Silicon controlled rectifiers were subjected to a maximum integrated fast neutron flux of 4×10^{13} nvt/cm^2 in the M.I.T. Nuclear Reactor. This maximum integrated flux was obtained by a number of short irradiations, measurements being made on the electrical properties of the controlled rectifier after each irradiation.

An increase in the emitter current required to obtain a given value of alpha was observed after irradiation. This increase is attributed to an increase in the bulk recombination in the base region. The variation of alpha with emitter current in the controlled rectifier is attributed to recombination in the space charge layer.

Using a slightly modified form of the expression for alpha given by Sah et al, computations were made for alpha as a function of emitter current and irradiation time and compared with the measured values. It is felt that the agreement is close enough to indicate that the shape of the alpha versus emitter current curve is still dependent on recombination in the space charge layer under irradiation, and that the maximum value of alpha decreases under irradiation due to bulk recombination of the base region.

At an integrated fast neutron flux of approximately 10^{13} nvt/cm^2, the saturation voltage increased, reaching values greater that 200 volts at an integrated fast neutron flux of 4×10^{13} nvt/cm^2. This sudden increase in the saturation voltage is attributed to the maximum alpha becoming less than unity and therefore, the saturation voltage being determined by the multiplication factor at the center junction. Under irradiation the breakover voltage increased due to the requirement that, since alpha decreases with irradiation, the multiplication factor must increase to satisfy the breakover condition, thereby increasing the breakover voltage. The increase in the saturation voltage, the increase in the breakover voltage and the decrease in the effectiveness of the trigger due to the decrease of alpha, were investigated.

The results of this investigation show that the silicon controlled rectifier in its present form is not suitable for use in a neuclear environment where it will be subjected to an integrated fast neutron flux exceeding 10^{13} nvt/cm^2.

3.0   Transport Properties of Zinc-Antimonide

An important application of zinc antimonide is its use as the p-type leg against an n-type lead telluride leg in thermoelectric power generators. There is very little modern effort under way to explore the properties of this material in a systematic way. A program of fundamental investigation of the thermal and transport properties of this material is initiated.

There has been no published attempt to develop a model for any of the transport properties of this material. The nature and mechanism of the high temperature instability and the effects of annealing both single crystal zinc antimonide and zinc antimonide alloy systems has not been established. Inasmuch as this instability appears when the material is raised to temperatures around 100°C, it is a phenomena which has an important influence on the optimization of ZnSb for higher temperature thermoelectric applications.

The following areas need to be investigated in order to gain a fundamental understanding of the properties of ZnSb. This work on ZnSb would also supply information of a basic nature about the little invesigated system of group II-V semiconductors.

1) Physical Properties

(a) Crystal Growth

The production of single crystal zinc antimonide has been reported by several researchers. Both pulling and zone recrystallization techniques have been used. These techniques will have to be duplicated and possibly improved upon in our laboratory.

(b) Thermal Instabilities

The mechanism of the reported irreversible instabilities in the electronic transport parameters in the neightborhood of 100°C is of great interest. Whether this instability is due to a phase change and/or a chemical decomposition of the material is not clear.

Previous workers have resorted to annealing their polycrystalline samples in order to gain high temperature thermoelectric stability. It would be interesting to see what effect this annealing process has on the physical structure and transport properties of single crystals.

(c) Doping

Methods for the Systematic control of carrier concentrations in ZnSb have to be developed. In particular, a method for producing n-type single crystals is needed.

2) Transport Properties

Zine antimonide forms orthorhombic crystals. Hence, its transport properties will be considerably more anisotropic than those of more familiar semiconductors such as lead telluride, which is cubic. For instance, the diagonalized electrical conductivity matrix for an orthorhombic crystal contains three independent parameters while the electrical conductivity matrix for a cubic crystal contains just one independent parameter which is called a scalar electrical conductivity. Other transport parameters, such as the Hall coefficient, thermoelectric power, and magnetoresistance coefficients will be anisotropic.

There have been no detailed experimental investigations into any of the above or other electronic transport effects in zinc antimonide. Cyclotron resonance experiments have yielded only sketchy information about the effective masses of charge carriers.

Thus, it is seen that careful investigations of phenomena like thermal and electrical conductivity, thermoelectric power, Hall effect, magnetoresistance, cyclotron resonance, optical reflection phenomena will contribute new and useful information about the basic transport properties of this material.

3) Development of a Model for the Transport Properties of Zinc Antimonide

The characterization of the transport properties of zinc antimonide and an evaluation of its potential as a thermoelectric element awaits the basic information that is supplied by carefully performed experiments.

4.0   The Thermo-Photo-Voltaic Effect and Its Utilization in Energy
        Conversion

        Theoretical expressions for the collection efficiency and optimum
junction depth have been developed and solved on a digital computer. The
results show that the optimum junction depth always lies between an absorp-
tion length and a diffusion length, irrespective of the surface recombination
velocity. Increasing surface recombination velocity, however, shifts the
optimum junction depth toward an absorption length. These monochromatic
results have been extended to cover the more general chromatic case. It
has also been shown that relative collection efficiency vs. wavelength data
can be used to experimentally determine diffusion length, junction depth,
surface recombination velocity, and absorption coefficient.

        A series of p-n, p-i, and p-i-n germanium diode converters
have been fabricated according to the theoretical principles developed above.
Excellent agreement was obtained and accurate measurements of the semi-
conductor properties mentioned above achieved. Also it was found that
spectral response measurements can be used to experimentally determine
diffused impurity penetrations.

        The best converter configuration was found to be the p-i-n diode.
The efficiency of one of these devices was investigated under varying inten-
sity and wavelength. The converter obeyed the low-level injection theory at
all intensities measured. It was found that efficiency increased with inten-
sity up to the limit of the radiation source. The maximum value obtained was
4.23 percent at 282 mw/sq cm. Band-limited light improved efficiency at a
given intensity. Based on these experimental results conversion efficiencies
of 30% at intensities on the order of 10 watts/sq cm are expected.

Publications

H.A. Lyden, The Effective Masses of Free Carriers in PbTe: Their Temperature Dependence and Contribution to Transport Properties. .

J.M. Borrego-Larralde, Optimum Impurity Concentration in Semi-conductor Thermoelements, AFCRL-62-148, Contract No. AF19(604)-4153, January 15, 1962.

B.D. Wedlock, Spectral Response and Conversion Efficiency of P-N Junctions, Scientific Report No. 3, Contract No. 1841(78), August 20, 1962.

Research on Materials, Processes, and Devices Related to Energy Conversion, M.I.T. School of Engineering, Technical Summary Report No. 2, Nonr 1841(78).

F.A. Leith, Effects of Fast Neutrons on Silicon Controlled Rectifiers, paper delivered at the Electron Devices Meeting, PGED of IRE, Washington D.C., October 1962.

G.S. Almasi, A. Mercury Telluride Cadmium Telluride Graded Gap Device, M.S. Thesis, Department of Electrical Engineering, August 1962.

B.D. Wedlock, Thermo-Photo-Voltaic Conversion from High Temperature Energy Sources, delivered at 1962 Electron Devices Meeting, Washington, D.C., October 1962.

V. THE DEVELOPMENT OF THERMIONIC EMITTER MATERIALS

Personnel:

E.N. Carabateas, Assistant Professor, Mechanical Engineering
Arthur Shavit, Instructor, Mechanical Engineering
R. Vanderweil, Jr., Research Assistant, Mechanical Engineering
C. Deininger, Laboratory Assistant, Mechanical Engineering

Research Report

(Starts on next page)

1.0 Introduction

      The present report describes the experimental re-
sults obtained in a research program aimed at the development
of thermionic emitter materials with a specified value of work
function at a given operating temperature. This program is
sponsored by the Office of Naval Research with funds provided
by ARPA, under the M.I.T. Contract No. DSR 8848. In this en-
deavor the thermionic energy conversion group is in close co-
operation with the Department of Metallurgy, where the work
on the various materials was performed. The primary objective
for the development of these materials is motivated from the
fact that considerable improvement in the efficiency of cesium
thermionic converters is deemed possible if the cesium is only
used to provide the necessary ions for the neutralization of
the electron space charge and not to lower the emitter work
function by covering the emitter surface. The latter function
of the cesium requires a higher pressure than the former and
therefore the present optimization of the cesium pressure in
converters is a compromize between these two functions of the
cesium.

      The ideal performance of cesium converters is achieved
when there are no transport effects in the interelectrode re-
gion, that is, the electron mean free path is considerably
larger than the interelectrode spacing so that losses due to
collisions are not important. Under these conditions for a
given operating temperature the efficiency has a steep maxi-
mum at a particular value of the emitter work function[1]. This
optimum value of work function is shown as a function of the
operating temperature in Figure 1. A typical value ob-

tained from the above Figure is 2.8 volts at a temperature of
1850°K. In order for a pure material such as a refractory
metal to attain this value of work function at the above tem-
perature by cesium coverage the cesium pressure must be raised
to a value which makes the collisionless ideal performance
impossible. This causes transport losses which may account
for as much as 50% of the output power, and therefore the ef-
ficiency. On the otherhand, the work function of refractory
metals can be changed by the addition of another component
such as a rare earth. Therefore, binary mixtures of refrac-
tories with different percentages of rare earths have been
tested in an effort to obtain the desired values of work
function. In this report the experimental set-up used for the
measurement of the work function of different emitter mater-
ials is described. Subsequently measurements from a pure
molybdenum emitter used to test and calibrate the test set-up
are presented. The experimental results obtained from a
M_o + 10% ThO_2 mixture for two different preparation methods
and for a M_o + 25% ThO_2 mixture are given. The effect of dif-
ferent activation processes is described. Finally a discussion
of the experimental results and the direction of the future
effort is outlined.

FIGURE 1

Optimum Work Function for Maximum Efficiency Versus Temperature
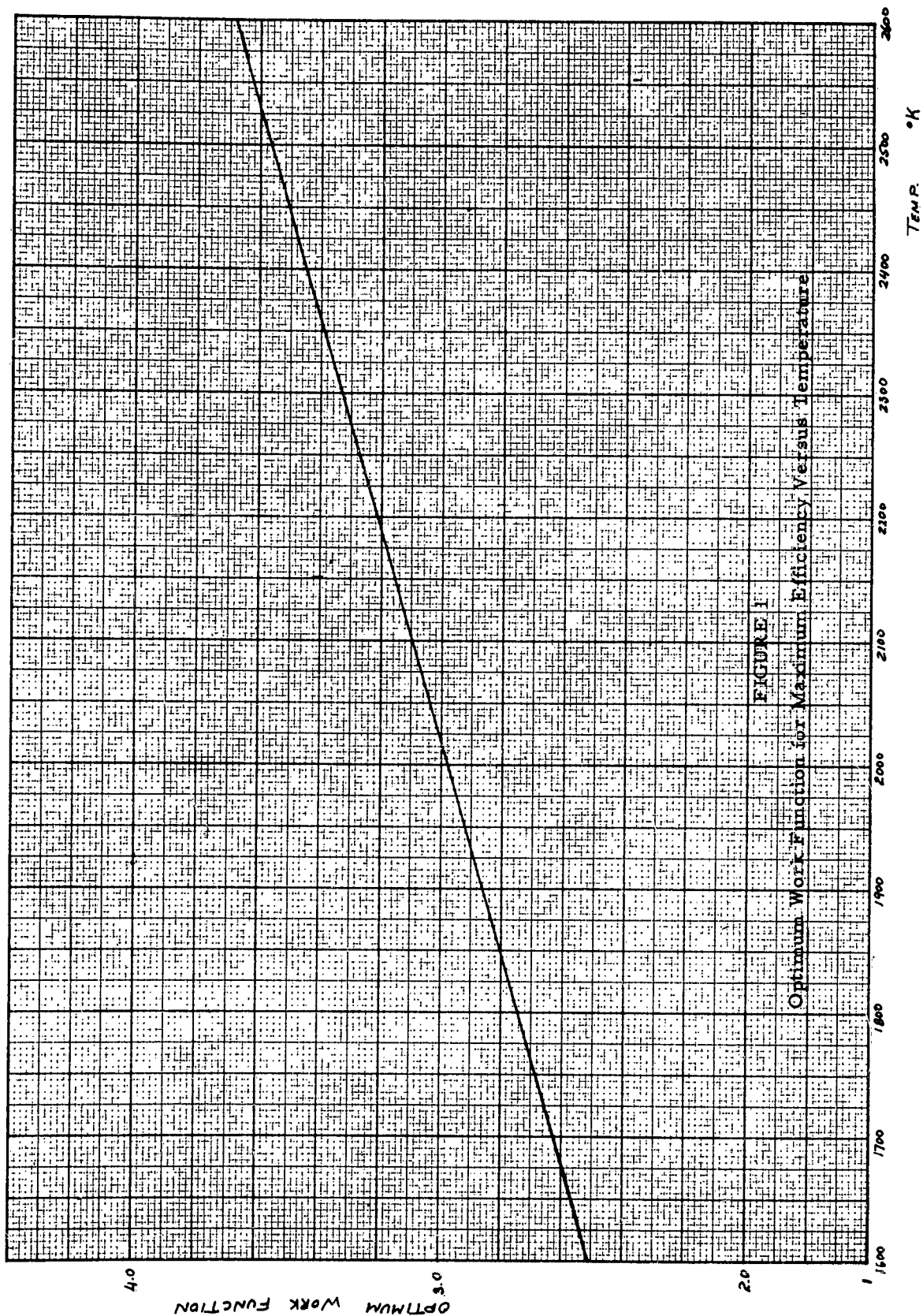
2.0 Experimental Set-up

Two vacuum tubes were constructed and calibrated by testing pure molybdenum emitters.*

The first tube was found to be inadequate for the tests because of improper shielding which resulted in substantial leakage current from the bombardment filament. The leakage currents were of higher order of magnitude than the' thermionic currents and therefore the measurements were not reliable.

A second tube was built in which the leakage problems were eliminated. All the following results are from measurements on the second tube. The tube is shown schematically in Figure 2. The emitter is dropped into a fitted emitter holder and can be easily interchanged(by lifting and replacing it with another emitter). The collector is shielded by a nickel tube whose potential can be independently controlled. The bombardment filament is covered by a shield that also serves to focus the electron beam. The tube is placed in a vacuum system where the pressure is maintained at $2 \times 10^{\pm 6}$ mm Hg to 4×10^{-6} mm Hg.

The emitter is heated by electron bombardment method. A filament is heated by controlled AC current and the thermionicly emitted electrons of the filament are accelerated by a high voltage of the order of 1000V - 1500V, towards the emitter. In this way the emitter may be brought to any desired temperature.

---

* The tubes were designed to facilitate easy testing of various emitter materials.

The voltage between emitter and collector is changed and controlled either by a D.C. voltage source or by a variac and an isolation transformer. The thermionic current is measured by the potential drop in precision resistors. The current voltage characteristics are plotted on X-Y recorder (only possible when slow varying potential is applied) or displayed on an oscilloscope and photographed. The electric circuit is shown schematically in Figure 3.

Some typical I-V curves as photographed from the scope are shown in Figure 4.
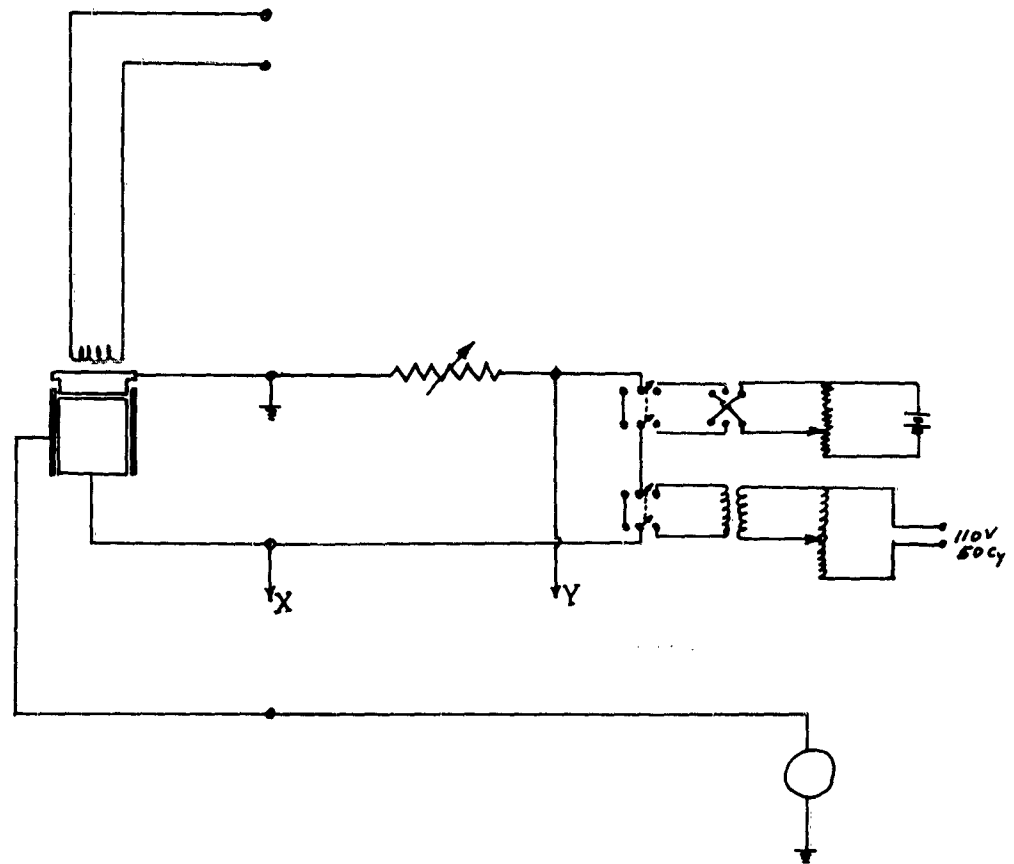
FIGURE 2

Schematic of Experimental Set-up.
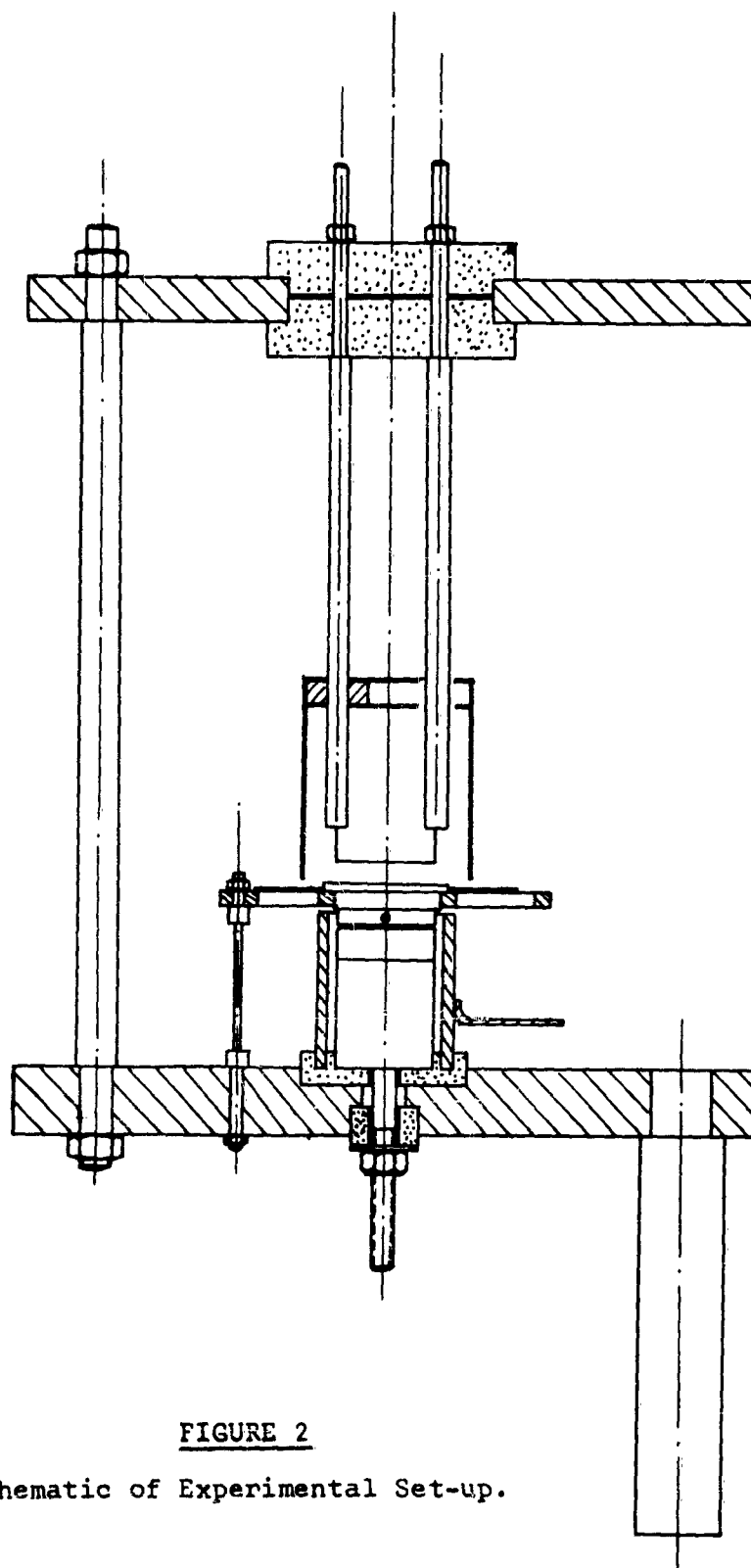
FIGURE 2

Schematic of Experimental Set-up.
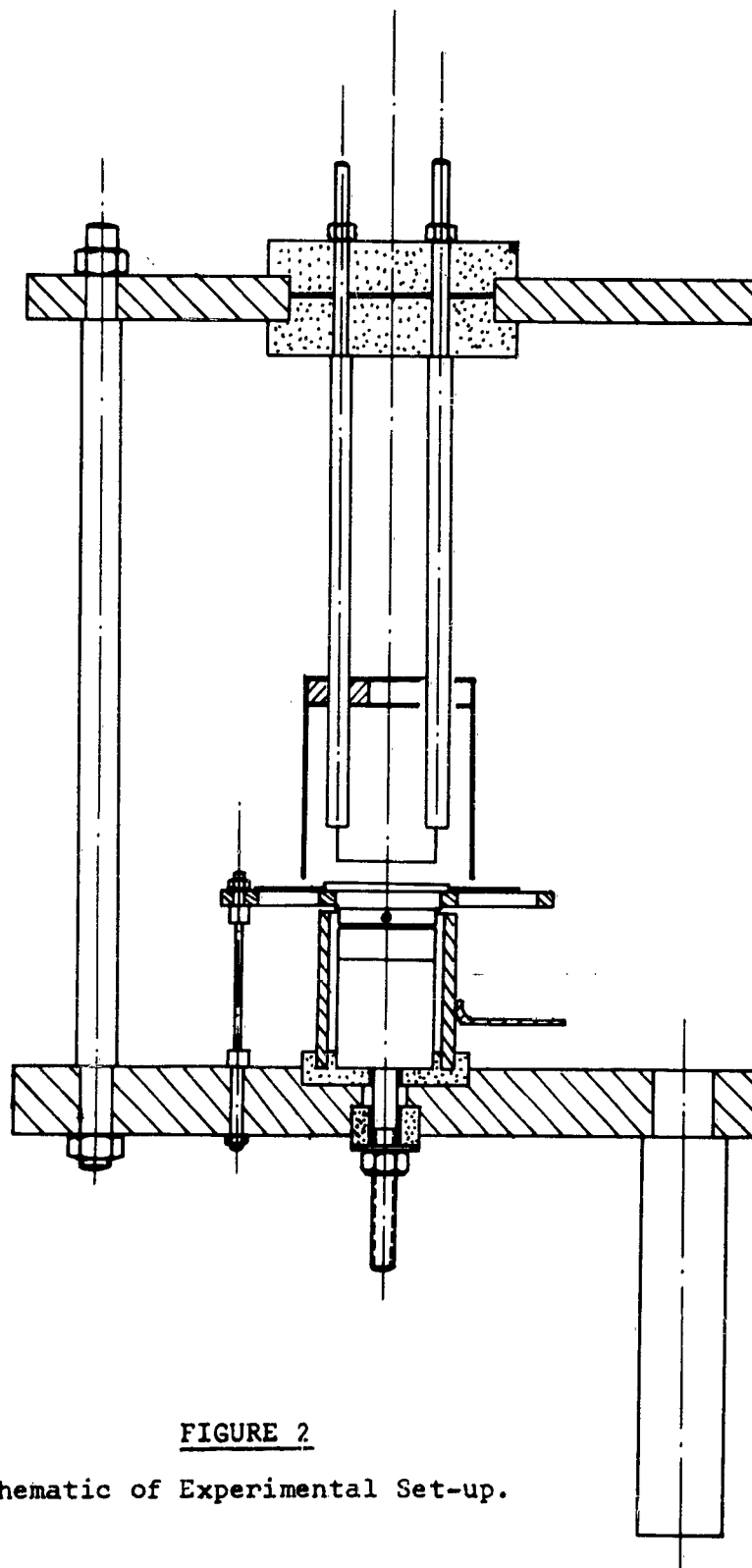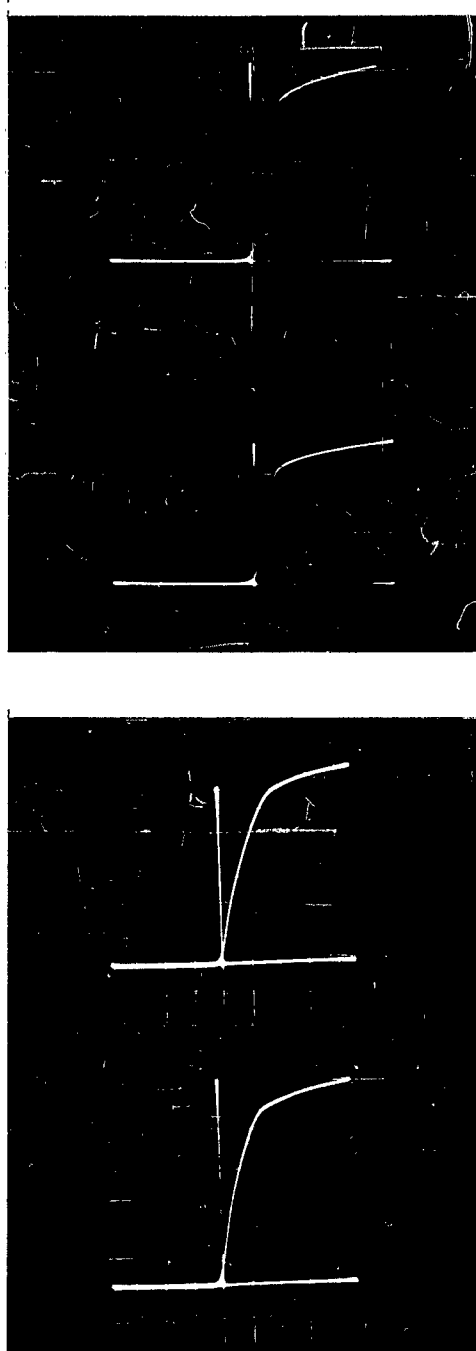
FIGURE 3

Schematic Diagram of Electrical Circuit

FIGURE 4

Photographs of Typical Experimental Current-Voltage
Curves Obtained on the Oscilloscope

3.0 Experimental Results - Pure Molybdenum

A series of tests with pure molybdenum emitter were performed in order to calibrate and check the instrumentation. Some characteristic current voltage plots corresponding to different emitter temperatures are shown in Figure 5. The results are plotted on a log I versus V scale. The full line corresponds to the characteristics of an ideal converter, with no space charge effects. The voltage current curves shown in Figure 5, for emitter temperatures ranging from 1560 to 1910 show that quite good accuracy could be obtained from the experimental set-up used in these tests, All the curves show a well defined saturation current which is obtained at low enough values of the voltage so that corrections due to the Schotky effect can be neglected. Furthermore, in the space charge region the slope of the line determined by the experimental points corresponds very closely to the observed temperature measured independently with a thermocouple. The work function was determined by two methods. One method is by Richardson's equation

$$J_s = AT^2 \, e^{-\emptyset/kT} \tag{1}$$

where $A = 120 \, \frac{Amp}{cm^2 \cdot R}$ for all surfaces. The results are shown in Figure 14. The second method consists of plotting $\log(\frac{J_s}{AT^2})$ versus $1/kT$ as shown in Figure 6. From Equation (1) we have

$$\log(\frac{J_s}{AT^2}) = - \frac{\emptyset}{kT} \log e \tag{2}$$

and if the work function depends on temperature linearly that is if

$$\emptyset = \emptyset_0 + \quad kT \qquad\qquad (3)$$

we have therefore

$$\log(\frac{J_s}{AT^2}) = [- \frac{\emptyset_0}{kT} - \alpha] \log e \qquad\qquad (4)$$

In Equation (4) $\emptyset_0$ is the work function at zero temperature as determined from the slope of $\log(\frac{J_s}{AT^2})$ versus $1/kT$. The coefficient α gives the temperature dependence. From the experimental results it was found that the work function of moly is best given as a function of temperature with the values of the constants $\emptyset_0$ and α equal to $\emptyset_0 = 4.36$, $\alpha = -.71$. Hence

$$\emptyset = 4.36 - 0.062f(\frac{T}{1000}) \qquad\qquad (5)$$

In some references the temperature dependence is shown in terms of a variable coefficient A_r in Richardson's equation. The relation between A_r, A and α is
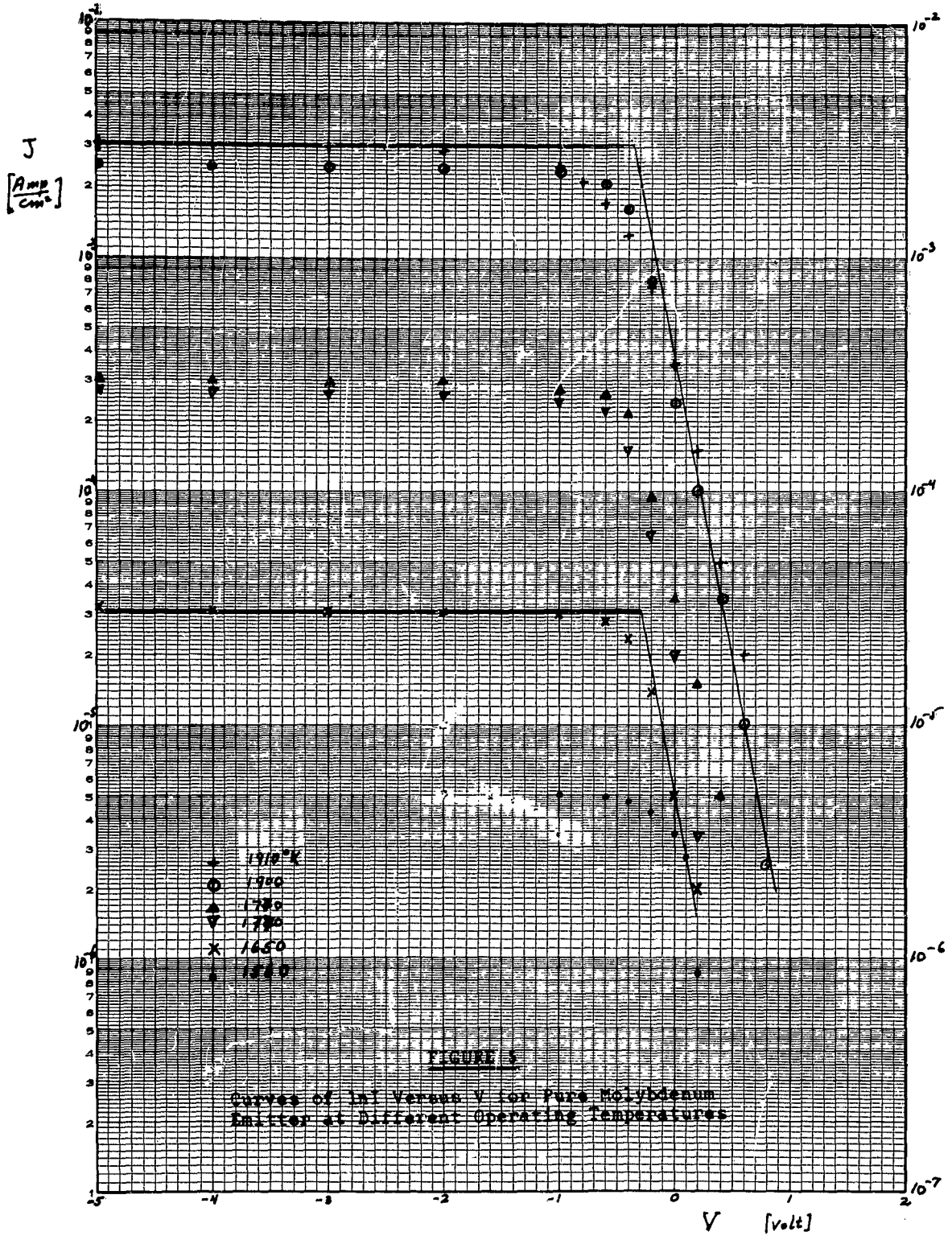
$$\frac{A_r}{A_a} = e^\alpha \qquad\qquad (6)$$

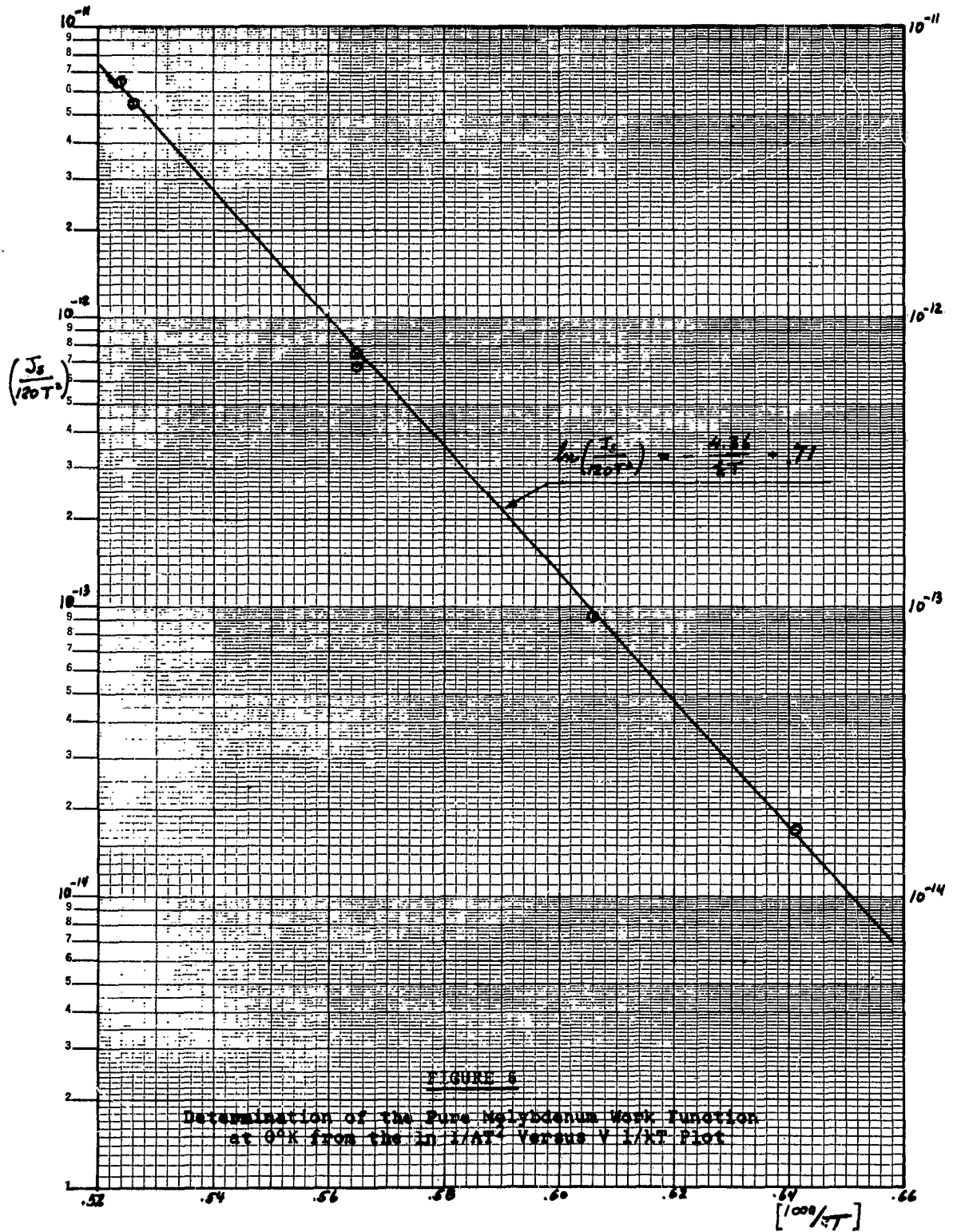Therefore in this case $A_r = 120 \ e^{-0.71} = 58 \ amp/cm^2 {}^\circ K^2$. A comparison between the present results and reported values is shown in Table I.

TABLE I

Source	$\emptyset_0$	A_r	Method
Roy[2]	4.31	60	Thermionic Emission
	4.33		Photoelectric Treshhold
Dushman[3]	4.45	60	Thermionic Emission
	4.50	60	Thermionic Emission

FIGURE 5

Curves of ln J Versus V for Pure Molybdenum
Emitter at Different Operating Temperatures

FIGURE 5

Determination of the Pure Molybdenum Work Function
at 0°K from the ln J/AT² Versus V 1/kT Plot

4.0 Experimental Results for 10% ThO$_2$

Two samples of moly + 10% ThO$_2$ were tested. Both samples were prepared by the Metallurgy Department in M.I.T. by the sintering method. The two samples however were different as to the pressure and temperature of sintering and therefore were different in density. The densities were approximately 85% and 95% respectively.

The data was taken in a similar way as for the pure molybdenum emitter. In Figure 7a experimental results for the approximately 85% dense thoriated molybdenum sample are shown for three different temperatures of 1520°K, 1620°K and 1760°K. In Figure 7b experimental results for the approximately 95% dense sample are shown for a range of operating temperatures. Comparison of these results shows that the preparation method makes a difference in the value of work function the more dense sample corresponding to a lower value of work function or a higher value of the saturation current. It should be pointed out that the saturation current is reached at a higher voltage than in the case of pure moly. Therefore in order to find the saturation current at zero field it is necessary to use Schottky type plotts. Typical Schottky plots are shown in Figure 8.
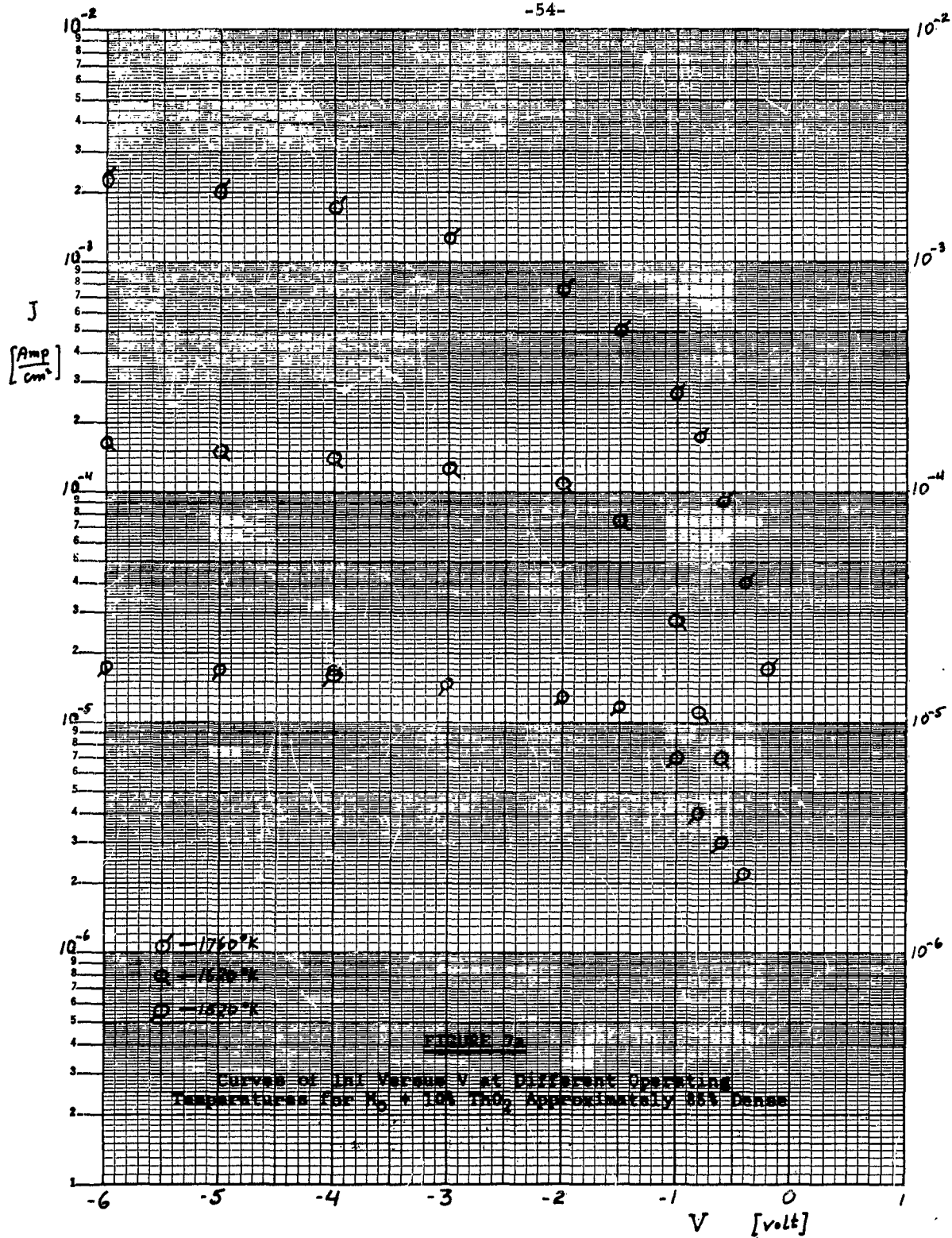
Whereas the work function for theppure moly emitter is a function of temperature only, the work function of the binary mixture of moly and ThO$_2$ depends on both the operating temperature and the history of heat treatment.
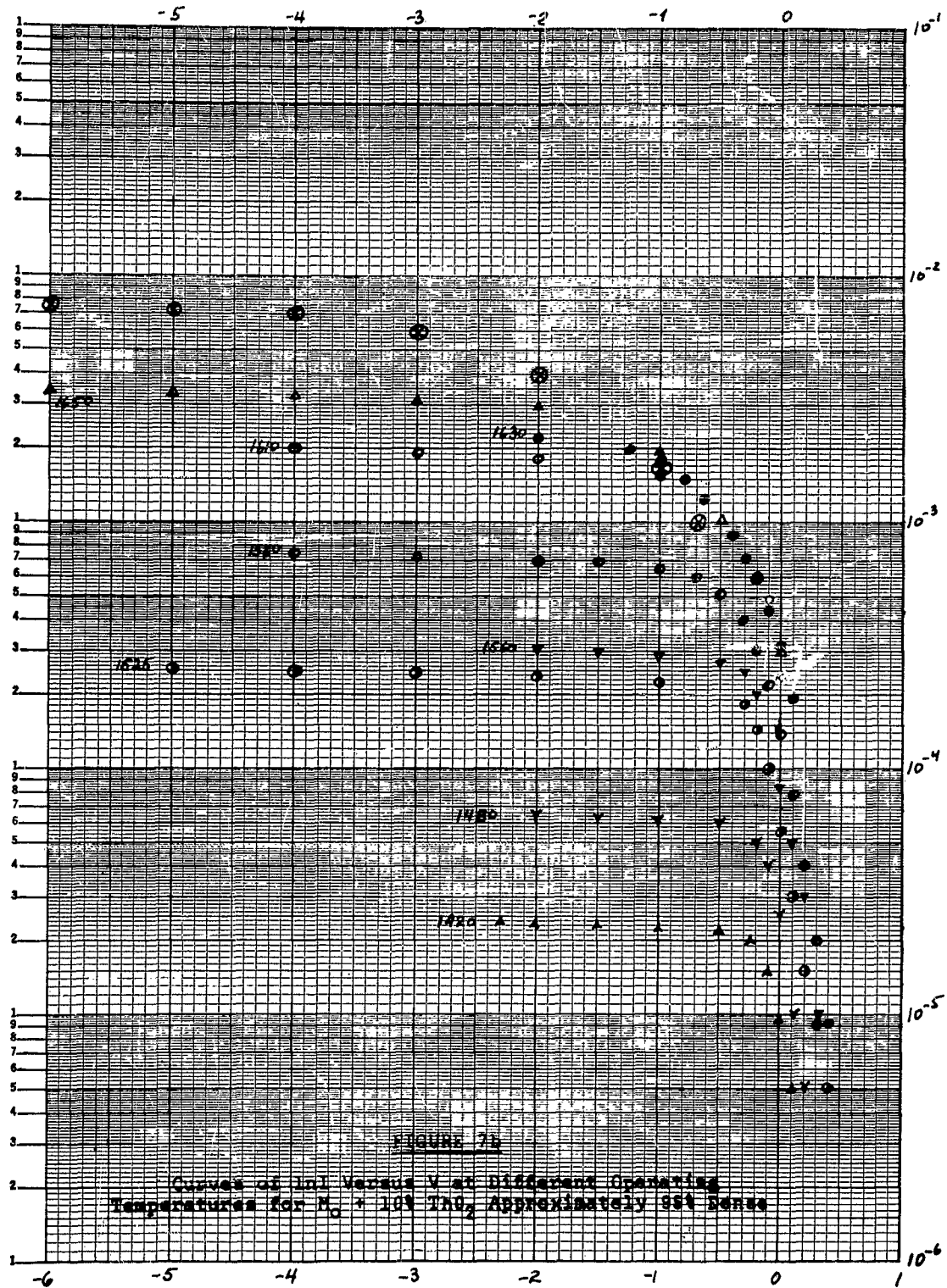
It was found that the work function of clean emitter surface immediately after machining and with no exposition to
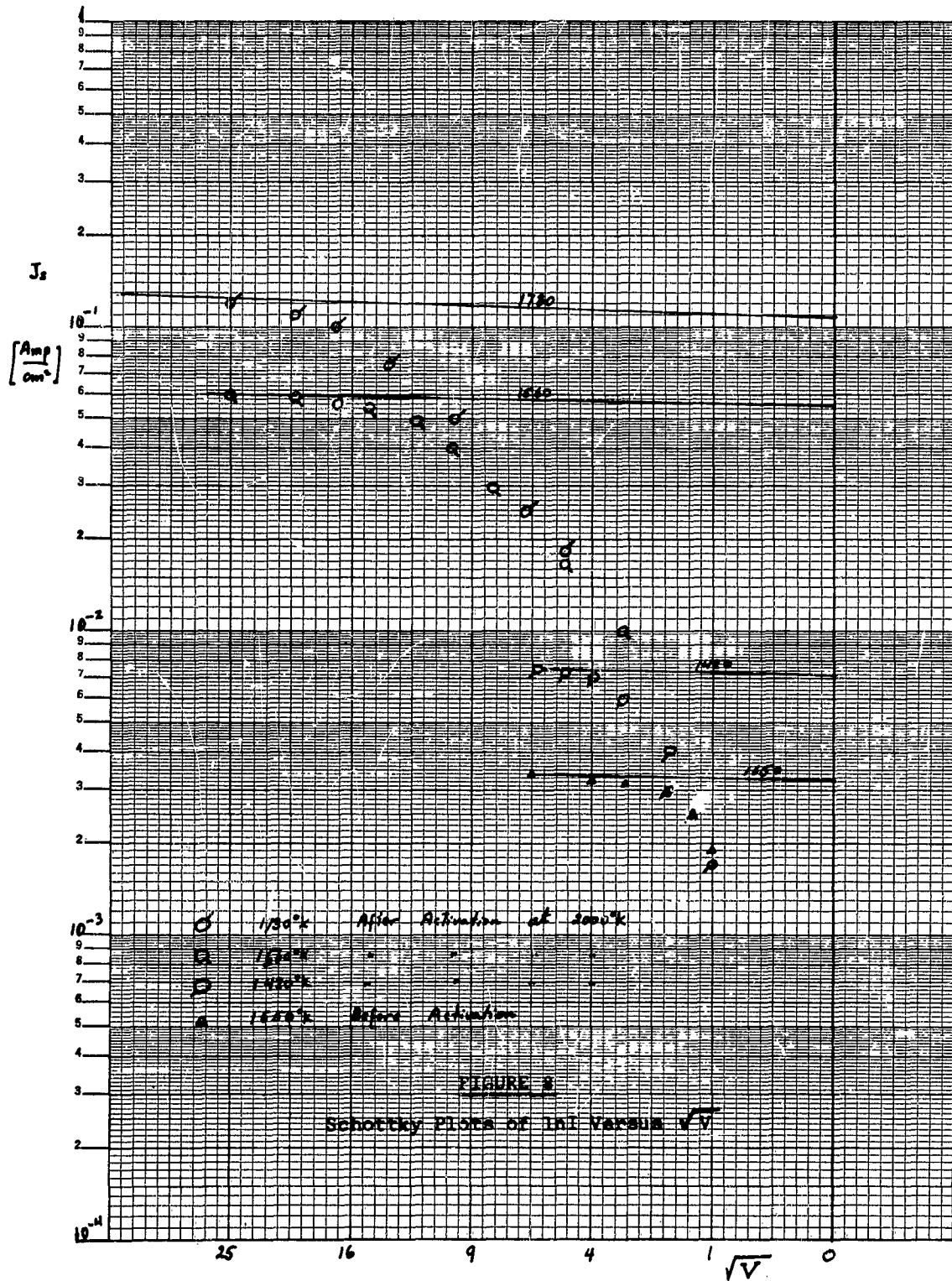
high temperature has a higher value. This value is repro-
duced even after long cooling period as long as the surface
was not exposed to a high temperature (activation temperature).
The values of work function obtained from the voltage-current
curves plotted in a Schottky plot for the M_O + 10% ThO_2 mix-
ture are summarized in Figure 9 where the work function is
plotted versus operating temperature for different values of
the activation temperature. In Figure 10, the plot of $\ln\frac{T}{AT^2}$
versus $\frac{1}{kT}$ is shown. When the surface is heated to a high
temperature (2000°K) for a short time and cooled down again
the work function decreases. After the surface was activated,
its work function assumes a lower value even after a long
cooling period and the original value can not be reached.
Furthermore, the work function also depends on the activation
temperature shortly before the measurement was taken.

Series of data was taken with the emitter at a fixed
temperature of 1410°K. The work function was measured but
before every measurement the emitter was activated to a progres-
sively higher temperature (ranging from 1410°K to 2100°K).
The activation was made by quick heating of the emitter to the
prescribed value maintaining it to within $\pm$ 20°K for five min-
utes and then cooling quickly to 1410°K and taking the current
voltage characteristic. It was found that the work function
decreases with increasing activation temperature up to a value
of 2100°K. Above this value no significant change in the work
function was observed. The experimental results are summar-
ized in Figure 11, where the value of work function is plotted
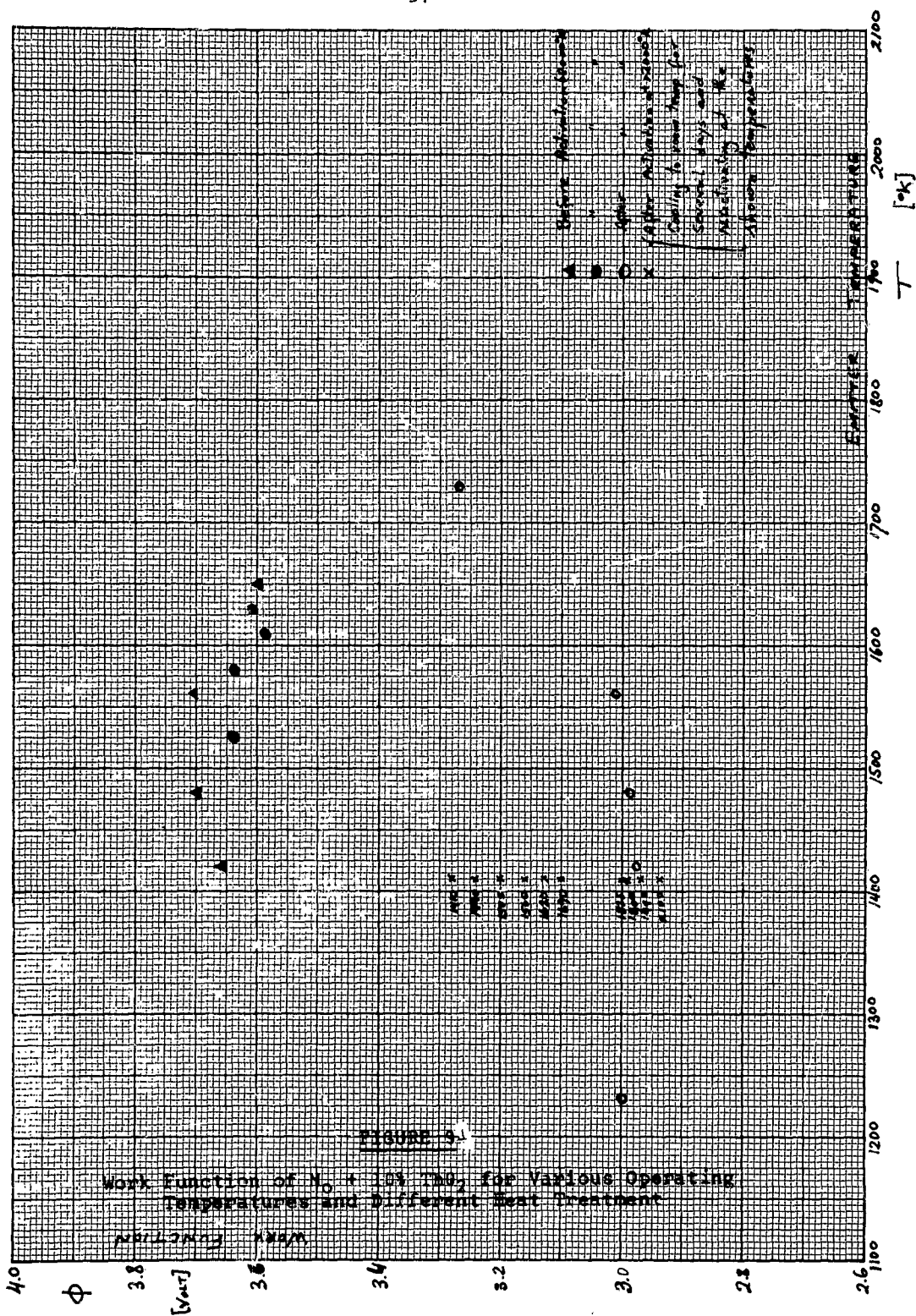versus the activation temperature for fixed operating emitter

temperature of 1410°K. It should be pointed out that these results are for measurements taken shortly after the activation treatment was performed. If, However, the emitter is maintained at a constant value of 1410°K for a long time its work function will slowly increase and reach asympotically a higher value. The "relaxation" time is about five to seven hours.
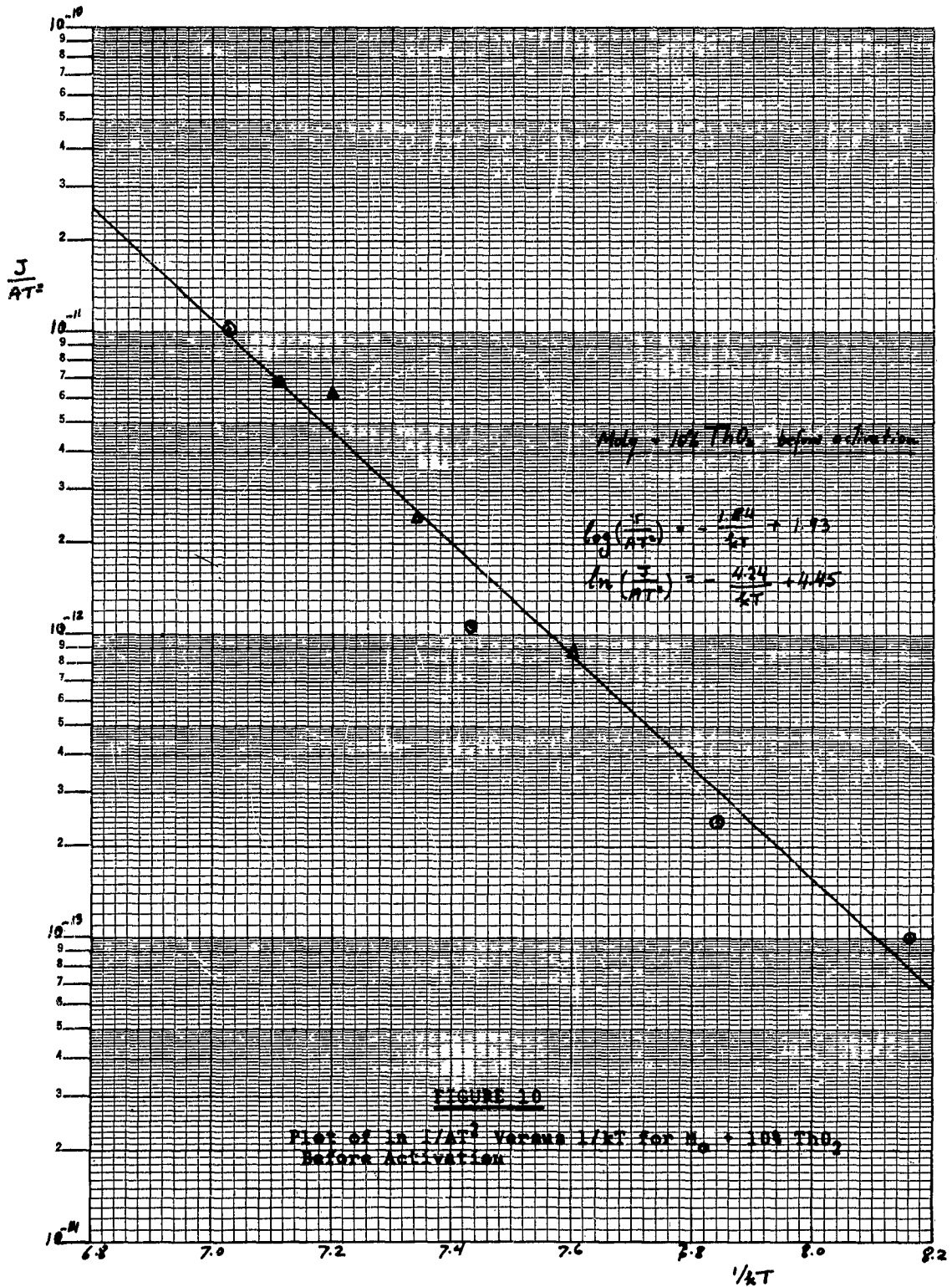
FIGURE 5a

Curves of J vs V at Different Operating
Temperatures for M_0 + 10% ThO_2 Approximately 85% Dense

FIGURE 7b

Curves of lnI Versus V at Different Operating
Temperatures for $M_o + 10\% ThO_2$ Approximately 98% Dense

FIGURE 8

Schottky Plots of lnI Versus $\sqrt{V}$

FIGURE 9

Work Function of No + 10% ThO2 for Various Operating
Temperatures and Different Heat Treatment

FIGURE 10

Plot of ln J/AT² versus 1/kT for Mo + 10% ThO₂
Before Activation

FIGURE 11

Work function of $Mg + 10\%$ ThO_2 at an Operating Temperature of $1{,}100°K$ for Various Activation Temperatures
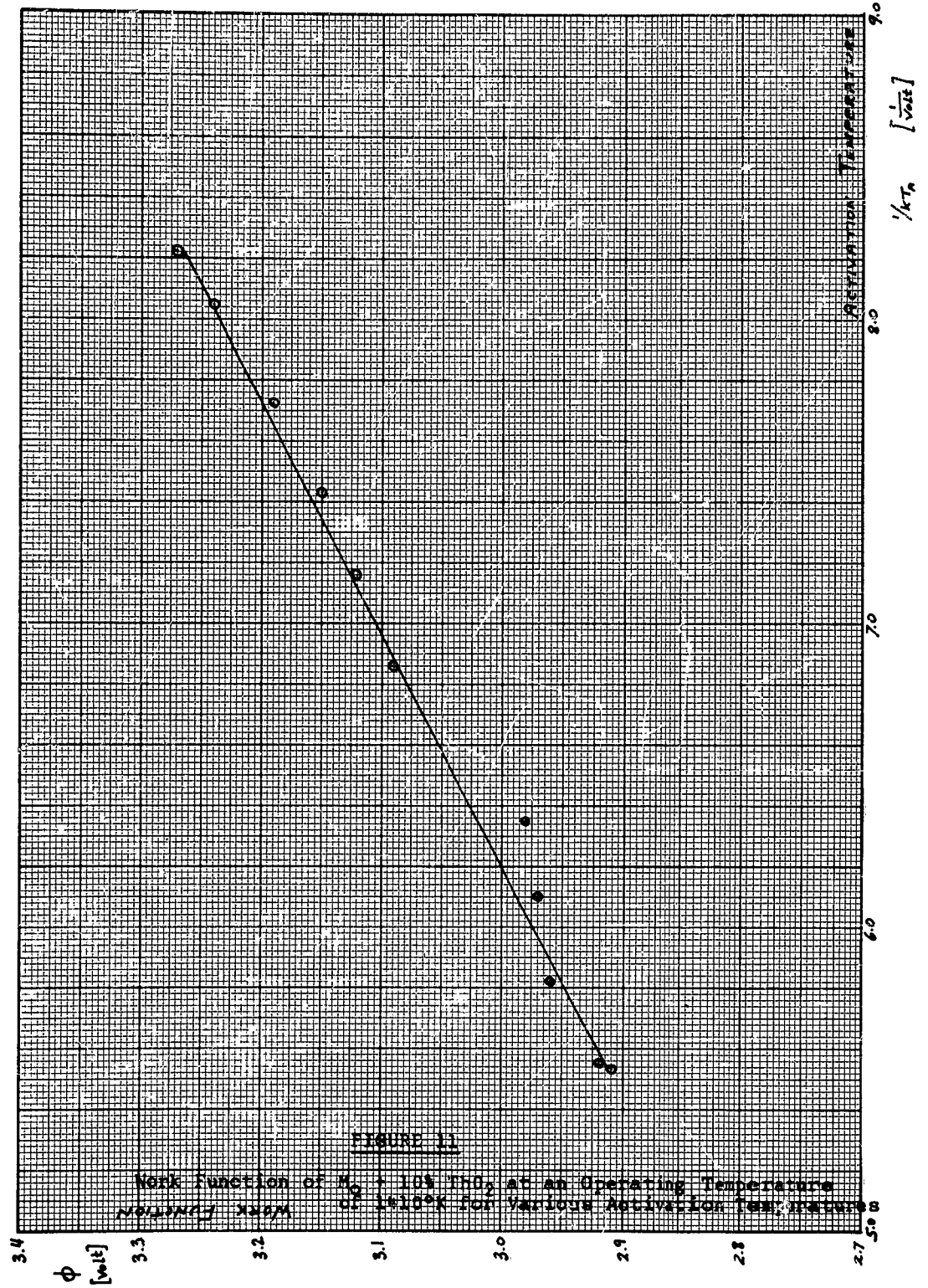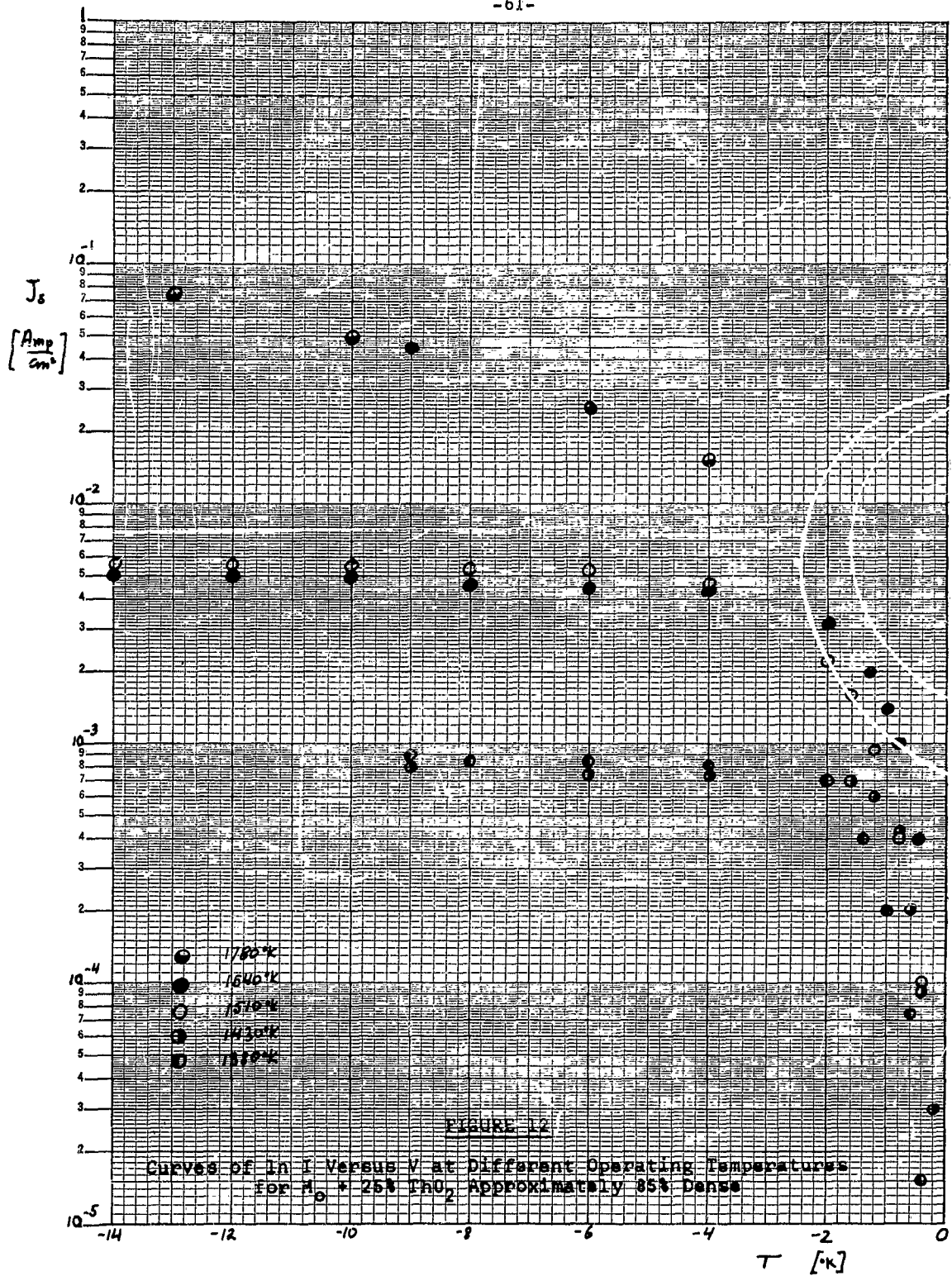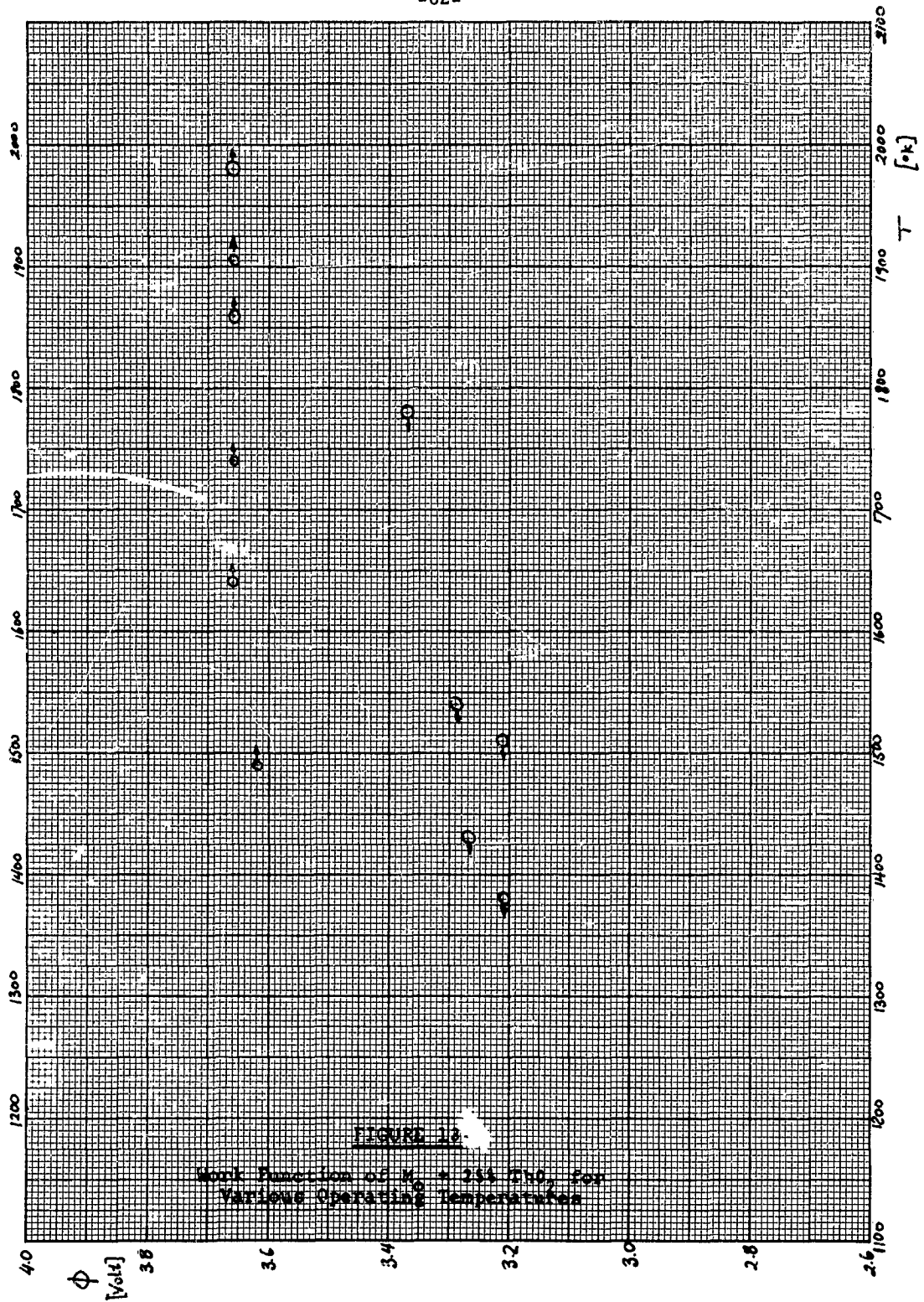
5.0 Experimental Results - 25% ThO$_2$

Only one sample of 25% ThO$_2$ was tested. This sample was of the lower density variety (85% density). In general it was found that the work function of the thoriated moly does not depend strongly on the thoria concentration between 10% and 25%. Typical log I versus $\sqrt{V}$ characteristics are shown in Figure.12. The work function for this sample as computed from Schottky type plotts are given in Figure 13. The experimental data falls into two distinct regions of work function values. The higher value is before activation and the lower value is after activation at 2000°K.

FIGURE 12

Curves of ln I Versus V at Different Operating Temperatures
for M$_o$ + 25% ThO$_2$ Approximately 85% Dense

FIGURE 19

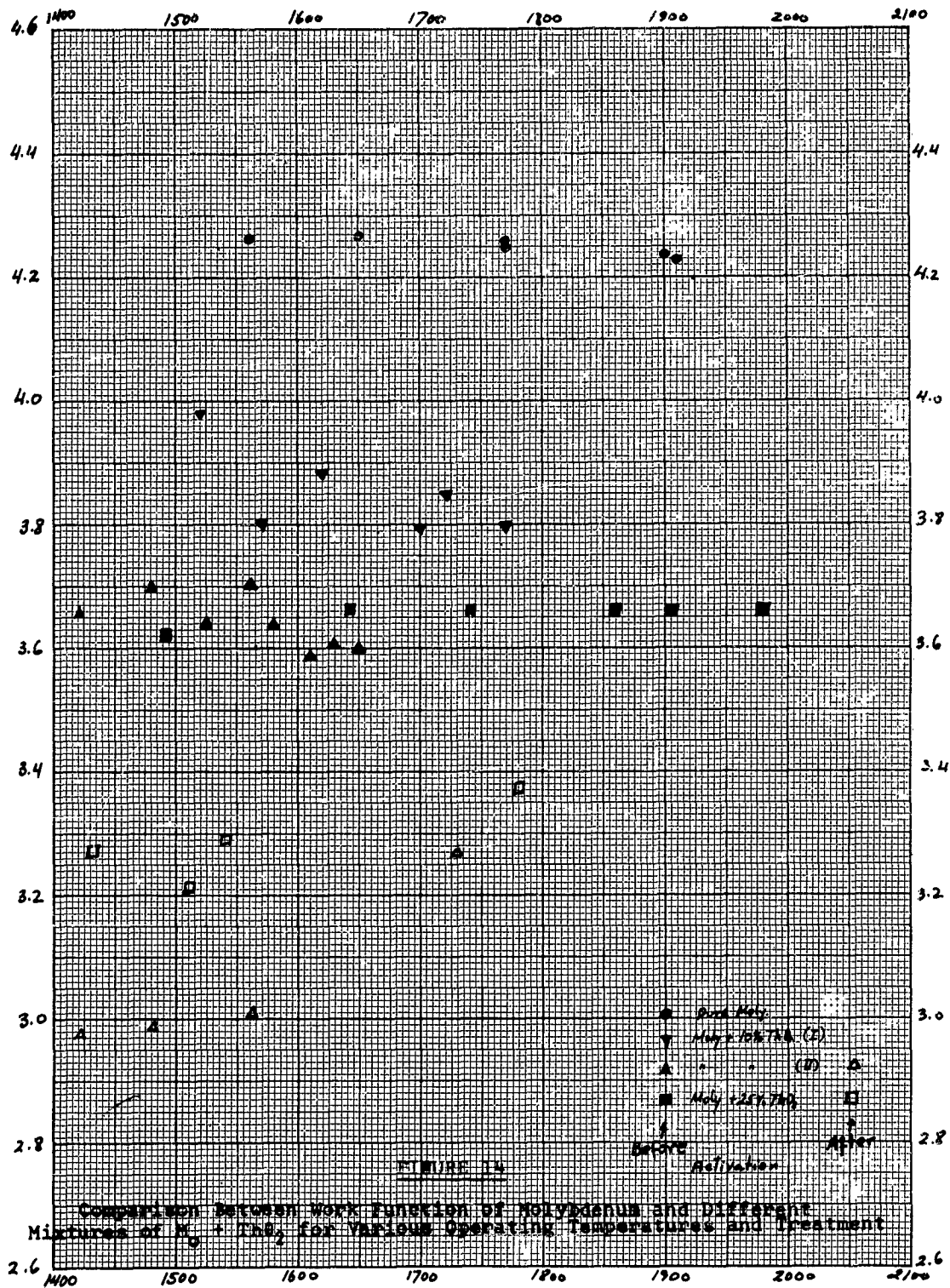Work Function of Mo + 25% ThO₂ for
Various Operating Temperatures

6.0 Discussion of the Results

The experimental results described in this report show that the work function of thoriated moly surfaces is not a function of temperature only but depends strongly on the activation temperature. The minimum value of the work function obtained in these tests was about 2.95 volts. However, this value can not be maintained at lower temperature unless frequent activations are made. A summary of the experimental results obtained from the different samples that were tested in a variety of conditions is shown in Figure 14. In the remaining part of this program the samples which were tested in vacuum will be tested in a cesium atmosphere. In this way the effect of cesium on materials with different initial values of work function can be studied.i In addition samples of moly centered with ytterbium are presently under testing in order to evaluate the effect of other types of rare earths on the work function of the mixture. Photographs of the surface such as shown in Figures 1 and 2 of the reportonnHighhTTempera- ture Metallurgy research will supplement the electron emission studies in order to obtain a clear picture of the parameters affecting the value of work function.

FIGURE 14

Comparison Between Work Function of Molybdenum and Different
Mixtures of M_0 + ThO_2 for Various Operating Temperatures and Treatment

7.0 References

1. First Semi-annual Technical Summary Report, Contract No. Nonr 1841(78), September 30, 1961.

2. Roy, Proceedings Royal Soc. 112, 599, (1926).

3. Dushman, Rev. Modern Phy. 2, 381, (1930).

UNCLASSIFIED

AD
Massachusetts Institute of Technology
Cambridge 39, Massachusetts
RESEARCH ON MATERIALS PROCESSES-- AND
DEVICES RELATED TO ENERGY CONVERSION by the
School of Engineering Interdepartmental Energy Conver-
sion Activity. 31 December 1962. 68pp., additional re-
prints (Contract No. Nonr 1841(78) Office of Naval
Research Authorization ARPA Order No. 214-62
Task No. NR099-360, Project Code No. 9800,
M.I.T. Project DSR No. 8848-49.) Report No. 6.
                    Unclassified report

Research Reports on:

   I. SUPERCONDUCTING MATERIALS AND SYS-
TEMS
   II. ELECTROCHEMICAL ENERGY CONVERSION
RESEARCH
   III. THERMOELECTRIC AND THERMIONIC
MATERIALS RESEARCH
   IV. SOLID STATE ENERGY CONVERTERS
   V. THE DEVELOPMENT OF THERMIONIC
EMITTER MATERIALS

UNCLASSIFIED

UNCLASSIFIED

AD
Massachusetts Institute of Technology
Cambridge 39, Massachusetts
RESEARCH ON MATERIALS PROCESSES-- AND
DEVICES RELATED TO ENERGY CONVERSION by the
School of Engineering Interdepartmental Energy Conver-
sion Activity. 31 December 1962. 68pp., additional re-
prints (Contract No. Nonr 1841(78) Office of Naval
Research Authorization ARPA Order No. 214-62
Task No. NR099-360, Project Code No. 9800,
M.I.T. Project DSR No. 8848-49.) Report No. 6.
                    Unclassified report

Research Reports on:

   I. SUPERCONDUCTING MATERIALS AND SYS-
TEMS
   II. ELECTROCHEMICAL ENERGY CONVERSION
RESEARCH
   III. THERMOELECTRIC AND THERMIONIC
MATERIALS RESEARCH
   IV. SOLID STATE ENERGY CONVERTERS
   V. THE DEVELOPMENT OF THERMIONIC
EMITTER MATERIALS

UNCLASSIFIED

UNCLASSIFIED

AD
Massachusetts Institute of Technology
Cambridge 39, Massachusetts
RESEARCH ON MATERIALS PROCESSES-- AND
DEVICES RELATED TO ENERGY CONVERSION by the
School of Engineering Interdepartmental Energy Conver-
sion Activity. 31 December 1962. 68pp., additional re-
prints (Contract No. Nonr 1841(78) Office of Naval
Research Authorization ARPA Order No. 214-62
Task No. NR099-360, Project Code No. 9800,
M.I.T. Project DSR No. 8848-49.) Report No. 6.
                    Unclassified report

Research Reports on:

   I. SUPERCONDUCTING MATERIALS AND SYS-
TEMS
   II. ELECTROCHEMICAL ENERGY CONVERSION
RESEARCH
   III. THERMOELECTRIC AND THERMIONIC
MATERIALS RESEARCH
   IV. SOLID STATE ENERGY CONVERTERS
   V. THE DEVELOPMENT OF THERMIONIC
EMITTER MATERIALS

UNCLASSIFIED

UNCLASSIFIED

AD
Massachusetts Institute of Technology
Cambridge 39, Massachusetts
RESEARCH ON MATERIALS PROCESSES-- AND
DEVICES RELATED TO ENERGY CONVERSION by the
School of Engineering Interdepartmental Energy Conver-
sion Activity. 31 December 1962. 68pp., additional re-
prints (Contract No. Nonr 1841(78) Office of Naval
Research Authorization ARPA Order No. 214-62
Task No. NR099-360, Project Code No. 9800,
M.I.T. Project DSR No. 8848-49.) Report No. 6.
                    Unclassified report

Research Reports on:

   I. SUPERCONDUCTING MATERIALS AND SYS-
TEMS
   II. ELECTROCHEMICAL ENERGY CONVERSION
RESEARCH
   III. THERMOELECTRIC AND THERMIONIC
MATERIALS RESEARCH
   IV. SOLID STATE ENERGY CONVERTERS
   V. THE DEVELOPMENT OF THERMIONIC
EMITTER MATERIALS

UNCLASSIFIED

AD

Massachusetts Institute of Technology
Cambridge 39, Massachusetts
RESEARCH ON MATERIALS PROCESSES--AND
DEVICES RELATED TO ENERGY CONVERSION by the
School of Engineering Interdepartmental Energy Conver-
sion Activity. 31 December 1962. 68pp., additional re-
prints (Contract No. Nonr 1841(78) Office of Naval
Research Authorization ARPA Order No. 214-62
Task No. NR099-360, Project Code No. 9800,
M.I.T. Project DSR No. 8848-49.) Report No. 6.
                    Unclassified report

Research Reports on:

    I. SUPERCONDUCTING MATERIALS AND SYS-
TEMS
    II. ELECTROCHEMICAL ENERGY CONVERSION
RESEARCH
    III. THERMOELECTRIC AND THERMIONIC
MATERIALS RESEARCH
    IV. SOLID STATE ENERGY CONVERTERS
    V. THE DEVELOPMENT OF THERMIONIC
EMITTER MATERIALS

AD

Massachusetts Institute of Technology
Cambridge 39, Massachusetts
RESEARCH ON MATERIALS PROCESSES--AND
DEVICES RELATED TO ENERGY CONVERSION by the
School of Engineering Interdepartmental Energy Conver-
sion Activity. 31 December 1962. 68pp., additional re-
prints (Contract No. Nonr 1841(78) Office of Naval
Research Authorization ARPA Order No. 214-62
Task No. NR099-360, Project Code No. 9800,
M.I.T. Project DSR No. 8848-49.) Report No. 6.
                    Unclassified report

Research Reports on:

    I. SUPERCONDUCTING MATERIALS AND SYS-
TEMS
    II. ELECTROCHEMICAL ENERGY CONVERSION
RESEARCH
    III. THERMOELECTRIC AND THERMIONIC
MATERIALS RESEARCH
    IV. SOLID STATE ENERGY CONVERTERS
    V. THE DEVELOPMENT OF THERMIONIC
EMITTER MATERIALS

AD

Massachusetts Institute of Technology
Cambridge 39, Massachusetts
RESEARCH ON MATERIALS PROCESSES--AND
DEVICES RELATED TO ENERGY CONVERSION by the
School of Engineering Interdepartmental Energy Conver-
sion Activity. 31 December 1962. 68pp., additional re-
prints (Contract No. Nonr 1841(78) Office of Naval
Research Authorization ARPA Order No. 214-62
Task No. NR099-360, Project Code No. 9800,
M.I.T. Project DSR No. 8848-49.) Report No. 6.
                    Unclassified report

Research Reports on:

    I. SUPERCONDUCTING MATERIALS AND SYS-
TEMS
    II. ELECTROCHEMICAL ENERGY CONVERSION
RESEARCH
    III. THERMOELECTRIC AND THERMIONIC
MATERIALS RESEARCH
    IV. SOLID STATE ENERGY CONVERTERS
    V. THE DEVELOPMENT OF THERMIONIC
EMITTER MATERIALS